UNIVERSITÉ DU QUÉBEC À MONTRÉAL

THÈSE PRÉSENTÉE À
L'UNIVERSITÉ DU QUÉBEC À CHICOUTIMI
COMME EXIGENCE PARTIELLE
DU DOCTORAT EN RESSOURCES MINÉRALES
OFFERT À
L'UNIVERSITÉ DU QUÉBEC À MONTRÉAL
EN VERTU DU PROTOCOLE D'ENTENTE
AVEC L'UNIVERSITÉ DU QUÉBEC À CHICOUTIMI

PAR

MARTIN BIZZARRO

GÉOCHIMIE DES ÉLÉMENTS MAJEURS ET DES ISOTOPES (Sr, Nd et Hf) DE PÉRIDOTITES MANTELLIQUES, CARBONATITES ET KIMBERLITES DU CANADA ET DU GROENLAND ; IMPLICATIONS POUR LA DYNAMIQUE DU MANTEAU TERRESTRE

MAI 2002

Bibliothèque
Paul-Émile-Boulet

UQAC
Université du Québec
à Chicoutimi

Mise en garde/Advice

Afin de rendre accessible au plus grand nombre le résultat des travaux de recherche menés par ses étudiants gradués et dans l'esprit des règles qui régissent le dépôt et la diffusion des mémoires et thèses produits dans cette Institution, **l'Université du Québec à Chicoutimi (UQAC)** est fière de rendre accessible une version complète et gratuite de cette œuvre.

Motivated by a desire to make the results of its graduate students' research accessible to all, and in accordance with the rules governing the acceptation and diffusion of dissertations and theses in this Institution, the **Université du Québec à Chicoutimi (UQAC)** is proud to make a complete version of this work available at no cost to the reader.

L'auteur conserve néanmoins la propriété du droit d'auteur qui protège ce mémoire ou cette thèse. Ni le mémoire ou la thèse ni des extraits substantiels de ceux-ci ne peuvent être imprimés ou autrement reproduits sans son autorisation.

The author retains ownership of the copyright of this dissertation or thesis. Neither the dissertation or thesis, nor substantial extracts from it, may be printed or otherwise reproduced without the author's permission.

UNIVERSITÉ DU QUÉBEC À MONTRÉAL

THÈSE PRÉSENTÉE À L'UNIVERSITÉ DU QUÉBEC À CHICOUTIMI
COMME EXIGENCE PARTIELLE DU DOCTORAT EN RESSOURCES
MINÉRALES

OFFERT À:

L'UNIVERSITÉ DU QUÉBEC À MONTRÉAL EN VERTU DU PROTOCOLE
D'ENTENTE AVEC L'UNIVERSITÉ DU QUÉBEC À CHICOUTIMI

PAR

MARTIN BIZZARRO

MAJOR ELEMENT AND ISOTOPE GEOCHEMISTRY (Sr, Nd AND Hf) OF MANTLE DERIVED PERIDOTITES, CARBONATITES AND KIMBERLITES FROM CANADA AND GREENLAND; INSIGHTS INTO MANTLE DYNAMICS

MAI 2002

RÉSUMÉ

Nous avons étudié la composition en éléments majeurs d'une suite de péridotites provenant de la marge nord du craton Archéen de l'ouest du Groenland, ainsi que la composition isotopique (Sr, Nd et Hf) de kimberlites et de carbonatites de l'est du Canada et du sud-ouest du Groenland.

Nos résultats indiquent que le manteau lithosphérique sous la région de Sarfartoq de l'Ouest du Groenland a une épaisseur d'environ 225 km et est constitué d'assemblages réfractaires d'harzburgites et de lherzolites (nombre Mg de l'olivine >0.9). Contrairement aux péridotites du craton de Kaapvaal (Afrique du Sud), les péridotites de la région de Sarfartoq ne sont pas enrichies en OPX et montrent donc plus d'affinités avec les péridotites de l'Est du Groenland (Wiedemann Fjord), de l'île de Somerset (arctique canadien) et de Tanzanie. L'étude détaillée de la composition des différentes phases minérales des péridotites suggère que le manteau lithosphérique sous la région de Sarfartoq soit stratifié comme suit: (1) une couche (70-180 km), caractérisée par une stratification interne, composée de harzburgites (avec ou sans grenats) non-déformées, et (2) une couche (180-225 km) composée de lherzolites fertiles (avec CPX) porphyroclastiques. La stratification interne observée dans la couche de harzburgites non-déformées (70-180 km) est reflétée par une augmentation de fertilité (par exemple diminution de l'abondance d'olivine et contenu inférieur en fostérite) avec la profondeur. La nature abrupte de la stratification semble indiquer que la formation de la racine lithosphérique s'est effectuée en au moins deux stades.

La composition isotopique du Sr de cristaux d'apatite et de carbonate provenant de l'intrusion alcaline de Sarfartoq, Groenland, a été mesurée avec l'aide d'un système d'ablation laser couplé à un MC-ICP-MS. Cent sept analyses montrent des rapports $^{87}Sr/^{86}Sr$ variant de ~0.7025 à ~0.7031. Cette variation du rapport $^{87}Sr/^{86}Sr$ (~0.0006) est largement supérieure à la reproductibilité externe de la méthode (~0.000047; 2σ). L'ampleur de l'intervalle des valeurs $^{87}Sr/^{86}Sr$ suggère que l'apatite et le carbonate ont précipité dans des conditions de deséquilibre. Il est possible que les variations isotopiques observées à l'échelle centimétrique reflètent des processus d'ordre régionaux, comme par exemple le mélange de magma carbonaté provenant de différentes sources mantelliques ou, alternativement, un domaine mantellique hétérogène. Cette technique analytique fournit une approche rapide et pertinente pour déterminer l'ampleur de l'hétérogénéité isotopique dans un échantillon ou parmi différents minéraux, avec la précision analytique approchant cela obtenu par méthode TIMS conventionnelles.

L'analyse des isotopes de l'Hf et les âges U-Pb de carbonatites et kimberlites provenant du Canada et Groenland, y compris la plus ancienne carbonatite connue (3 Ga), indique que ces magmas proviennent d'une source mantellique enrichie. Ce nouveau domaine mantellique, caractérisé par une composition isotopique de l'Hf non radiogénique et préservé dans le manteau profond, peu possiblement boucler le bilan de masse terrestre pour l'Hf et le Nd. Nos résultats indiquent que le manteau terrestre Archéen montrait une hétérogénéité isotopique (surtout pour l'Hf) beaucoup plus importante que le manteau actuel tel qu'échantillonné par les basaltes de types MORB et OIB. Cette hétérogénéité isotopique est semblable à l'hétérogénéité caractérisant les corps planétaires sans convection mantellique comme Mars et la Lune, et peut représenter un régime transitoire

hérité de la différentiation initiale de la Terre. Notre étude confirme donc qu'une telle hétérogénéité était toujours présente aux environ de 3 Ga, mais plus élusive dans les roches juvéniles d'âge <2.7 Ga. Les nouvelles données isotopiques de l'Hf ici présentées favorisent une source et origine communes pour les carbonatites, kimberlites et certain basaltes océaniques.

ABSTRACT

We report on the major element composition of a suite of kimberlite-hosted peridotite xenoliths from the northern margin of the western Archean craton of Greenland, as well as the isotopic composition (Nd, Sr and Hf) of carbonatites and kimberlites from eastern Canada and southwestern Greenland.

Our results indicate that the lithospheric mantle underneath the Sarfartoq area of southwestern Greenland extends to approximately 225 km, and consists of refractory (olivine Mg # >0.9) harzburgites and lherzolites. Moreover, the Sarfartoq peridotites are not characterized by the OPX enrichment observed in peridotites from the Kaapvaal craton of South Africa, and show more affinity with peridotites from east Greenland (Wiedemann Fjord), Somerset Island (Canadian arctic) and Tanzania. Detailed analyses of constituent minerals reveal that the lithospheric mantle underneath the Sarfartoq area is compositionally layered as follows: (1) an internally stratified upper layer (70 to 180 km) consisting of coarse, un-deformed, refractory garnet-bearing and garnet-free peridotites and, (2) a lower layer (180 to 225 km) characterized by fertile, CPX-bearing, porphyroclastic garnet lherzolites. The stratification observed in the upper refractory harzburgite layer (70-180 km) is reflected by an increase in fertility (e.g. lower olivine abundance and fosterite content) with depth. The sharp nature of the stratification may indicate a two-step process for the formation of this lithosphere, i.e. multistage growth of the lithospheric root.

In situ Sr isotopic compositions of coexisting apatite and carbonate for carbonatites from the Sarfartoq alkaline complex, Greenland, have been determined by laser ablation MC-ICP-MS. The combined total analyses (n=107) of apatite and carbonate yield $^{87}Sr/^{86}Sr$ compositions ranging from ~0.7025 to ~0.7031. This relatively large variation in Sr isotopic compositions (~0.0006) is significantly higher than the estimated external reproducibility (~0.000047; 2σ) of the method. The large range in $^{87}Sr/^{86}Sr$ values suggests that apatite and carbonate precipitated predominantly under non-equilibrium conditions. The isotopic variations observed within individual hand specimens may therefore reflect larger- (regional) scale open-system processes, possibly involving mixing of carbonatitic melts derived from distinct mantle sources, or from a common isotopically heterogeneous mantle. This analytical technique provides a rapid and effective approach to determine the extent of isotopic heterogeneity within a single sample or individual grains, with analytical precision approaching that obtained by conventional TIMS.

High-precision Hf isotopic analyses and U-Pb ages of carbonatites and kimberlites from Greenland and eastern North America, including Earth's oldest known carbonatite (3 Ga), indicate derivation from an enriched mantle source. This previously unidentified mantle reservoir of unradiogenic Hf isotopic composition, preserved in the deep mantle for at least 3 billion years, may account for the mass imbalance in Earth's Hf-Nd budget. Our results show that the Early to mid-Archean terrestrial mantle was isotopically much more heterogeneous (in particular for Lu/Hf) than the present-day mantle sampled by MORBs and OIBs. The isotopic heterogeneity observed in the early terrestrial mantle exhibits similarities to the poorly mixed mantles of planetary bodies such as Mars and the Moon and, as such, may represent a transient regime inherited from initial planetary

differentiation. Our study thus confirms that such isotopic heterogeneity was still present as late as around 3 Ga, but more elusive in <2.7 Ga mantle-derived rocks. The Hf isotopic data presented here support a common mantle source region and genetic link between carbonatite and some oceanic island basalt (OIB) volcanoes.

TABLE OF CONTENTS

TABLE OF CONTENTS (CONTINUED)

TABLE OF CONTENTS (CONTINUED)

LIST OF FIGURES

CHAPTER I

LIST OF TABLES

CHAPTER I

CHAPTER II

CHAPTER III

GENERAL INTRODUCTION

Because of the lack of geological material older than 4 Ga, it is not known when and how modern-style geologic processes overprinted the initial chemical fractionations left by planetary accretion. Understanding the chemical and isotopic secular evolution of Earth's mantle is thus essential in order to evaluate early planetary differentiation processes. The extent and degree of mantle depletion in the Early Archean is not fully understood, since data from separate regions seem to indicate a different history. Other outstanding problems are the mechanisms by which deep buoyant sub-continental roots were created and preserved throughout most of the planet's history. The potential contribution of these lithospheric roots to continental volcanism by interaction with up-welling mantle material such as deep-seated plumes remains elusive. Such questions can be addressed through the study of magmas originating at deep levels in the mantle and/or mantle-fragments that are occasionally brought-up to the surface of the planet in the form of inclusions in kimberlites. Until recently, our knowledge of the sub-continental mantle mainly relied manly on mantle fragments included in diamondiferous kimberlites from South Africa. The recent discoveries of new kimberlite provinces in the Northern Hemisphere have provided a chance to investigate the nature of mantle roots from this region and to assess lithospheric growth models. Preliminary results from these studies have outlined significant compositional differences between different cratonic areas, which may reflect distinct petrogenetic conditions.

To this effect, we have studied the Sr, Nd and Hf isotope systematics of kimberlites and carbonatites from Greenland and Canada in order to constrain the isotopic evolution of Earth's mantle through time. In addition, we have studied the major element composition of

a suite of mantle-derived peridotites from Greenland to better understand lithosphere stabilization processes. This also enabled us to evaluate the contribution of the sub-continental mantle to carbonatite and kimberlite volcanism. The large spread in age of the samples studied, i.e. from 3 to 0.2 billion years, not only provides us with an unsurpassed opportunity to monitor secular changes in the isotopic composition of the mantle, but also offers the possibility to investigate the nature of the Mid-Archean (3 Ga) mantle.

In the first portion of the thesis, we document the nature of the sub-continental mantle under the North Atlantic craton. Our results indicate that the North Atlantic sub-continental mantle differs in major element composition and structure from the Kaapvaal craton of South Africa, and we have interpreted these distinctions as reflecting different styles of lithosphere formation (mantle growth). Because South Africa is one of the largest diamond producing areas in the world, understanding the relationships between styles of lithosphere formation and diamond preservation is essential in targeting areas for diamond exploration. This portion of the thesis thus has an important impact in the field of economic geology.

Secondly, we have used new technology (multicollector inductively coupled plasma mass spectrometer interfaced to a laser system) in order to document in-situ Sr isotopic compositions of coexisting apatite and carbonate for carbonatites from the Sarfartoq alkaline complex, Greenland. This new technique enables us to look not at only at variations between coexisting minerals, but also to investigate potential intra-mineral disequilibrium. This study is the first to examine the extent of Sr isotopic homogeneity amongst coexisting igneous minerals containing high Sr (>3000 ppm) and low Rb (1<< ppm) contents within a single petrographic thin section mount. Our results show that apatite

and carbonate record a large range in $^{87}Sr/^{86}Sr$ values, suggesting that these minerals precipitated predominantly under non-equilibrium conditions. The isotopic variations observed within individual hand specimens may therefore reflect larger- (regional) scale open-system processes, possibly involving mixing of carbonatitic melts derived from distinct mantle sources (e.g. plume vs. lithosphere), or from a common isotopically heterogeneous mantle.

In the last part of the thesis, we have integrated new technology and analytical procedures (plasma source mass spectrometry and Lu-Hf geochemistry) to the study of carbonatites and kimberlites. In the course of this research, we document Earth's oldest known carbonatite (3 Ga) and demonstrate that carbonatites and kimberlites are derived from a previously unidentified deep mantle reservoir possibly isolated from the convective mantle. These results have important ramifications for isotope geochemistry because the existence of such a reservoir can reconcile the mass imbalance in the terrestrial Nd-Hf elemental budget. In addition, the extreme heterogeneity of the Archean terrestrial mantle documented in this study bears similarities with the poorly mixed mantles of planetary bodies such as the Moon and Mars, and may represent a transient regime inherited from initial planetary differentiation. Our study suggests that this isotopic heterogeneity was still present as late as 3 Ga, but more elusive in <2.7 Ga mantle-derived rocks.

CREDITS

This thesis consists of three chapters written in 'paper' style in order to accelerate publication of the results and ideas presented in this thesis. Chapters two and three are in press in the journals *Geochimica et Cosmochimica Acta* and *Geology*, respectively, while chapter one has been submitted to *Journal of Petrology* and is presently being revised. All papers have been written by the author of this thesis, and all ideas presented are genuinely his. Ross K. Stevenson, who supervised the thesis, guided and helped the author to stay focused on the objectives of the study throughout the course of this thesis. Antonio Simonetti was responsible for the developmental work regarding plasma source mass spectrometry and laser ablation analyses presented in chapters two and three, and also participated in the interpretation of the data. Jean David participated in chapter three of the thesis, by helping the author with the U-Pb chemistry and thermal ionization mass spectrometry. Lastly, Stephan Kurzlaukis assisted the author in collecting samples in the field during the summer of 2000.

Chapter I

Composition of the Lithospheric Mantle under the NorthAtlantic Craton: Evidence from Peridotite Xenoliths of the Sarfartoq area, Southwestern Greenland

Martin Bizzarro and R. K. Stevenson

GEOTOP Center, Université du Québec à Montréal, succursale Centre-ville, PO box 8888, Montréal, Québec, Canada, H3C 3P8.

ABSTRACT

The composition and thermal state of the lithospheric mantle under the North Atlantic craton was investigated using a suite of peridotite xenoliths from the diamond-bearing Sarfartoq kimberlite dike swarm of South Western Greenland. Elevated olivine and whole-rock Mg# (>0.9) attest to the refractory nature of the Sarfartoq mantle showing comparable degrees of depletion to other cratonic roots. Modal analyses indicate that the Sarfartoq mantle is not typified by the orthopyroxene enrichment observed in the Kaapvaal and Siberian cratonic roots, but shows more affinity with the Canadian Arctic (Somerset Island), Tanzania and East Greenland (Wiedemann Fjord) peridotites. Geothermobarometric data indicate that the Sarfartoq peridotites have equilibrated at temperatures and pressures ranging from 660 to 1280 C and from 2.2 to 6.3 GPa, and lie on an elevated conductive geotherm (50 mW/m^2) with a modeled crustal thickness of 45 km and heat production of 0.8 $\mu W/m^3$. In addition,the lithospheric mantle underneath the Sarfartoq area is compositionally layered as follows: (1) an internally stratified upper layer (70 to 180 km) consisting of coarse, un-deformed, refractory garnet-bearing and garnet-free peridotites and, (2) a lower layer (180 to 225 km) characterized by fertile, CPX-bearing, porphyroclastic garnet lherzolites. The stratification observed in the upper refractory harzburgite layer (70-180 km) is reflected by an increase in fertility (e.g. decrease in olivine abundance and fosterite content) with depth. The sharp nature of the boundary beetween the upper and lower layers may indicate multistage growth of the lithospheric mantle.

1.1 INTRODUCTION

The sub-continental mantle is a heterogeneous geochemical reservoir of considerable mass and volume, extending for more than 300 km below some Archean cratons (Jordan, 1975). Dating of melt depletion events with the the Re-Os chronometer has showed that continental roots have existed for extensive periods of time, perhaps as long as the overlying crust (>2.5 Ga, Pearson, 1999). Because of it's mass and age, this reservoir could play an important role in balancing the terrestrial trace element budget. For example, Griffin et al. (2000) recently proposed that the so-called missing Hf reservoir of Blichert-Toft and Albarède (1997) lies within the sub-continental mantle. Although the petrogenesis of the lithosphere under oceans is well explained through low-pressure melt extraction, the origin of the continental equivalent is still under debate. Certain geodynamic models emphasize the importance of the stabilization of the first continental roots in preserving early Archean crust from mantle recycling (e.g. Bowring and Housh, 1995). An understanding of the petrogenesis and subsequent evolution of this reservoir is thus imperative in deciphering the early history of the Earth. Cratonic lithospheric growth models include (1) restite from high-pressure komatiitic melt extraction (Boyd and Mertzman, 1987; Boyd, 1989; Walter, 1998), (2) melt-rock interactions (Kelemen et al., 1992; Rudnick et al., 1994; Kelemen et al, 1998), (3) mechanical/metamorphic sorting (Boyd, 1989; Boyd et al., 1997), (4) exsolution (Canil, 1991), (5) majorite fractionation (Herzberg et al., 1988), (6) mantle overturns (Griffin et al., 1998; Griffin et al., 1999), (7) fluid metasomatism (Kesson and Ringwood, 1989) and (8) melting of a meteoritic protolith (Herzberg, 1993). Until recently, these models were solely based on classical xenolith

suites from southern Africa and, to a lesser extent, Siberia and Tanzania. The recent discoveries of kimberlites in North America and Greenland have provided information on the nature of the mantle under the Slave, Superior and North Atlantic cratons through the study of their hosts xenoliths. Preliminary results from these studies suggests isotopic (Bizzarro et al., 1999) and compositional (Berstein et al., 1998; Kopylova et al., 1999; Boyd and Canil, 1997; McKenzie and Canil, 1999; Schmidberger and Francis, 1999) differences between North American, Greenlandic and South African suites, that may potentially reflect different styles of lithosphere growth.

The main objective of this study is to investigate the nature of the sub-continental mantle under the North Atlantic Craton (NAC) using a suite of kimberlite-borne xenoliths from the Sarfartoq area of southwestern Greenland (fig. 1). We define the major element composition of the lithospheric mantle through whole-rock and mineral analyses of the peridotites, which further enables us to determine a geothermal gradient for the Sarfartoq area at the time of kimberlite magmatism. This new data set is compared with well-documented peridotite compositions of other Archean cratonic areas such as the Kaapvaal (South Africa), allowing the evaluation of potential lithospheric growth models.

1.2 GEOLOGICAL SETTING

The xenoliths investigated in this work are derived from the Sarfartoq kimberlite dike swarm of southwestern Greenland (Larsen and Rex, 1992; Mitchell et al., 1999). Alluvial diamonds have been reported in the past from the Sarfartoq area (Brunet, 1974; 1976), and recent discoveries of in situ deposits have renewed mineral exploration activities in this area (Minex, 1998). The Sarfartoq swarm is located on the western coast of Greenland, southwest of the town of Kangerlussuaq (Søndre Stromfjord) and northeast of

the Sukkertoppen ice cap, and centered on the Sarfartoq carbonatite complex (fig. 1). Radiometric dating (K-Ar on micaceous minerals) has constrained the age of kimberlite intrusion to ca. 600 Ma, i.e. contemporaneous with the episode of the Sarfartoq carbonatite magmatism (Larsen et al., 1983). Although field relations suggest that kimberlite emplacement postdates the carbonatite intrusion event (Larsen and Rex, 1992), it has yet to be confirmed by precise geochronology. The Sarfartoq swarm is intruded into highly metamorphosed Precambrian gneisses and the dikes straddle the boundary between the southern front of the Proterozoic Nagssuqotidian orogen and un-reworked Archean units of the Greenland Western Archean craton. The Nagssuqotidian Orogen trends east-northeast and consists of Archaean tonalitic and granodioritic orthogneisses interleaved with Proterozoic orthogneisses and supracrustal units (Kalsbeek et al, 1987; Kalsbeek and Nutman, 1996). The orogen represents the collision between two Archaean continents and is temporally constrained between 1850 and 1800 Ma (Kalsbeek and Nutman, 1996). The region south of the Nagssuqotidian front comprises three distinct Archean terrains mainly composed of granulite facies orthogneisses, with locally abundant supracrustal rocks. The terrains, which include Early (> 3600 Ma) to late Archean components, were assembled at ca. 2800 to 2700 Ma and thus acted as a stable craton during Nagssuqotidian orogeny (Rosing et al., 2001).

1.3 MATERIAL AND ANALYTICAL PROCEDURE

Peridotite xenoliths were collected from two different dikes of the Sarfartoq kimberlite dike complex, located within undisturbed Archean gneisses (fig. 1). The xenoliths are fresh and vary in size from about 5 to 45 cm, and consist of spinel-facies and garnet-facies peridotites. The dikes show unusual sedimentological-like textures reflecting

their complex intrusive histories (Kurszlaukis and Bizzarro, submitted). In this respect, the xenoliths tend to be concentrated in specific areas of the dikes resembling cumulate phases. Some of the xenoliths appear to have experienced interaction with the host magma as implied by the presence of secondary volatile rich phases such as phlogopite mantling garnet, clinopyroxene (CPX) or spinel. Xenoliths were separated from the kimberlite host rock with the use of a mechanical saw. The freshest material from the center of the larger specimens was thus selected for geochemical analyses. Major element compositions of xenoliths were determined with a Philips PW 1400 X-ray fluorescence (XRF) spectrometer using 10-15 grams of powdered rock, while the major element compositions of mineral phases were determined with a JEOL 8900 super microprobe (both at McGill University, Montréal, Canada). Microprobe analyses were conducted with an acceleration voltage of 15 KV and beam current at 5×10^{-8} A, and the diameter set at 5 μm. Uncertainties for major (>5%) and minor (<5%) oxides analyzed by microprobe are better than 2% and 5% of quoted values. Instrument calibration was done with natural mineral standards of similar elemental composition to the samples analyzed. Results were processed online by a ZAF (JEOL) correction program. XRF analyses of major oxides and certain trace elements (Ni, Cr) were determined from fused beads prepared from ignited samples. Rb and Sr XRF analyses were determined from pressed powder pellets. Detection limits for trace elements are as follows: Ni (3 ppm), Cr (15 ppm), Rb (1 ppm) and Sr (1 ppm). Uncertainties for major (>5%) and minor (<5%) oxides determined by XRF are better than 2% and 5% of quoted values, respectively. Modal mineral abundances for xenoliths were calculated by balancing whole rock and mineral phases compositions (Walter, 1998). This is done by

solving for x in the matrix equation $A \bullet x = b$, where A is an M by N matrix composed of N phase and M components, x is the solution vector and b is the known vector.

1.4 RESULTS

1.4.1 Petrography and mineral chemistry

The terminology used for the different rock textures is after Harte (1977). Lherzolite vs. harzburgite assignment is based on the presence or absence of clinopyroxene, respectively.

1.4.1.1 Garnet facies peridotites

The garnet-bearing lithologies can be separated in two groups based on their mineralogy and texture. The first group consists of CPX-depleted coarse equant garnet harzburgites (fig. 2a and b) while the second group comprises more fertile, porphyroclastic garnet lherzolites (fig. 2c and d). The harzburgites show anhedral to sub-euhedral cracked olivine crystals with irregular to curvilinear grain boundaries, ranging in size from 2 to 20 mm. Pink garnets occur as euhedral grains (<5 mm) always mantled by phlogopite and small euhedral spinels (<0.5 mm), while the OPX commonly show tabular habits with straight grain boundaries. Garnet is infrequently observed as inclusions in OPX and olivines. Although CPX has not been observed in polished sections for this rock type, it has been noted as a rare phase during mineral separation procedures at high magnification, and its abundance is estimated to be always less than 1%. The average modal abundances for the garnet harzburgites are 84 % olivine, 8 % OPX and 8 % garnet. Spinel was observed in textural equilibrium with garnet in sample SAF-06.

The lherzolites show large porphyroclasts of garnet, CPX, OPX and rare olivine, set in a matrix of smaller euhedral crack-free olivine neoblasts (<2 mm) with straight grain

boundaries. The average modal abundance for this rock type are 79 % olivine, 7 % OPX, 8 % CPX and 6 % garnet. Garnet appears as a purple sub-circular phase while the CPX are emerald green tabular crystals. Garnet is the most abundant porphyroclast, ranging in size from 0.5 to 1 cm, while the CPX are smaller (0.5-0.8 cm), less frequent, usually aligned along a deformation plane inducing a weak fluidal texture to the rock. OPX porphyroclasts are commonly < 1 cm, showing euhedral habits. Olivines from the harzburgites and lherzolites have average Mg# (molar Mg/(Mg+Fe)) of 0.918 and 0.913 respectively. The lower Mg# of the Sarfartoq deformed lherzolites are consistent with similar lithologies from the Slave, Kaapvaal and Siberian cratons (Boyd, 1989; Boyd et al., 1997; McKenzie and Canil, 1999; Kopylova et al., 1999).

Compared to other cratonic suites, olivines from the Sarfartoq garnet harzburgites have lower average Mg#. NiO contents of olivines from garnet harzburgites correlate positively with Mg#, showing comparable values to the garnet-free peridotites (fig. 3a). The olivines from the Sarfartoq deformed garnet lherzolites have much lower NiO abundance than coarse garnet and garnet-free peridotites. Garnets from the Sarfartoq peridotites are Cr-pyropes with Cr_2O_3 contents ranging from 3.5 to 4.5 wt.%, and CaO ranging from 1.3 to 5 wt.%. Garnets from coarse harzburgites are easily distinguished from deformed lherzolites by having significantly lower TiO_2 and CaO abundances; harzburgitic garnets also show a wider Cr_2O_3 and CaO compositional range. OPX from the harzburgites are enstatites with low Al_2O_3 contents (<1 wt.%). Their overall composition is similar to the Sarfartoq garnet-free peridotites as well as garnet peridotites from other cratonic suites (Kaapvaal, Boyd, 1989; Slave, McKenzie and Canil, 1999; Kopylova et al., 1999; Siberia, Boyd et al., 1997;Tanzania, Lee and Rudnick, 1999). OPX from garnet lherzolites have

more fertile compositions than harzburgitic samples, characterized by higher Al, Ti, Ca and lower Mg contents. CPX from the garnet lherzolites are Cr-diopsides, and compositionally distinct from CPX from spinel facies lherzolites or rare CPX from garnet harzburgites, as they are characterized by much lower Cr and Na contents (fig. 4a). Transects were conducted along garnet and pyroxenes grains of both coarse harzburgites and deformed lherzolites to investigate potential chemical zoning. Figure 5 shows the results for garnets from two distinct lherzolite and harzburgite samples, respectively. The two garnet lherzolites have well-developed zoning for TiO_2, CaO, Al_2O_3, MgO and FeO. The shape of the profiles is sinusoidal for both samples, characterized by a reversal of the gradient from core to rim. Likewise, TiO_2, CaO, MgO and FeO contents are also zoned in the garnet harzburgite, but the shape of the profile is either concave of convex, i.e. with a steady increase/decrease from core to rim. In addition, the range of chemical variation observed in garnet harzburgite is roughly 1 wt% for FeO, MgO and CaO, and 0.25 wt.% for TiO_2. Except for TiO_2, major oxide variation in the garnet lherzolites is approximately 0.5 wt.% for FeO, MgO, Al_2O_3 and CaO. Transects conducted along OPX grains from either harzburgites or lherzolites did not show any significant chemical variations. In contrast, CPX from the lherzolites are chemically zoned for Na_2O, MgO, TiO_2, FeO and CaO (Fig 6). Unlike garnet form this rock type, the shape of the profile is either concave of convex. For both garnet and CPX, the chemical variation is not correlated with mineral surface features.

1.4.1.2 Garnet-free peridotites

Three rock types are recognized within the garnet-free peridotites, i.e. dunites, harzburgites (fig. 2e) and lherzolites (fig. 2f). Sarfartoq garnet-free lherzolites commonly

possess a coarse equant texture (terminology of Harte, 1977) typified by coarse (2-5 mm) anhedral to sub-euhedral cracked olivines with curvilinear grain boundaries. The average modal abundances of these lherzolites are 91% olivine, 7% OPX (orthopyroxene), 2% CPX and <1% spinel. The OPXs appear as elongate euhedral crystals, which may sometimes be corroded, and range in size from 1-2 mm, while the CPX are smaller (<0.5 mm) euhedral emerald green crystals often associated with OPX. Both phases are commonly mantled by phlogopite. Spinels are opaque and of small size (<0.2 mm), observed at olivine triple junctions or as inclusions within olivine crystals. The average modal abundances for harzburgite are 92% olivine, 6% OPX and 2% spinel. The olivines are coarse (2-4 mm), cracked, showing sub-euhedral to anhedral habits with irregular to curvilinear grain boundaries. OPX show sub-euhedral to anhedral habits, and are of relatively small size (<1 mm). Spinel grains range from 0.1-2 mm, are opaque with circular or elongated habits and located at olivine triple junctions points or as inclusions within olivine crystals. Dunites show almost mono-mineralic assemblages with the exception of spinel and rare CPX. They are typified by a coarse equant texture, large (1 cm) sub-euhedral cracked olivines with curvilinear to irregular grain boundaries. The olivines from the lherzolites, harzburgites and dunites have indistinguishable average Mg# of 0.926, 0.922 and 0.920, respectively. These values are consistent with the Mg# of garnet-free peridotites from other cratonic suites such as the eastern Greenland Wiedemann Fjord spinel harzburgites (0.927; Bernstein et al, 1998), the Kaapvaal and Siberian spinel peridotites (0.928; Boyd et al, 1997), spinel lherzolites of the Slave craton (0.924; McKenzie and Canil, 1999) and garnet-free peridotites from Tanzania (0.925; Lee and Rudnick, 1999). NiO contents of the olivines vary from 0.322 to 0.425 wt. %, almost identical to values reported for the Wiedemann

fjord spinel harzburgites (Bernstein et al., 1998) and comparable to averages from Tanzania as well as the Slave and Siberian cratons (Lee and Rudnick, 1999; Pearson et al., 1999; McKenzie and Canil, 1999; Kopylova et al, 1999; Boyd et al, 1997), but much lower than low temperature peridotites from the Kaapvaal (Boyd et al, 1997).

OPX are aluminous enstatite with Al_2O_3 contents ranging from 0.5 to 4 wt.%. Although one sample (SAF-13) has Al_2O_3 content similar to spinel-bearing samples from other cratonic suites (1-5 wt.%), most OPX of the Sarfartoq garnet-free peridotites have low aluminum compositions (< 1%) typical of OPX from garnet facies peridotites (fig. 4b), as well as the OPX from the garnet-free peridotites from Tanzania (Lee and Rudnick, 1999). CPX are Cr-diopsides with variable amounts of Cr_2O_3 (0.6-4%), Al_2O_3 (0.1-3%) and Na_2O (0.7-3%). Al_2O_3 correlates positively with Na_2O, and the coarse spinel and garnet bearing peridotites plot towards the high Al and Na end of the trend, while the porphyroclastic garnet lherzolites plot towards the lower part of the array (fig. 3a). A second population represented by low Cr and Na is present, showing compositional similarities with secondary diopsides from Siberia described by Boyd et al. (1997). Unlike these small (100 μm) secondary diopsides from Siberia which crystallized as discrete grains growing along the contact between OPX and olivine, the secondary Sarfartoq population is characterized by individual crystals associated with spinel and OPX and in places replacing OPX. Similar CPX have been described by Dawson (1999).

Spinels from Sarfartoq are Mg-chromites with high Cr_2O_3 (43.6-63.1%), relatively high TiO_2 contents (0-3.8%), and low Al_2O_3 abundances (0.5-16.5%), with most having Cr# > 80. The average Cr_2O_3 content of the Sarfartoq spinels (58.4 wt.%) is high compared to other published North American and Greenland spinel facies peridotites (McKenzie and

Canil, 1999; Kopylova et al, 1999; Berstein et al., 1998), with a good proportion of the population plotting within the diamond inclusion field of Gurney and Zweistra (1995) in the Cr-Mg chemical space (not shown). The high-Cr and low-Al abundances of the Sarfartoq spinels resemble those from garnet peridotites of the Slave craton (McKenzie and Canil, 1999; Kopylova et al, 1999) and the Canadian Arctic (Zhao et. al, 1997), as well as the spinels from garnet-free peridotites from Tanzania (Lee and Rudnick, 1999). In the olivine-spinel mantle array (OSMA) of Arai (1994), the Sarfartoq spinel peridotites plot in the high-Cr # and high-Fo olivine part of the trend (fig. 7a). The OSMA array is interpreted as a restite trend because Fo in olivine and the Cr# of spinel correlate positively with the degree of melting (Irvine, 1965). Similarly, in the spinel Cr#-Mg# chemical space, the Sarfartoq spinels plot towards high-Cr# and lower Mg# (fig. 7b), compositionally close to spinels from garnet peridotite. Transects were conducted along two spinel grains from sample SARF-39 to investigate potential chemical zoning. Results (Fig. 8) indicate that spinels have well-developed zoning for FeO, Cr_2O_3 and MgO. The Cr_2O_3 and MgO concentration increases from core to rim, while it decreases for FeO.

1.4.1.3 Ilmenite bearing dunites

Ilmenite bearing dunites show gradual variation between coarse, porphyroclastic and granuloblastic textures, indicating variable degrees of deformation. These rocks are dominated by the presence of olivine, with minor ilmenite and traces of spinel. Olivine morphology is variable and evidently related to the degree of deformation of the rock in which it occurs. It can thus show euhedral coarse (>2 mm) habits with curvilinear grain boundaries in coarse equant rock types, to small (<2 mm) crack-free anhedral habits with straight grain boundaries in granuloblastic lithologies. Ilmenite and spinel occur as small

blebs or pockets (< 1 mm) at olivine grain boundaries, commonly in textural equilibrium. Olivine compositions are much less forsteritic than garnet or spinel facies peridotites, as the Mg# varies from 0.858 to 0.903 (fig. 3). These olivines are thus atypical of olivines from peridotites generated through melt extraction processes, but resemble groundmass olivine found in kimberlites (Mitchell, 1986). Spinels from this rock type are also atypical of peridotite spinels, having higher TiO_2 and FeO contents. Core-rim analyses for these spinels showed intense compositional variations, with rims having re-equilibrated to much lower Cr_2O_3 and higher TiO_2 and FeO contents. Moreover, these spinels are very similar to spinels from magmatic trend 2 described by Mitchell (1986), believed to be representative of a magma undergoing extensive phlogopite precipitation. Ilmenites have high contents of MgO and moderate Cr_2O_3 abundances (1-6 wt.%). They are thus close to kimberlitic groundmass ilmenites described by Mitchell (1986), who also mentions the common presence of ilmenite-spinel intergrowths, which are observed in the Sarfartoq ilmenite-dunites. Furthermore, core-rim analyses of kimberlite groundmass ilmenites (Mitchell, 1986, table 6.12) show those rims are typified by Mg depletion and Ti enrichment, as observed in this study. One specimen shows the presence of OPX and olivine igneous layering. The compositions of these OPX are quite distinct from the OPX present in the spinel and garnet facies peridotites, having higher Ca, Ti and Fe abundances. Lee and Rudnick (1999) have described Fe-rich dunites from Tanzania that contains olivines with comparable Mg# to the ilmenite-dunite olivines here described.

1.4.2 Major element compositions

Selected major and trace element whole-rock compositions of the Sarfartoq peridotites are presented in Table 1. Whole rock Mg# for the Sarfartoq suite are

summarized in figure 3b. The Sarfartoq averages are comparable to those of other cratonic suites and significantly more refractory than most peridotites from oceanic or alpine settings. The depletion in basaltic components such has Al, Fe, Ti, and Ca compared to primitive mantle models testifies to the refractory nature of the Sarfartoq mantle at the time of kimberlitic magmatism. In figure 9, incompatible elements such as Fe, Al, Ti and Ca, are plotted against MgO and are used as proxies to estimate the degree of partial melting for the different rock types of the Sarfartoq suite. Incompatible elements demonstrate negative correlations with MgO while a positive correlation is observed with compatible Ni, suggesting that the peridotite suite is related through melt-extraction processes. When compared to the global peridotite trend, the Sarfartoq peridotites plot towards the end of the array. As expected from the mineral chemistry data, the garnet-free peridotites plot towards the more depleted end of the melt extraction arrays. Garnet-free peridotites have the highest MgO contents and show the least internal variation, while analyses of garnet facies rocks are more variable. The ilmenite bearing dunites diverge from the worldwide peridotite trend for most elements.

1.5 DISCUSSION

1.5.1 Elemental zoning

Griffin et al. (1989) suggested that the chemical heterogeneities preserved in garnets from mantle peridotites may be generated by two distinct processes: (1) inward diffusion of chemical components from rims of stable garnet grains, or (2) overgrowth of garnet cores by rims of different compositions, followed by diffusive equilibration across the core-rim boundaries. Based on the shape of the diffusion profiles, they ascribed the zoning preserved in garnets from some deformed peridotites of South Africa to peripheral overgrowth on

primary cores. Alternatively, other studies have also suggested that the zoning recorded by garnet porphyroblasts in deformed lherzolites can be explained by melt-related inward diffusion of chemical components (e.g. Shizimu, 1999).

The chemical zoning present in garnets from the Sarfartoq harzburgites is overall similar, characterized by rimward increase in TiO_2, CaO and FeO (fig. 5). Unlike the garnet grains described by Griffin et al. (1989), the profiles of the Sarfartoq harzburgitic garnets do not show inflection points and may thus be modeled by simple binary diffusion. Using a model of diffusive penetration into a sphere of constant composition (Crank, 1975), the Ti and Fe zoning present in harzburgitic garnets may be approximated by Dt/a2 values of 0.03 and 0.06, respectively, where D is the diffusion coefficient (m/s), a is the grain radius (m) and t is time (s) (fig. 10). Using diffusion coefficients of 3.3×10^{-19} to 2.7×10^{-18} m^2/s for Fe (Gangully et al., 1998), time scales for diffusional relaxation are in order of 25 to 250 years for the harburgitic garnets. These time scales are similar to those reported for Kaapvaal (Griffin et al., 1989) and Siberian (Shizimu, 1999) zoned garnets from high-temperature peridotites.

The zoning patterns present in garnets of the porphyroclastic lherzolites are complex, with correlated reversal of the Ti, Al, Ca, Mg and Fe chemical gradients (fig. 5). These profiles may not be explained by simple inward diffusion, or overgrowth of cores by rims of different compositions as described by Griffin et al. (1989). The Ti, Ca and Fe profiles are characterized by an initial rimward depletion followed by an increase in concentrations, while the Al and Mg profiles show an inverse pattern. The initial depletion in Ti, Ca and Fe coupled with the increase in Mg and Al bears similarities with melt-extraction trends observed in peridotitic garnets from melting experiments at pressures

above 4 GPa (Walter, 1998). In this respect, the complex zoning pattern observed in these garnets may have occurred via a two step process, with an initial melt depletion event followed by re-fertilization through melt-related diffusional exchange of chemical components, as argued for the harzburgitic garnets. Although it is difficult to constrain the timing of the re-fertilization event in relation to the depletion, diffusion kenetics indicate that the zoning preserved in the inner part of the grain (decrease in Ti, Fe and Ca; increase in Al and Mg) is a relatively young feature.

Clinopyroxene crystals from high temperature peridotites show compositional heterogeneity characterized by rimward increase in CaO and decrease in Na_2O and FeO (Fig. 6). This zoning pattern is not easily reconciled by the interaction of the crystal with a melt and may reflect disequilibrium related to a change in temperature and/or pressure. Using the *two-pyroxene* thermometer of Brey and Köhler (1990), potential temperatures gradients between cores and rims were investigated. The results indicated that crystal rims consistently have last equilibration temperatures ~100 °C lower than the cores. As such, the core-rim increase in the Ca/Fe ratio may reflect a decrease in temperature due to to partial equilibration of the pyroxene crystals during ascent of the peridotite nodule.

1.5.2 Thermal structure of the NAC lithosphere

A combination of published geobarometers and geothermometers were used to calculate last equilibration pressures and temperatures (P-T) of the xenolith suite following the iterative procedure of Brey and Köhler (1990). Equilibration P-T arrays of garnet bearing lherzolitic lithologies were calculated by combining the *two-pyroxene* thermometer and the *Al in OPX* barometer of Brey and Köhler (1990), while the P-T conditions of garnet facies harzburgites were computed by combining the *Ca in OPX* thermometer and the *Al in*

OPX barometer of Brey and Köhler (1990). Temperature estimates obtained with the *Ca in OPX* and *two-pyroxene* thermometers were within 50°C. Results are presented in table 4, and show that the Sarfartoq peridotites have equilibrated at pressures and temperatures ranging from 2.2 to 6.5 GPa and 650 to 1300 C. Deformed, porphyroclastic garnet lherzolites have equilibration temperatures higher than 1100 C while the coarse garnet harzburgites show temperatures lower than 1100 C. All porphyroclastic garnet lherzolites have equilibrated within the diamond stability field, but only a small proportion of the coarse garnet harzburgites show such high equilibration pressures.

To constrain the P-T regime of the Sarfartoq mantle at the time of kimberlite magmatism, we have used an approach similar to Rudnick and Nyblade (1999). A regression of the P-T data yields temperature estimates for the base of the crust for four different models of crustal thickness of 40, 45, 50 and 55 km (table 4). From this, the surface heat flow can be solved with the following equation (Fowler, 1990):

$$T_{base} = T_0 + \frac{q_0 D}{K} - \frac{AD^2}{2K}$$

Where T_{base} is the temperature at the base of the crust determined by extrapolation, T_0 is the surface temperature (0 C), D is the thickness of the crust, and A and K are respectively the crustal heat production and the thermal conductivity. There is presently no information on crustal heat production for the Sarfartoq area, and we have therefore chosen to use average values of 0.6, 0.7 and 0.8 from Rudnick and Nylblade (1999). We have adopted a value of 2.5 for crustal thermal conductivity, but because this parameter is expected to increase in the lithospheric mantle, a temperature dependent model was considered instead (Jaupart

and Mareschal, 1999). Once the surface heat flow is constrained, we can deduce the mantle heat flow through the following relationship (Pollack and Chapman, 1977):

$$q_0 = q_m + AD$$

Where q_0 is the surface heat flow, q_m is the reduced heat flow which represents the mantle heat flow, while A and D are respectively the crustal heat production and thickness. All values used and results of the thermal models are presented in Table 4, and shown in fig. 11. Of the 12 models depicted in Table 4, only the model assuming a 45-km crust and a 0.8 $\mu W/m^3$ heat production values fits the observed data. The mantle heat flow derived from this model, 14 mW/m^2, is in accordance with values reported by Jaupart and Mareschal (1999) for the Superior province. Moreover, our Moho temperatures are evidently higher than those from the Abitibi province (Jaupart and Mareschal, 1999) because of the greater crustal thickness in the Sarfartoq model. The 50 mW/m^2 surface heat flow derived from our model is relatively elevated compared to values from the Eastern Abitibi province (28 mW/m^2), but closer to the Western Abitibi values (52 mW/m^2). It is important to stress that these values are controlled by the crustal heat production and thickness, since we have assumed that the lithospheric mantle is not producing heat and the Moho heat flow represents the heat flow at the base of the lithosphere. Comparison of the Sarfartoq values with the Somerset Island data (Schmidberger and Francis, 1999) shows that both xenolith suites lie on the same P-T array, apart from the inflected nature of the Sommerset geotherm at high temperatures. Given the 90 Ma age of the Sommerset Island kimberlites, this suggests a similar thermal state for both mantles and stable thermal conditions for approximately 500 Ma. The location of the base of the lithosphere can be approximated by

the intersection of the conductive lithospheric and the isentropic oceanic temperature profiles (Jaupart and Mareschal, 1999). This overestimates the true lithosphere thickness (where heat is transported by conduction), because this model represents the lower limit of a boundary layer between conducting and convecting heat transport, which has been estimated to be in the order of 40 km (Jaupart and Mareschal, 1999). We thus derive a lithosphere thickness of roughly 220-225 km for the Sarfartoq area at the time of kimberlite magmatism.

1.5.3 Petrogenesis of the Sarfartoq peridotites

As outlined previously, the Sarfartoq peridotites can generally be separated in four groups: (1) CPX-free garnet harzburite, (2) garnet-free peridotites, (3) fertile CPX-rich, deformed lherzolites and, (4) ilmenite bearing dunites. The mineral chemistry of the ilmenite dunites is suggestive of a cumulate origin (section 1.4.1.3). However, similar lithologies from the Tanzanian lithosphere (Lee and Rudnick, 1999) are believed to be the products of melt-interaction based on high Re and Os abundances (Chesley et al., 1999). Figure 12a shows the Cr_2O_3 and FeO contents (wt.%) of spinels from the ilmenite dunites discussed in this study, as well as the Fe-rich dunites from Tanzania (Lee and Rudnick, 1999) and the refractory Sarfartoq garnet-free peridotites (this study) and Wiedeman fjord harzburgites. Magmatic spinels from kimberlites (Mitchell, 1995) are also plotted. The chemical variations present in both the ilmenite dunites (this study) and Fe-rich peridotites (Lee and Rudnick, 1999) bear similarities with trends observed for magmatic spinels from kimberlites. In addition, correlated increases in FeO and TiO_2 observed in these lithologies are found in magmatic spinels from kimberlites (Fig. 12b). The trends observed for spinels from the Sarfartoq ilmenite dunites are thus not easily reconciled with an origin via melt-

rock interaction. Thus, both the whole-rock and mineral chemistry of the ilmenite dunites are more easily explained by precipitation from a parental melt undergoing olivine fractionation (i.e. a cumulate origin).

Major element chemistry of the other peridotite types has demonstrated that they are depleted in basaltic components relative to primitive mantle estimates, and can be interpreted as residues from melt extraction events. Although similar to other cratonic areas in terms of depletion (olivine and whole-rock Mg#), the Sarfartoq peridotites are distinct in their high modal olivine contents (75 to 90%), low SiO_2 and hence low OPX modal abundances (< 20%). In this respect, they are compositionally more similar to the Wiedeman fjord spinel harzburgites (Berstein et al., 1998), the Tanzanian peridotites (Lee and Rudnick, 1999) and, to a lesser extent, the Sommerset Island garnet peridotites (Schmidberger and Francis, 1999).

The melting conditions that lead to the formation of depleted cratonic peridotites are subject to debate. For example both low (<3 GPa) and high (>7 GPa) pressures have been proposed for the formation of the Kaapvaal lithosphere (Kelemen et al., 1998; Walter, 1998). Recent experimental melting of fertile peridotite KR4003 (West Kettle River; Xue et al., 1990) at mantle conditions (Walter, 1998) allows comparisons with natural systems and assessment of conditions and degrees of melt extraction. Walter (1998) experimentally showed that the first phase to be consumed at the onset of melting changes from garnet to CPX at pressures above 4.2 GPa. Thus, garnet stability increases dramatically with pressure, being more stable than OPX above 6.6 GPa. High degrees of partial melting at low pressure (<3 GPa) would result in high modal CPX abundances at the expense of garnet. The Sarfartoq garnet harzburgites have only traces of CPX (<1%), suggesting that

partial melting reached the point of CPX exhaustion at pressures higher than 4.2 GPa. Experimental evidence indicates that CPX is exhausted after 30% partial melting at 4.2 GPa, and after 45% partial melting at 7 GPa (Walter, 1998). This indicates that the garnet harzburgites are residues from similar degrees of partial melting, i.e. from 30 to 45%. Recent experimental work by Walter (1999) showed that polybaric, near fractional melting, may also explain some of the elemental trends observed in Siberia, South Africa and Tanzania. We plot the compositions of Sarfartoq garnet-free peridotites, garnet harzburgites and garnet lherzolites in figure 13, using both the batch and fractional melt-extraction models of Walter (1998; 1999). The averages for the Kaapvaal (K), Siberian (S) and Tanzanian (S) peridotites are also plotted for comparison. The Sarfartoq peridotites have low SiO_2 contents and thus plot well below the polybaric near fractional melting residues of pyrolite in fig. 13a, but may indicate over 60% of isobaric batch melting at pressures of about 3-4 GPa. The degrees of melting inferred from the silica content are thus believed to be unrealistic, as they cannot be reconciled with the average olivine compositions (Mg#) of the suite. This may indicate that protolith models, with respect to silica contents, are inadequate for the Sarfartoq area. In addition, the FeO contents of the Sarfartoq peridotites are generally higher than those reported for Kaapvaal, Siberian and Tanzanian suites (fig. 13), suggesting lower pressure melt extraction. Using MgO and Al_2O_3 in figures 13b and 13c, the Sarfartoq peridotites can be modeled to be residues of a pyrolitic mantle after 30-45% of batch melting at pressure around 3 GPa. The garnet-free peridotites lie close to a polybaric near-fractional melting model, indicating 40% melt extraction at an average pressure of 3 GPa, while the garnet peridotites consistently show lower degrees of partial

melting. The greater degree of melting inferred for the garnet-free peridotites is consistent with their higher olivine abundance and Mg#, compared to garnet harzburgites.

The majority of high-temperature deformed peridotites from cratonic settings are less depleted in incompatible major elements than undeformed, low-temperature lithologies. The fertile nature of these high-temperatures peridotites have led authors to regard these rocks as asthenospheric material (Boyd, 1987) or, alternatively, subducted oceanic lithosphere accreted to the bottom of cratonic roots (Kesson and Ringwood, 1989). However, detailed studies of compositional heterogeneity within mineral phases of some high-temperature peridotites suggests that they were modified shortly prior to the magmatic episode having brought these rocks to surface (e.g. Smith and Boyd, 1987; Griffin et al., 1989; Shizimu, 1999). In addition, Re-Os systematic of South African and Siberian deformed peridotites indicate Archean depletion ages (Pearson et al., 1995), suggesting that these may be modified fragment of ancient lithosphere. In this respect, the use of their major element chemistry to constrain their petrogenesis can be problematical. Detailed microprobe analyses of the mineral phases of the Sarfartoq high-temperature lherzolites have revealed that these lithologies are consistently more fertile than overlying harzburgites and, as such, may not simply represent modified harzburgitic assemblages. Although the origin of the Sarfartoq high-temperature lithologies is unconstrained at present, models involving accretion of oceanic lithosphere (Kesson and Ringwood, 1989) or upwelling of asthenopsheric material (Chesley et al., 1999) can be envisaged.

1.5.4 Chemical structure of the NAC lithospheric mantle

The coarse garnet-bearing lithologies record last depths of equilibration ranging from approximately 70 to 180 km, while deformed lherzolites yield depths in excess of 200

km. As discussed previously, the mineral chemistry of the garnet-free peridotites suggests a genetic link with the garnet-bearing lithologies. This is also supported by the ubiquitous presence of chromite in the garnet-free harzburgites, which is stable to much higher pressure compared to the hercynic spinel typical of spinel facies peridotites. As such, the absence of garnet may not be solely controlled by pressure, but may reflect a more refractory bulk composition for the garnet-free suite. Figure 14 depicts the relationships between the last depth of equilibration and olivine Mg#, olivine abundance, and TiO_2 and CaO concentrations in garnet for seven coarse garnet harzburgites. In all cases, deeper assemblages are characterized by more fertile compositions compared to shallower lithologies, i.e. lower olivine Mg# and abundances, and higher CaO and TiO_2 contents of garnets. Moreover, when compared to the garnet harzburgites, the range of values observed in the garnet-free peridotites plot towards the refractory part of the arrays (Fig. 14a and 14b), which is consistent with derivation from depths close to that of the shallower assemblages (i.e. approximately 70 km). Like the Tanzanian lithosphere (Lee and Rudnick, 1999), the Sarfartoq garnet-free peridotites are generally more refractory (high olivine abundance and olivine Mg#) than associated garnet harzburgites. The increase in fertility observed within the garnet peridotites at Sarfartoq has also been documented in Tanzania (Lee and Rudnick, 1999). Using garnets derived from kimberlitic mineral concentrates, Gaul et al. (2000) have suggested that similar relationships are present within the Slave, Siberian and Kaapvaal lithospheres. The origin of this layering is unclear, but may be indicative of a downward decrease in the degree of partial melting. This feature is consistent with polybaric fractional melting models (e.g. Walter, 1999), as would be expected for adiabatic melting of a rising mantle plume (Lee and Rudnick, 1999).

Alternatively, the layering could be secondary and reflect a metasomatic modification of the lithosphere by pervasive melt infiltration from the asthenosphere (Gaul et al., 2000).

At Sarfartoq, the porphyroclastic garnet lherzolites are derived from depths in excess of 200 km, and thus represent the deepest assemblages sampled by the kimberlite. These rocks differ from shallower lithologies not only in their texture, but also in their modal mineralogy and mineral chemistry. CPX is common in all deformed garnet lherzolites, but rare (<1%) in coarse garnet harzburgites and only present in significant amounts in one garnet-free peridotite (SAF-39; 12%). Moreover, garnet, OPX and olivine from deformed lherzolites are much more fertile compared to the shallower assemblages (e.g. lower Mg#, higher CaO and TiO_2 in garnets). This suggests that the lithospheric mantle underneath the Sarfartoq area is compositionally layered as follows: (1) an internally stratified upper layer (70 to 180 km) consisting of coarse, un-deformed, refractory garnet-bearing and garnet-free peridotites and, (2) a lower layer (180 to 225 km) characterized by fertile, CPX-bearing, porphyroclastic garnet lherzolites (fig. 15). A similar layered structure, i.e. refractory assemblages underlain by fertile lithologies, has been recognized within the Slave cratonic mantle (Griffin et al., 1999; Kopylova and Russel, 2000). Re-Os systematics of mantle peridotites from Tanzania (Chesley et al., 1999) and East Greenland (Hanghøj et al., 2000) indicate an increase of the $^{187}Os/^{188}Os$ ratio with depth, which is also positively correlated with indexes of fertility. Although this observation is consistent with progressive re-fertilization of the lithospheric mantle by asthenospheric melts, Chesley et al. (1999) also suggested that the lowermost, fertile, portion of the Tanzanian lithosphere may represent a younger addition (<1 Ga) to the overlying refractory ~2.8 Ga mantle. Multistage growth of the cratonic mantle beneath the

Canadian Artic has also been proposed based on combined Sr-Nd-Pb isotope systematics (Schmidberger et al., 2001). Although temporal constraints are presently not available, the sharp nature of the stratification observed for the Sarfartoq mantle may indicate a two-step process for the formation of this lithosphere. The distinct zoning patterns present in garnets from the deformed peridotites also support a different petrogenetic history for the fertile, high-temperature peridotites. Thus, the refractory garnet-free and garnet-bearing peridotites may constitute the Archean portion of the lithospheric root stabilized by high degrees of partial melting. The deeper, more fertile assemblages may represent a younger addition to the refractory overlying mantle.

1.6 CONCLUSIONS

The main conclusions of this study can be summarized as follows:

(1) The Sarfartoq peridotites can be separated in four groups: (1) CPX-free garnet harzburgite, (2) garnet-free peridotites, (3) fertile CPX-rich, deformed lherzolites and (4) ilmenite bearing dunites.

(2) Modal analyses showed that unlike the Kaapvaal and Siberian peridotites, the Sarfartoq suite is not typified by OPX enrichment, and is thus compositionally closer to the Wiedeman Fjord spinel harzburgites, the Somerset Island garnet peridotites and the Tanzanian peridotites.

(3) Ilmenite-free, underformed peridotites show similar degrees of depletion (whole-rock and olivine Mg#) as other cratonic suites, and are modeled as being residues after 30-45% of batch melting at pressures around 4 GPa, while the ilmenite-bearing dunites are interpreted as cumulates.

(4) Modeling of the P-T data indicates a relatively elevated surface (47.5 –50 mW/m^2) geotherm but cool (12 mW/m^2) mantle heat flow for the Sarfartoq area at the time of kimberlite magmatism. The model supports a lithosphere thickness of 220-225 km.

(5) The lithospheric mantle underneath the Sarfartoq area is compositionally layered as follows: (1) an internally stratified upper layer (70 to 180 km) consisting of coarse, un-deformed, refractory garnet-bearing and garnet-free peridotites and, (2) a lower layer (180 to 225 km) characterized by fertile, CPX-bearing, porphyroclastic garnet lherzolites. The stratification observed in the upper refractory harzburgite layer (70-180 km) is reflected by an increase in fertility (e.g. lower olivine abundance and fosterite content) with depth.

ACKNOWLEDGEMENTS

Dia Met Minerals Inc. and De Beers Exploration Canada are acknowledged for providing samples for this study as well as permission to publish and partial financial support. MB acknowledges FCAR (Fonds pour la Formation de Chercheurs et l'Aide a la Recherche) *Bourse de Recherche en Milieu Pratique* program for a doctorate scholarship. RKS acknowledges NSERC and FCAR for funding. J.-C. Mareschal (GEOTOP) is acknowledged for numerous discussions on mantle heat flows. Constructive reviews by Roberta Rudnick and Stephan Berstein improved the quality of this contribution.

REFERENCES

Arai, S. (1994). Characterization of spinel peridotites by olivine-spinel compositional relationships: Review and interpretations. *Chemical Geology* **113**: 191-204.

Bernstein, S., Kelemen, P.B. and Brooks, C.K. (1998). Depleted spinel harzburgite xenoliths in tertiary dykes from East Greenland: Restites from high degree melting. *Earth and Planetary Science Letters* **154**: 221-235.

Bizzarro, M, Stevenson, R. K and Boucher, D.R. (1999). Mantle xenoliths from southwestern Greenland: implications for the evolution and composition of the lithosphere under the North Atlantic craton. *GAC-MAC Joint Annual Meeting* **24**: 11.

Blichert-Toft, J. and Albarède , F. (1997). The Lu-Hf isotope geochemistry of chondrites and the evolution of the mantle-crust system. *Earth and Planetary Science Letters* **148**: 243-258.

Boyd, F.R. (1989). Compositional distinction between oceanic and cratonic lithosphere. *Earth and Planetary Science Letters* **96**: 15-26.

Boyd, F.R. and Mertzman, S.A. (1987). Composition and structure of the Kaapvaal lithosphere, southern Africa. *In: Mysen, B.O. (ed) Magmatic processes: physicochemical principles (Geochemical Society Special publication 1). Geochemical Society, Penn State University*, pp. 13-24.

Boyd, F.R. and Canil, D. (1997). Peridotite xenoliths from the Slave craton, Norwest Territories (abstract). (LPI contribution No. 921). *Seventh annual V.M. Goldschmidt Conference, Lunar and Planetary Institute, Houston*, pp. 34-35.

Boyd, F.R., Pokhilenko, N.P., Pearson, D.G., Mertzman, S.A., Sobolev, N.V., Finger, L.W. (1997). Composition of the Siberian cratonic mantle: evidence from Udachnaya peridotite xenoliths. *Contributions to Mineralogy and Petrology* **182**: 228-246.

Bowring, S.A., Housh, T. (1995). The Earth's early evolution. *Science* **269**: 1535-1540.

Brey, G.P., Köhler, T. (1990). Geothermobarometry in Four-phase Lherzolites II. New Thermobarometers and Practical Assessment of Existing Thermobarometers. *Journal of Petrology* **31**: 1353-1378.

Brunet, J. (1974). Concessions granted to Charter Consolidated Limited in the areas of Holsteinborg and Frederickshåb in Western Greenland. Report on exploration. Charter Consolidated Ltd. Internal report, 12 pp.

Brunet, J. (1976). Report on the investigation of the Holsteinborg concession, Western Greenland. Charter Consolidated Ltd., internal report, 12 pp.

Canil, D. (1991). Experimental evidence for the exsolution of cratonic peridotite from high-temperature harzburgite. *Earth and Planetary Science Letters* **106**: 64-72.

Chesley, J. T., Rudnick, R. L. and Lee, C.-T. (1999). Re-Os systematic of mantle xenoliths from the East African rift; Age, structure and history of the Tanzanian craton. *Geochimica et Cosmochimica Acta* **63**: 1203-1217.

Crank, J. (1975). The mathematics of diffusion, Oxford Univresity Press, 414 pp.

Fowler, C. M. R. (1990). The solid earth: an introduction to global geophysics, Cambridge University Press, 472 pp.

Gangully, J., Cheng, W and Chakraborty, S. (1998). Cation diffusion determination in aluminosilicate garnets: experimental determination in pyrope-almandine diffusion couples. *Contributions to Mineralogy and Petrology* **131**: 171-180.

Gaul , O. F., Griffin, W. L., O'Reilly , S. Y. and Pearson N. J. (2000). Mapping olivine composition in the lithospheric mantle. *Earth and Planetary Science Letters* **182**: 223-235

Griffin, W. L., Smith, D., Boyd, F. R., Cousens, D. R., Ryan, C. G., Sie, S. H. and Suter, G. F. (1989). Trace elements zoning in garnets from sheared mantle xenoliths. *Geochimica et Cosmochimica Acta* **53**: 561-567.

Griffin, W. L., O'Reilly, S. Y., Ryan, C. G., Gaul, O., Ionov, D. A. (1998). Secular Variation in the Composition of Subcontinental Lithospheric Mantle: Geophysical and

Geodynamic Implications. In Braun, J., Dooley, J., Goleby, B., van des Hilst, R. and Klootwijk, C. (eds) *Structure and Evolution of the Australian Continent, AGU Special Monograph*: 1-26

Griffin, W.L., Doyle, B.D., Ryan, C.G., Pearson, N.J., O'Reilly, S.Y., Davies, R., Kivi, K., Van Achterbergh, E and Natapov, L.M. (1999). Layered mantle lithosphere in the Lac de Gras Area, Slave Craton: composition, Structure and origin. *Journal of Petrology* **40**: 705-727.

Griffin, W.L., Pearson, N.J., Belousova, E., Jackson, S.E., van Achterbergh, E., O'Reilly, S.Y. and Shee, S.R. 2000. The Hf isotope composition of cratonic mantle: LAM-MC-ICPMS analysis of zircon megacrysts in kimberlites. *Geochimica et Cosmochimica Acta* **64**: 133-147.

Gurney J. J., Zweistra P. (1995). The interpretation of the major element compositions of mantle minerals in diamond exploration. *Journal of Geochemical Exploration* **53**: 293-309.

Hanghøj, K., Kelemen, P., Berstein, S., Blusztajn, J., Frei, R. (2000). Osmium isotopes in the Wiedemann fjord mantle xenoliths: A unique record of cratonic mantle formation by melt depletion in the Archaean. *Geochemistry, Geocphysics, Geosystems* **2**, paper number 20000GC000085.

Harte, B. (1977). Rock nomenclature with particular relation to deformation and recrystallisation textures in olivine-bearing xenoliths. *Journal of Geology* **85**: 279-288.

Herzberg, C.T. (1993). Lithosphere peridotites of the Kaapvaal craton. *Earth and Planetary Science Letters* **120**: 13-29.

Herzberg, C., Feigenson, M., Skuba, C. And Ohtani, E. (1988). Majorite fractionnation recorded in the geochemistry of peridotites from South Africa. *Nature* **332**: 823-826.

Irvine, T. N. (1965). Chromian spinel as a petrogenetic indicator. Part 1 Theory. *Canadian Journal of Earth Sciences* **2**: 648-672.

Jaupart, C. and Mareschal, J.C. (1999). The thermal structure and thickness of continental roots. *Lithos* **48**: 93-114.

Jordan, T. H. (1973). The continental tectosphere. *Rev. Geophys. Space Phys.* **13**:1-12.

Kalsbeek, F., Pidgeon, R.T. and Taylor, P.N. (1987). Nagssugtoqidian mobile belt of West Greenland: a cryptic 1850 Ma suture between two Archaean continents - chemical and isotopic evidence. *Earth and Planetary Science Letters* **85**: 385-385.

Kalsbeek, F. and Nutman, A. P. (1996). Anatomy of the Early Proterozoic Nagssugtoqidian Orogen, West Greenland, explored by reconnaissance SHRIMP U-Pb dating. *Geology* **24**: 515-518.

Kelemen, P. B., Dick, H. J. And Quick, J. E. (1992). Formation of harzburgite by pervasive melt/rock reaction in the upper mantle. *Nature* **358**: 635-641.

Kelemen, P.B., Hart, S.R. and Bernstein, S. (1998). Silica enrichment in the continental upper mantle via melt/rock reaction. *Earth and Planetary Science Letters* **164**: 387-406.

Kesson, S. E. and Ringwood, A. E. (1989). Slab-melt interaction 2. The formation of diamonds. *Chemical Geology* **78**: 97-118.

Kopylova, M.G., Russell, J.K. and Cookenboo, H. (1999). Petrology of peridotite and pyroxenite xenoliths from the Jericho Kimberlite: Implications for the thermal state of the mantle beneath the Slave Craton, Northern Canada. *Journal of Petrology* **40**: 79-104.

Kopylova, M. G. and Russell, J. K. (2000). Chemical stratification of cratonic lithosphere: constraints from the Northern Slave craton, Canada. *Earth and Planetary Science Letters* **181**: 71-87.

Larsen, L.M., Rex, D.C. and Secher, K. (1983). The age of carbonatites, kimberlites and lamprophyres from southern West Greenland: recurrent alkaline magmatism during 2500 million years. *Lithos* **16**: 215-221.

Larsen, L.M. and Rex, D.C. (1992). A review of the 2500 Ma span of alkaline-ultramafic, potassic and carbonatitic magmatism in West Greenland. *Lithos* **28**: 367-402.

Lee, C.-T. and Rudnick, R.L. (1999) Compositionally stratified cratonic lithosphere: petrology and geochemistry of peridotite xenoliths from the Labait tuff cone, Tanzania, In (Gurney, J.J., Gruney, J.L., Pascoe, M.D. and Richardson, S.H., eds.) *The Nixon Volume, Proc. Seventh Int. Kimberlite Conf.* pp. 503-521.

MacKenzie. J.M., Canil, D. (1999). Composition and thermal evolution of cratonic mantle beneath the central Archean Slave Province, NWT, Canada. *Contributions to Mineralogy and Petrology* **134**: 313-324.

McDonough, W.F. (1990). Constraints on the composition of the continental lithospheric mantle. *Earth and Planetary Science Letters* **101**: 1-18.

McDonough, W.F., Sun, S.-S. (1995). The composition of the Earth. *Chemical Geology* **120**: 223-253.

Minex, (1998). West Greenland diamond review and update. *Greenland Minex news* **14**: 4-5.

Mitchell R. H. (1986). Kimberlites: Mineralogy, Geochemistry and Petrology. *Plenum Press, New York*, 442 pp.

Mitchell, R. H. (1995). Kimberlites, orangeites, and related rocks, *Plenun Press, New York*, 410 pp.

Mitchell, R. H., Scott Smith and Larsen, L. M. (1999). Mineralogy of ultramafic dikes from the Sarfartoq, Sisimiut and Maniitsoq Areas, West Greenland. *Proceedings of the 7th International Kimberlite Conference, Cape Town, South Africa* (Capetown, South Africa: National Book Printers), Dawson Volume: 574-583.

Pearson, D.G., Shirey, S.B., Carlson, R.W., Boyd, F.R., Pokhilenko, N.P.and Shimizu, N. (1995). Stabilisation of Archaean lithospheric mantle: A Re-Os isotope study of peridotite xenoliths from the Kaapvaal craton. *Earth and Planetary Science Letters* **134**: 341-357.

Pearson, D.G. (1999). The age of continental roots. *Lithos* **48**: 171-194.

Pollack, H. N. and Chapman, D. S. (1977). On the regional variation of heat flow, geotherms, and the thickness of the lithosphere. *Tectonophysics* **38**: 279-296.

Rosing M. T., Nutman A. P., Løfqvist L. (2001). A new fragment of the early earth crust: the Aasivik terrane of West Greenland, *Precambrian Research* **105:** 115-128

Rudnick, R. L., McDonough, W. F. And Orpin, A. (1994). Northern Tanzanian peridotite xenoliths: a comparison with Kaapvaal peridotites and inferences on metasomatic interactions. In: Meyer, H. O. and Leonardos, O. H. (eds) *Kimberltites, Related Rocks and Mantle Xenoliths: Proceedings 5th International Kimberlite Conference, Vol., 1.* Rio de Janeiro: CPRM: 336-354.

Rudnick, R.L. and Nyblade, A.A. (1999). The thickness and haet production of Archean lithosphere: Constraints from xenolith thermobarometry and surface heat flows. In: Fei, Y., Bertka, M. and Mysen, B.O. (eds) *Mantle Petrology: Field observations and High*

Pressure experimentation: A tribute to Francis R. Boyd. The Geochemical Society Special Publication 6: 3-12.

Schmidberger, S.S. and Francis D. (1999). Nature of mantle roots beneath the North America craton: mantle xenolith evidence from Somerset Island kimberlites. *Lithos* **48**: 195-216.

Schmidberger, S. S. Simonetti , A. and Francis, D. (2001). Sr-Nd-Pb isotope systematics of mantle xenoliths from Somerset Island kimberlites. *Geochimica et Cosmochimica Acta* **65**: 4243-4255.

Shimizu, N. (1999). Young geochemical features in cratonic peridotites from Southern Africa and Siberia. In: Fei, Y., Bertka, M. and Mysen, B.O. (eds) *Mantle Petrology: Field observations and High Pressure experimentation: A tribute to Francis R. Boyd. The Geochemical Society Special Publication 6:* 47-55.

Sun, S.-s. and McDonough, W. F. (1989). Chemical and isotopic systematics of oceanic basalts: implications for mantle composition and processes. In: Saunders, A. D. and Norry, M. J. (eds) *Magmatism in the Ocean Basins. Geological Society, London, Special Publicaton* **42**: 313-345.

Walter M.J. (1998). Melting of garnet peridotite and the origin of komatiite and depleted lithosphere. *Journal of Petrology* **39**: 29-60.

Walter, M. J. (1999). Melting residues of fertile peridotites and the origin of cratonic lithosphere. In: Fei, Y., Bertka, M. and Mysen, B.O. (eds) *Mantle Petrology: Field observations and High Pressure experimentation: A tribute to Francis R. Boyd. The Geochemical Society Special Publication 6:* 225-239.

Wallace, M. and Green, D. H. (1988). An experimental determination of primary carbonatite composition. *Nature* **335**: 343-345.

Xue, X., Baadsgaard, H., Irving, A. J. and Scarfe, C. M. (1990). Geochemical and isotopic characteristics of lithospheric mantle beneath West Kettle River, British Columbia: Evidence from ultramafic xenoliths. *Journal of Geophysical Research* **95**: 15879-15891.

Yaxley, G. M., Green, D. H. and Kamenetsky, V. (1998). Carbonatite metasomatism in the Southeastern Australian lithosphere. *Journal of Petrology* **39**: 1917-1930.

Zhao, D., Essene, E. J., Zhang, Y., Hall, C. M. and Wang, L. (1997). Newly discovered kimberlites and mantle xenoliths from Somerset Island and Brodeur Peninsula, Canada: Pressure, temperature, oxygen fugacity and volatile content and age. *NWT Geology Division, Department of Indian and Northern Affairs, Yellowknife*, pp. 1-105.

Table 1: Whole-rock major and trace element data

Sample	1	4	6	8	38	40	2	3	302	303	304	7	26	27
Lithology	GH	GH	GH	GH	GH	GH	GL	GL	GL	GL	GL	ID	ID	ID
Major elements (wt. %)														
SiO_2	41.38	40.06	40.42	42.00	41.78	41.85	34.00	42.50	35.59	38.79	38.92	40.21	38.62	40.56
TiO_2	0.12	0.38	0.09	0.12	0.18	0.16	1.38	0.29	0.08	0.13	0.11	0.84	0.09	0.47
Al_2O_3	1.16	1.16	0.59	0.86	1.86	1.97	2.03	2.58	0.17	0.52	0.73	0.86	0.09	1.14
FeO	6.96	8.75	7.24	7.89	8.29	8.40	9.83	7.99	10.38	7.32	7.08	12.55	12.83	11.36
MnO	0.11	0.14	0.11	0.12	0.13	0.14	0.16	0.14	0.08	0.10	0.11	0.17	0.17	0.19
MgO	48.00	44.02	47.88	46.34	44.21	44.40	35.54	40.89	39.68	43.51	43.30	41.50	45.00	36.99
CaO	0.54	1.56	0.60	0.75	1.09	1.08	7.62	3.61	1.35	0.62	0.63	0.68	0.72	4.73
Na_2O	0.21	0.21	0.08	0.19	0.20	0.20	0.72	0.34	0.07	0.21	0.09	0.23	0.17	0.33
K_2O	0.24	0.32	0.18	0.18	0.25	0.22	0.40	0.20	0.05	0.05	0.02	0.70	0.06	0.98
P_2O_5	0.03	0.07	0.03	0.03	0.04	0.04	0.06	0.07	0.03	0.03	0.01	0.04	0.04	0.06
LOI	0.78	2.80	1.60	1.03	1.04	0.92	7.16	1.28	11.62	8.06	7.94	0.76	0.80	1.64
Total	99.52	99.46	98.83	99.51	99.07	99.37	98.89	99.88	99.11	99.32	98.94	98.54	98.59	98.44
Mg #	0.92	0.90	0.92	0.91	0.90	0.90	0.87	0.90	0.87	0.91	0.92	0.85	0.86	0.85
Trace elements (ppm)														
Ga	1	1.7	1.4	0	1.2	1.6	4.4	3	0	0	1.2	2.8	1	4.6
Nb	4.6	25.7	6.1	4.3	6.2	4.4	97.4	7.9	2.3	5.5	2.5	10.7	8.1	16.3
Rb	9.8	13.9	7.9	7.5	9.9	9.2	38.7	8.1	1.8	2.7	1.4	36.4	3.6	55.1
Sr	53.3	168.6	51.5	44.7	74.6	65.8	712.8	123.5	66	40.1	12.6	76.9	58.6	133.8
Zr	6.1	22.9	12.9	8.2	13.5	15.1	117.3	24.3	5.9	6.6	3.1	9.3	13.8	21
Ba	56.0	146.2	36.6	38.1	77.8	52.9	2439.9	66.1	17.9	21.8		92.6	43.6	96.4
Cr	1824	1690	1728	1554	2947	3097	1552	4566	320	1539	2094	3657	359	2604
Ni	2487	2185	2574	2435	2260	2249	2269	2061	2008	2296	2267	1728	2342	1497

Table 1 (continued)

Sample	28	29	36	9	11	12	13	14	32	37	39	41	42
Lithology	ID	ID	ID	GFP	GFP	GFP	GFP	GFP	GFP	GFP	GFP	GFP	GFP
Major elements (wt. %)													
SiO_2	48.37	38.25	38.10	40.24	39.99	39.30	40.27	39.48	40.39	41.16	41.06	42.00	40.02
TiO_2	0.25	0.27	0.23	0.19	0.08	0.09	0.16	0.09	0.04	0.07	0.16	0.04	0.13
Al_2O_3	0.59	0.31	0.12	0.21	0.19	0.06	0.44	0.22	0.11	0.17	0.44	0.18	0.27
FeO	8.82	13.32	13.02	7.40	6.94	9.58	7.76	8.46	7.06	8.00	6.70	7.06	7.75
MnO	0.16	0.18	0.19	0.12	0.10	0.13	0.12	0.15	0.10	0.11	0.11	0.11	0.12
MgO	38.73	44.02	44.19	47.69	49.64	48.01	45.67	46.78	50.26	48.25	47.02	48.51	48.89
CaO	0.81	0.73	0.98	1.15	0.53	0.80	1.79	1.24	0.32	0.53	1.05	0.34	0.89
Na_2O	0.15	0.11	0.09	0.17	0.09	0.10	0.26	0.18	0.09	0.23	0.27	0.14	0.14
K_2O	0.10	0.20	0.10	0.22	0.12	0.04	0.25	0.16	0.04	0.11	0.37	0.08	0.12
P_2O_5	0.03	0.04	0.04	0.06	0.03	0.04	0.07	0.05	0.03	0.03	0.04	0.02	0.04
LOI	0.71	0.84	1.64	2.00	1.52	1.05	2.31	1.59	0.37	0.81	1.78	0.56	1.32
Total	98.71	98.27	98.70	99.44	99.23	99.21	99.09	98.40	98.82	99.47	99.00	99.04	99.68
	0.89	0.85	0.86	0.92	0.93	0.90	0.91	0.91	0.93	0.91	0.93	0.92	0.92
Trace elements (ppm)													
Ga	2.6	1.3	1	1.1	0	1	1.7	1.4	0	1.1	1.4	0	1.1
Nb	4.4	7.8	6.3	9.1	4.8	5.8	6.6	7.4	4.6	2.8	6.5	6.2	9.1
Rb	5.2	12.5	4.1	9.2	5.8	2.7	12.1	5.9	2.1	5.3	16.5	4	6.2
Sr	39.5	105.3	122.1	83.1	102.1	65.8	96	87.7	40.4	82.2	106.8	34.6	83.6
Zr	4.6	11.9	14.8	14.4	10.4	8.7	19.2	14.4	5	7.8	12.3	5.2	8.9
Ba	32.7	38.1	19.4	53.7	19.4	38.9	38.9	24.1	13.2	34.2	45.9		57.6
Cr	3987	883	3346	1613	945	501	2391	2628	1756	1932	2467	2270	1165
Ni	1320	2047	2401	2551	2655	2648	2347	2346	2801	2591	2531	2757	2660

Table 2: Average microprobe analyses of xenolith constituent phases.

	SAF-01 (GH)			SAF-04 (GH)				SAF-06 (GH)				SAF-08 (GH)			SAF-38 (GH)			
	OL (5)	OPX (4)	GNT (4)	OL (2)	OPX (3)	OPX^R (2)	GNT (3)	OL (7)	OPX (3)	GNT (6)	SPI (3)	OL (4)	OPX (3)	GNT (5)	OL (7)	OPX (6)	GNT (4)	GNT^R (2)
Na_2O	0.01	0.07	0.02	0.01	0.16	0.16	0.06	0.00	0.08	0.02	0.00	0.01	0.11	0.06	0.01	0.16	0.07	0.07
MgO	51.75	37.33	22.66	49.69	36.29	35.68	20.78	50.94	36.71	20.99	12.19	50.50	40.97	20.74	49.89	35.94	20.40	20.48
TiO_2	0.00	0.01	0.00	0.02	0.13	0.20	0.35	0.00	0.01	0.00	0.12	0.02	0.07	0.34	0.03	0.11	0.38	0.40
K_2O	0.00	0.01	0.00	0.02	0.02	0.01	0.00	0.00	0.01	0.00	0.00	0.00	0.02	0.00	0.00	0.01	0.00	0.00
CaO	0.01	0.10	1.77	0.05	0.48	0.69	4.52	0.00	0.17	2.47	0.00	0.05	0.34	4.52	0.04	0.61	4.61	4.63
FeO	6.61	4.10	7.60	9.26	4.48	5.29	6.99	7.10	4.39	8.30	19.72	7.53	5.66	6.81	8.37	4.75	7.03	7.11
SiO_2	41.33	57.92	42.12	40.81	57.36	57.04	41.61	40.94	57.52	41.42	0.01	41.20	52.18	41.80	40.86	57.36	41.51	41.69
Al_2O_3	0.00	0.54	21.51	0.02	0.64	0.77	20.15	0.00	0.48	20.53	8.29	0.01	0.41	20.50	0.01	0.66	20.32	20.39
Cr_2O_3	0.01	0.20	3.58	0.01	0.25	0.18	4.79	0.01	0.19	5.03	58.42	0.02	0.17	4.25	0.02	0.25	4.44	4.30
MnO	0.07	0.09	0.41	0.12	0.12	0.11	0.35	0.09	0.11	0.49	0.29	0.10	0.10	0.32	0.10	0.11	0.33	0.33
NiO	0.39	0.09	0.00	0.36	0.10	0.11	0.01	0.38	0.09	0.01	0.09	0.37	0.20	0.01	0.38	0.11	0.01	0.01
Total	100.18	100.45	99.67	100.36	100.01	100.24	99.61	99.48	99.76	99.28	99.13	99.82	100.21	99.36	99.72	100.07	99.09	99.41
Mg#	0.933	0.942	0.842	0.905	0.935	0.923	0.841	0.927	0.937	0.818	0.524	0.923	0.928	0.844	0.914	0.931	0.838	0.837
Cr #											0.901							
%	88	6	6	84	11	-	-5	93	5	2	tr	78	18	4	78	13	9	-

	SAF-40 (GH)			SAF-02 (GL)					SAF-03 (GL)				SAF-304 (GL)				SAF-11 (SD)	
	OL (4)	OPX (4)	GNT (6)	OL (4)	OPX (4)	CPX (10)	GNT (8)	GNT^R (1)	OL (6)	OPX (3)	CPX (8)	GNT (4)	OL (3)	OPX (2)	CPX (3)	GNT (5)	OL (6)	SPI (2)
Na_2O	0.01	0.18	0.06	0.01	0.20	1.95	0.09	3.04	0.02	0.20	1.94	0.09	0.02	0.21	1.87	0.26	0.01	0.00
MgO	49.64	35.50	20.82	50.03	34.68	17.93	20.09	17.04	49.94	35.21	17.95	20.17	50.56	35.42	18.31	19.83	51.78	12.38
TiO_2	0.02	0.12	0.32	0.03	0.21	0.40	0.94	3.22	0.04	0.21	0.42	0.98	0.03	0.20	0.43	0.81	0.00	0.69
K_2O	0.00	0.02	0.00	0.00	0.01	0.04	0.00	0.00	0.00	0.01	0.04	0.00	0.00	0.01	0.04	0.00	0.00	0.08
CaO	0.03	0.50	4.51	0.05	0.80	17.68	4.99	9.78	0.05	0.78	17.66	5.04	0.05	0.80	17.49	5.23	0.02	0.01
FeO	8.94	5.22	7.07	8.81	5.54	3.29	7.94	4.86	8.67	5.30	3.19	7.80	7.91	4.81	2.87	7.31	6.11	20.16
SiO_2	40.99	57.32	41.59	40.87	56.48	54.24	41.18	42.42	40.75	56.12	53.87	41.29	40.73	55.91	54.12	38.17	41.41	0.00
Al_2O_3	0.03	0.61	19.81	0.03	0.70	2.06	19.21	14.13	0.02	0.68	2.05	19.33	0.01	0.67	1.92	18.86	0.00	6.62
Cr_2O_3	0.02	0.22	4.41	0.02	0.23	1.34	4.06	0.96	0.03	0.25	1.41	4.05	0.05	0.35	1.72	7.91	0.00	58.55
MnO	0.12	0.12	0.34	0.11	0.13	0.11	0.33	0.10	0.11	0.12	0.11	0.33	0.10	0.12	0.11	0.37	0.09	0.27
NiO	0.37	0.10	0.01	0.36	0.09	0.05	0.01	0.05	0.34	0.10	0.05	0.01	0.36	0.10	0.05	0.01	0.37	0.11
Total	100.16	99.91	98.95	100.32	99.06	99.08	98.84	95.59	96.59	98.99	98.68	99.09	99.82	98.60	98.91	98.75	99.79	98.87
Mg#	0.908	0.924	0.840	0.910	0.918	0.907	0.818	0.862	0.911	0.922	0.909	0.822	0.919	0.929	0.919	0.829	0.938	0.522
Cr #																		0.856
%	80	11	10	76	3	14	7	-	72	1	16	11	84	10	2	4	-	-

Table 2 (continued)

	SAF-13 (GFL)				SAF-14 (GFL)				SAF-39 (GFL)				SAF-41 (GFL)				SAF-12 (SD)	
	OL (3)	OPX (3)	CPX (3)	SPI (3)	OL (8)	OPX (2)	CPX (6)	SPI (5)	OL (5)	OPX (2)	CPX (1)	SPI (5)	OL (5)	OPX (8)	CPX (2)	SPI (2)	OL (3)	SPI (2)
Na_2O	0.01	0.12	2.33	0.00	0.01	0.11	0.94	0.00	0.01	0.11	2.95	0.00	0.01	0.07	2.85	0.00	0.01	0.00
MgO	50.73	34.74	15.78	14.27	50.79	34.93	18.19	10.83	51.68	37.14	15.55	11.90	50.61	36.65	15.15	12.00	50.71	13.09
TiO_2	0.03	0.10	0.17	3.37	0.00	0.11	0.23	1.31	0.01	0.04	0.20	1.59	0.00	0.00	0.00	0.15	0.02	2.87
K_2O	0.00	0.01	0.02	0.00	0.00	0.02	0.03	0.00	0.00	0.03	0.04	0.00	0.00	0.02	0.02	0.00	0.00	0.00
CaO	0.01	3.95	20.34	0.07	0.02	1.23	20.80	0.01	0.01	0.25	18.82	0.00	0.03	0.21	19.48	0.01	0.04	0.00
FeO	7.62	1.21	2.17	20.38	7.70	5.60	2.93	26.83	6.65	4.13	2.22	20.33	7.47	4.54	1.99	22.10	7.85	23.23
SiO_2	40.82	55.37	54.49	0.13	41.45	57.72	54.63	0.02	41.45	58.07	54.51	2.83	41.09	57.80	54.80	0.01	41.30	0.06
Al_2O_3	0.01	3.04	0.91	9.73	0.00	0.22	0.43	0.78	0.00	0.20	1.24	0.03	0.08	0.58	2.87	7.15	0.00	8.97
Cr_2O_3	0.01	1.27	3.47	50.36	0.01	0.26	0.97	57.70	0.00	0.20	4.09	61.95	0.02	0.23	2.37	56.82	0.01	50.43
MnO	0.12	0.10	0.08	0.32	0.13	0.13	0.09	0.32	0.10	0.12	0.09	0.38	0.11	0.12	0.08	0.31	0.12	0.30
NiO	0.37	0.12	0.04	0.19	0.34	0.09	0.05	0.14	0.39	0.10	0.04	0.13	0.39	0.08	0.03	0.11	0.35	0.19
Total	99.74	100.03	99.79	98.81	100.44	100.41	99.27	98.04	100.30	100.39	99.74	99.15	99.82	100.30	99.63	98.75	100.41	99.22
Mg#	0.922	0.981	0.928	0.555	0.922	0.917	0.917	0.418	0.933	0.941	0.926	0.511	0.923	0.935	0.931	0.492	0.920	0.501
Cr #				0.776				0.980				0.999				0.842		0.790
%	88	10	2	tr	95	4	tr	1	87	1	12	1	91	7	2	tr	-	-

	SAF-07 (ID)		SAF-26 (ID)			SAF-28 (ID)		SAF-29 (ID)			SAF-36 (ID)		SAF-37 (GFH)			S-10 (D)	SAF-42 (SD)	
	OL (5)	ILM (4)	OLV (5)	SPI (2)	ILM (3)	OPX (5)	SPI (8)	OLV (4)	SPI (2)	ILM (4)	OLV (4)	SPI (2)	OLV (7)	OPX (7)	SPI (7)	OLV (7)	OL (9)	SPI (2)
Na_2O	0.01	0.00	0.00	0.00	0.00	0.10	0.00	0.01	0.00	0.00	0.00	0.00	0.01	0.07	0.00	0.00	0.02	0.00
MgO	46.15	12.18	46.70	9.22	12.55	33.08	12.16	46.19	11.23	12.36	46.80	9.75	50.48	36.72	12.41	50.51	50.77	12.51
TiO_2	0.02	52.50	0.01	10.52	50.94	0.25	4.05	0.01	8.34	50.35	0.00	8.12	0.00	0.01	0.04	0.01	0.01	0.51
K_2O	0.00	0.00	0.00	0.00	0.00	0	0.00	0.00	0.00	0.00	0.00	0.00	0.00	0.02	0.00	0.00	0.00	0.00
CaO	0.03	0.07	0.01	0.35	0.04	0.90	0.08	0.04	0.01	0.06	0.01	0.00	0.02	0.22	0.00	0.03	0.04	0.01
FeO	13.37	30.19	12.77	53.47	32.76	7.04	24.22	13.28	32.85	29.92	12.84	42.77	7.63	4.35	17.16	7.80	7.28	21.41
SiO_2	40.26	0.09	39.78	0.00	0.03	56.39	0.05	40.19	0.00	0.18	40.11	0.00	41.22	57.76	0.04	41.11	41.10	0.00
Al_2O_3	0.01	0.38	0.00	3.71	0.21	1.06	6.96	0.00	6.78	0.68	0.00	2.51	0.01	0.35	8.69	0.07	0.02	6.15
Cr_2O_3	0.02	4.07	0.03	19.17	1.90	0.62	50.58	0.03	38.08	5.82	0.00	33.86	0.02	0.18	60.45	0.01	0.02	57.86
MnO	0.17	0.37	0.17	0.64	0.30	0.14	0.33	0.18	0.31	0.33	0.21	0.34	0.10	0.12	0.26	0.12	0.10	0.29
NiO	0.26	0.14	0.31	0.21	0.18	0.08	0.16	0.28	0.24	0.17	0.31	0.28	0.38	0.09	0.08	0.37	0.37	0.13
Total	100.31	100.02	99.78	97.39	98.92	99.65	98.63	100.22	97.91	99.90	100.28	97.69	99.86	99.90	99.23	100.02	99.72	98.87
Mg#	0.860	0.418	0.867	0.235	0.406	0.893	0.472	0.861	0.379	0.424	0.867	0.289	0.922	0.938	0.563	0.920	0.926	0.510
Cr #		0.878		0.776	0.856		0.830		0.790	0.852		0.901			0.824			0.863
%	-	-	-	-	-	-	-	-	-	-	-	-	93	6	1		-	-

All analyses are from mineral cores except where indicated (R=rim). Number of grains analyzed in parenthesis. GH=garnet harzburgite, GL=garnet lherzolite, GFL=garnet-free lherzolite, GFH=garnet-free harzburgite, ID=ilmenite dunite, D=dunite. Mg# = atomic (Mg/(Mg+Fe)), Cr # = atomic (Cr/(Cr+Al)). % represent the calculated modal abundance of each phase in the rock. **Table 3:** Last equilibration pressures and temperatures of Safartoq garnet peridotites.

Sample	Lithology	Temperature (C)	Pressure (GPa)
1	Garnet harzburgite	660	2.2
4	Garnet harzburgite	1012	4.3
6	Garnet harzburgite	738	2.3
8	Garnet harzburgite	1015	4.4
38	Garnet harzburgite	1087	4.7
40	Garnet harzburgite	1019	4.2
303	Garnet harzburgite	1213	5.5
2	Garnet lherzolite	1274	6.1
3	Garnet lherzolite	1278	6.3
304	Garnet lherzolite	1298	6.1

Temperature and pressure estimates of garnet bearing lherzolitic lithologies were calculated by combining the *two-pyroxene* thermometer and the *Al in OPX* barometer of Brey and Köhler (1990), while the P-T conditions of garnet facies harzburgites were computed by combining the *Ca in OPX* thermometer and the *Al in OPX* barometer of Brey and Köhler (1990).

Table 4: Modeled lower crustal temperatures, surface and mantle heat flows.

		Heat flows (mW/m^2)					
		0.6 $\mu W/m^3$		0.7 $\mu W/m^3$		0.8 $\mu W/m^3$	
Crustal thickness (km)	T_{base} of crust (C)	Surface	Mantle	Surface	Mantle	Surface	Mantle
40	546.3	46.1	22.1	48.1	20.1	50	18.1
45	575.1	45.5	18.5	47.7	16.2	50	14
50	603.7	45.2	15.2	47.7	12.7	50.2	10.2
55	632.1	45.2	12.2	48	9.5	50.7	6.7

Lower crustal temperatures extrapolated from the data set presented in table 4, using the following polynomial expression T= -0.0049D2 + 6.1889D + 306.5, where D=depth and T=temperature. Computed surface and heat flow values using three different crustal heat production parameters (0.6, 0.7, 0.8 $\mu W/m^3$) are presented for each crustal thickness model.

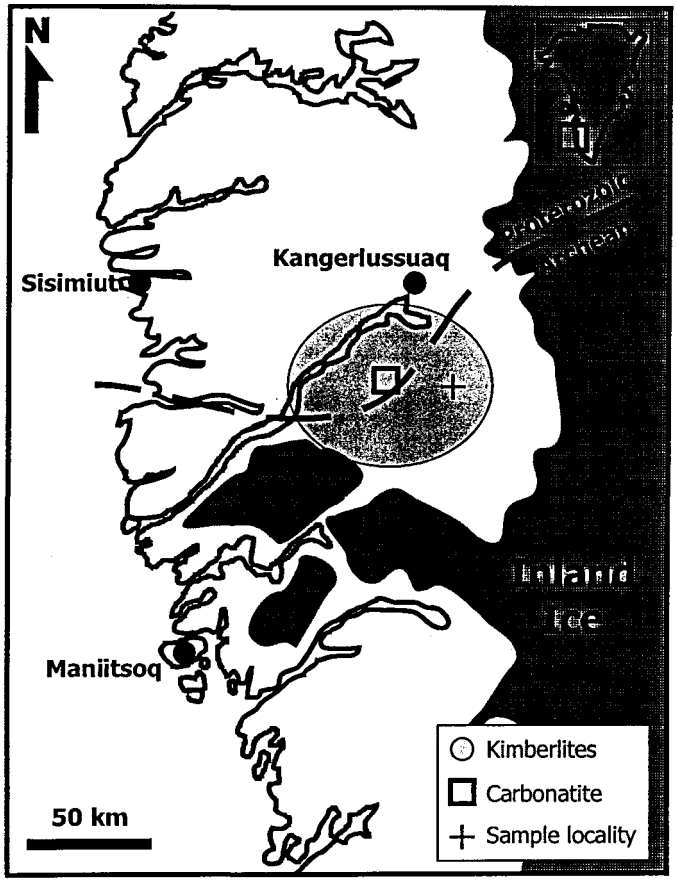

Figure 1: Map of the Sarfartoq alkaline complex, Southwestern Greenland, showing sampled xenolith locality. Area defined as kimberlites represents the approximate lateral extent of the kimberlite dike swarm.

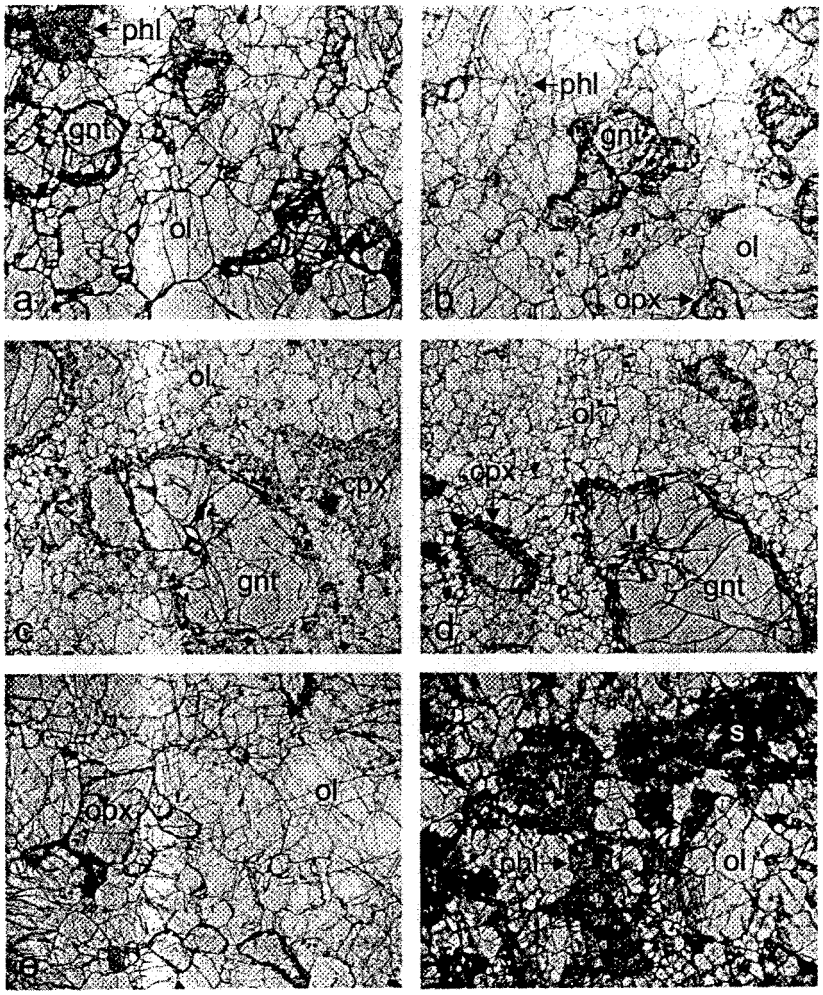

Figure 2: Microphotographs depicting the different textures of the Sarfartoq peridotites. (a) Sample SAF-40; coarse, low temperature garnet harzburgite, (b) Sample SAF-06; coarse, low temperature garnet harzburgite, (c) Sample SAF-02; porphyroclastic high-temperature lherzolite, (d) Sample SAF-02; porphyroclastic high-temperature lherzolite, (e) Sample SAF-41; coarse, garnet-free harzburgite, (f) Sample SAF-39, coarse, metasomatized garnet-free lherzolite. Field of view is approximately 10 mm. phl=phlogopite, ol=olivine, opx=orthopyroxene, cpx=clinopyroxene, gnt=garnet, s=spinel.

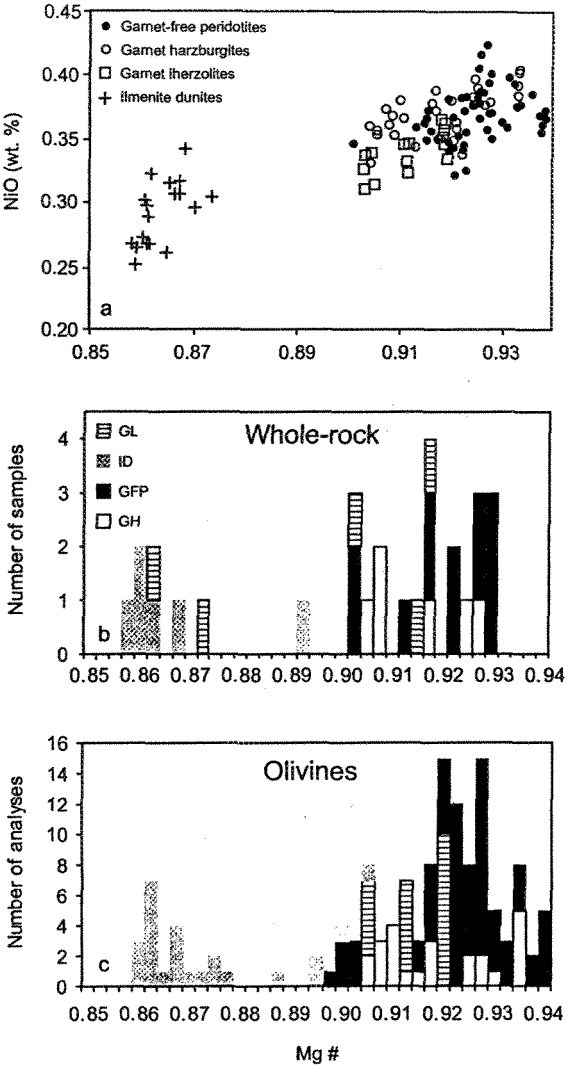

Figure 3: Variation of Mg# (atomic Mg/Mg + Fe) for the different rock types present at Sarfartoq. (a) Relationship between olivine Mg# and NiO (wt. %) abundance. Mg# = atomic (Mg/(Mg+Fe)). Also plotted for comparison are the Fe-rich dunites from Tanzania (Lee and Rudnick, 1999). (b) and (c) are frequency histograms showing the variation of the Mg# for whole-rock and olivine samples from Sarfartoq, respectively. GL=garnet lherzolites, GH=garnet harzburgites, GFP=garnet-free peridotites and ID=ilmenite dunites.

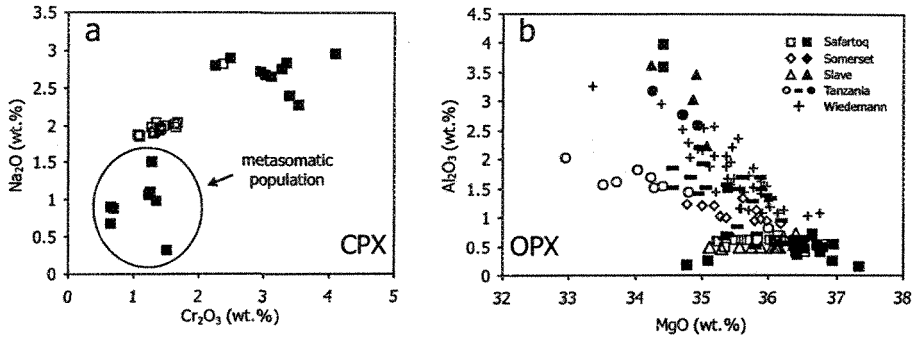

Figure 4: Plots of Al_2O_3 (wt.%) vs. MgO (wt.%) and Na_2O (wt.%) vs. Cr_2O_3 (wt.%) for Sarfartoq CPX (a) and OPX (b), respectively. Also plotted for comparison in (a) are OPX data from the following localities: Wiedemann spinel harburgites (Bernstein et al., 1998), Somerset Island spinel and garnet peridotites (Zhao et al., 1997; Schmidberger and Francis, 1999), Slave Craton spinel and garnet peridotites (Kopylova et al., 1998; McKenzie and Canil, 1999). Open symbols correspond to garnet facies peridotites. For the Sommerset, Slave and Tanzanian areas, solid symbols refer to spinel-facies peridotites. For Sarfartoq, solid symbols corresponds to garnet-free peridotites, while the horizontal solid line refers to the Tanzanian garnet-free peridotites. Wiedemann samples are all spinel facies harzburgites.

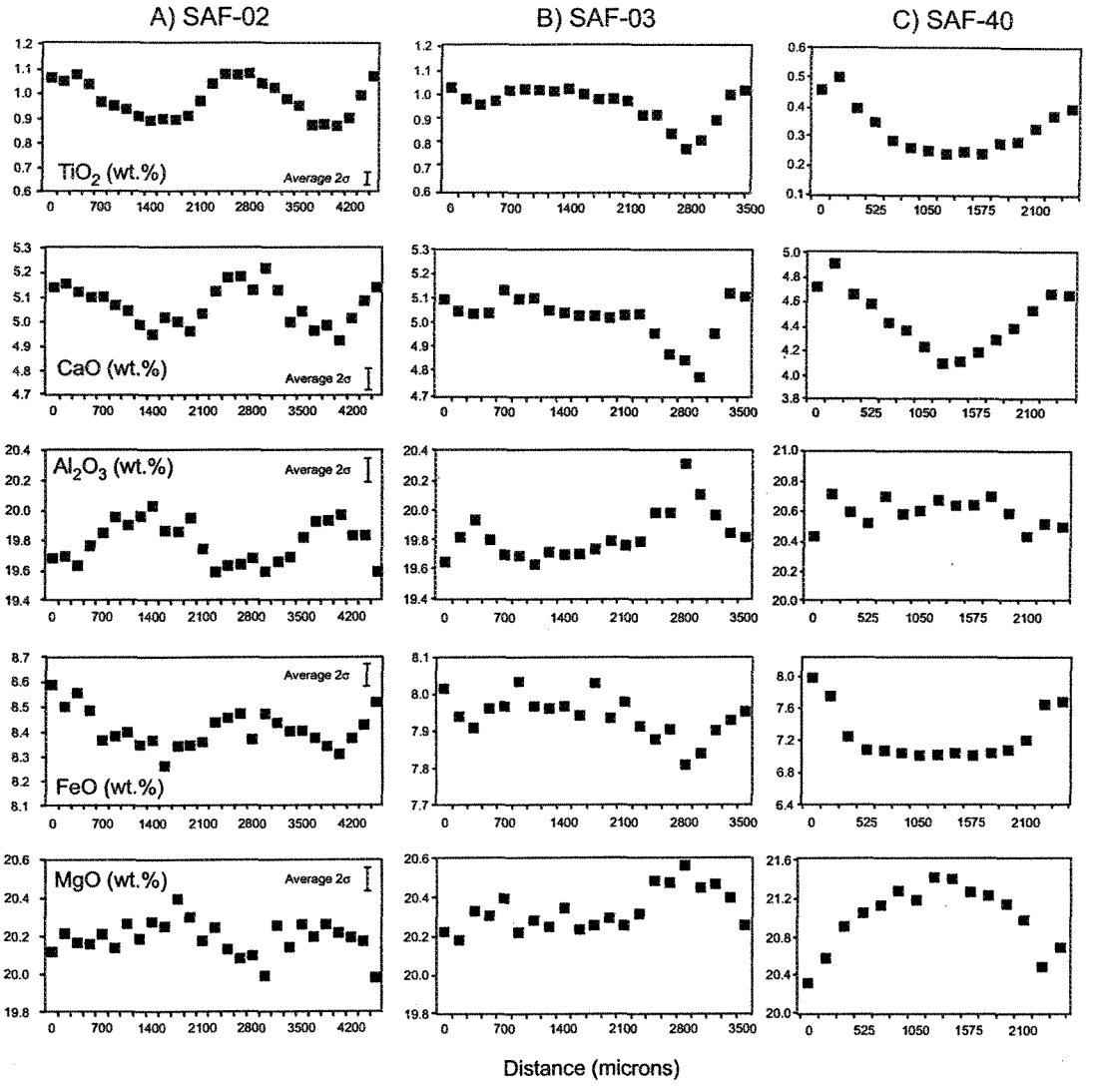

Figure 5: Electron microprobe data for selected oxides acquired at constant intervals along garnet grains (rim to rim). SAF-02 and SAF-03 are high-temperature garnet lherzolites, while SAF-40 is a coarse garnet harzburgite.

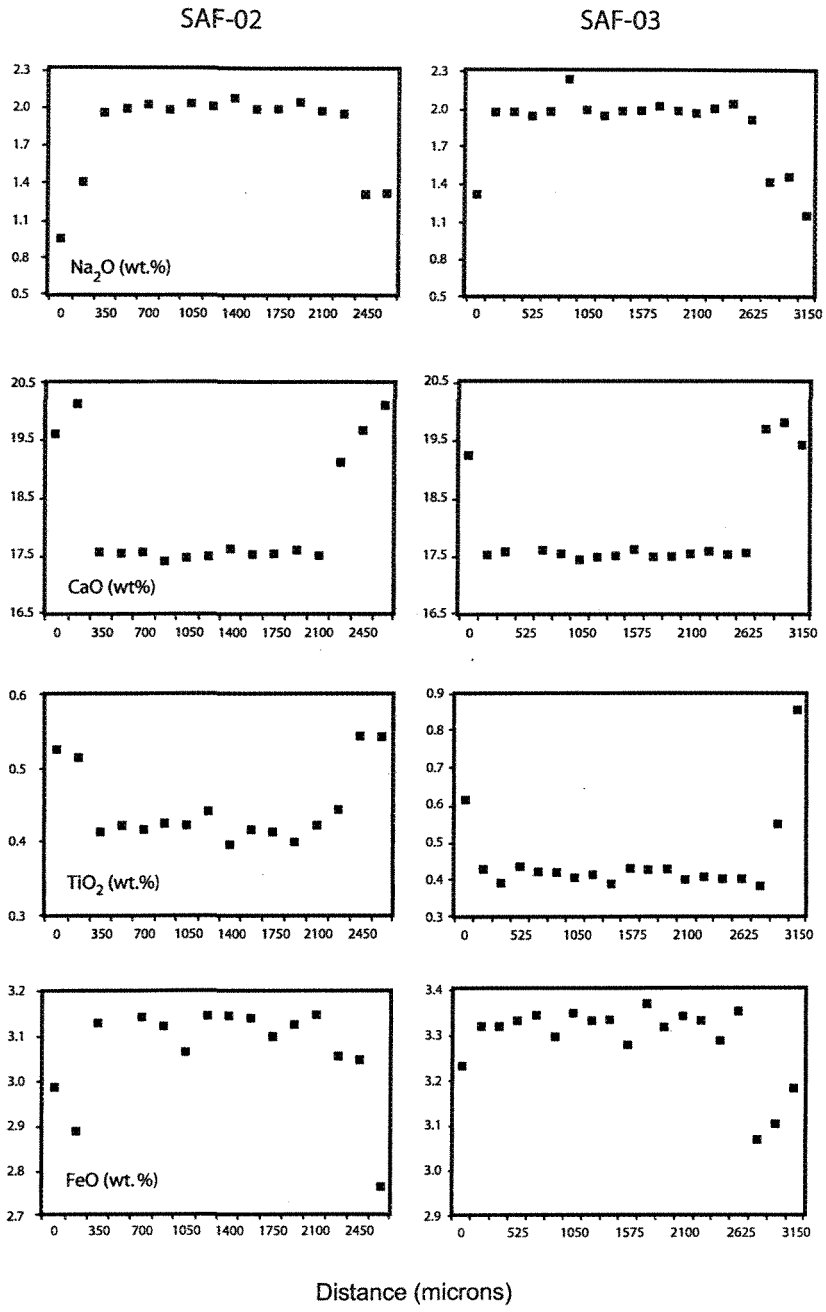

Figure 6: Electron microprobe data for selected oxides acquired at constant intervals along clinopyroxene grains (rim to rim). SAF-02 and SAF-03 are high-temperature garnet lherzolites. Analytical uncertainty is approximately 3% of quoted value (2σ level).

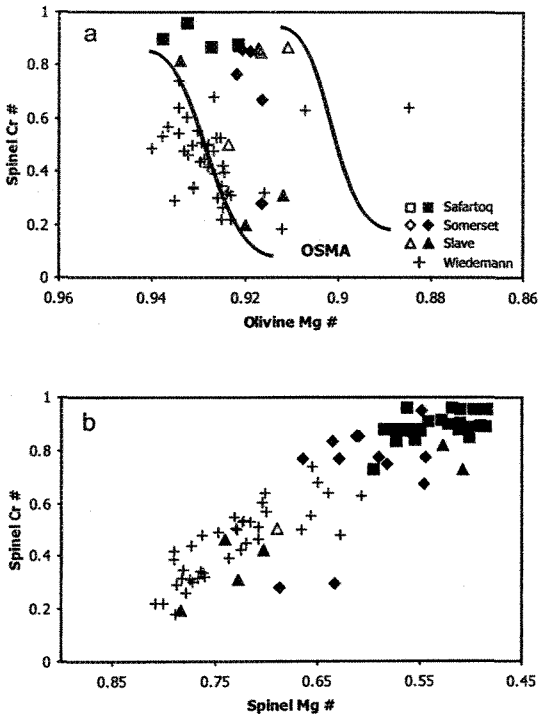

Figure 7: Plots of coexisting spinel Cr # vs. olivine Mg# (a) and Cr # vs. Mg# (b) for spinels from Sarfartoq and other localities. Mg# and Cr # are atomic (Mg/(Mg+Fe)) and (Cr/(Cr+Al)), respectively. Symbols and data sources as in Fig. 4. OSMA is the olivine-spinel mantle array of Arai (1994).

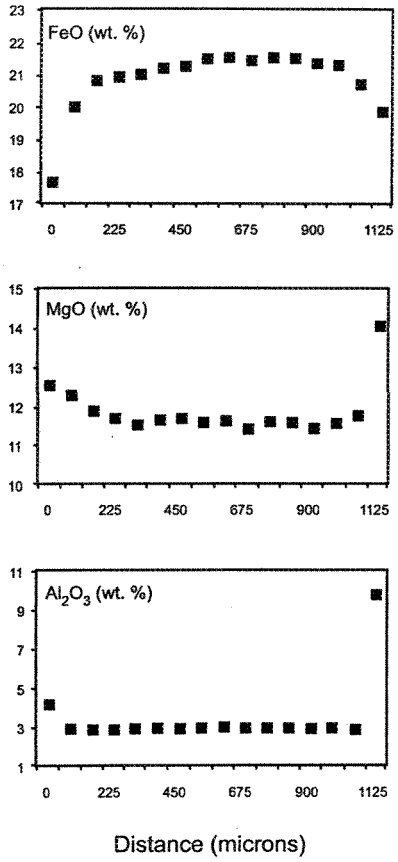

Figure 8: Electron microprobe data for selected oxides acquired at constant intervals along a spinel grain (rim to rim) from garnet-free lherzolite sample SAF-39.

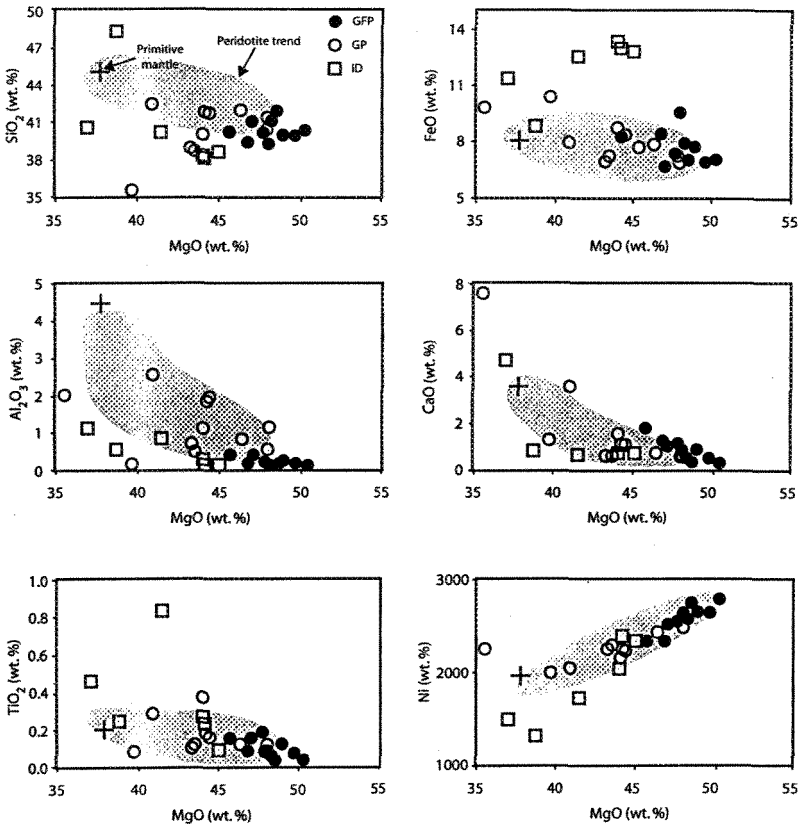

Figure 9: Selected major and trace element variations vs. MgO (wt.%) for peridotites from Sarfartoq. Peridotite trends constructed from data of McDonough (1990). Primitive mantle model is from McDonough and Sun (1995). GP=garnet peridotite, GFP=Garnet-free peridotite and ID=ilmenite dunite.

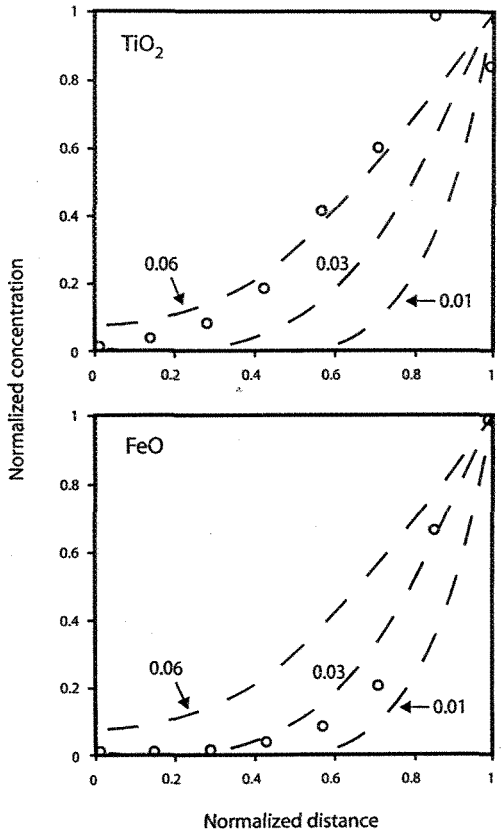

Figure 10: Ti (a) and Fe (b) zoning expressed in terms of normalized concentration and normalized distance. Normalized concentration = (concentration - concentration in core)/(concentration in rim - concentration in core); distances are normalized to the measured radius of the crystal. Dashed curves are for model diffusion gradients for different Dt/a^2 values, where D is the diffusion coefficient (m/s), a is the grain radius (m) and t is time (s). Note that the Fe and Ti zoning can be approximated with a model of diffusional penetration into a sphere of constant surface composition (Crank, 1975) with values of $Dt/a^2 = 0.06$ and 0.03, respectively.

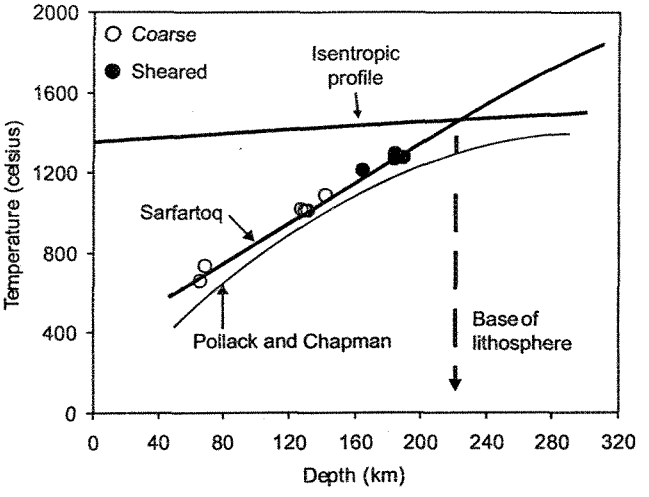

Figure 11: Depth vs temperature plot for the Sarfartoq peridotites, based on data presented in Table 3. Isentropic profile corresponds to a 1350°C potential temperature and a 0.5 °C/km gradient (Rudnick and Nylblade, 1999). The Sarfartoq mantle geotherm is based on a 45-km crust and a 0.8 $\mu W/m^3$ model of table 4. Also shown is the Pollack and Chapman (1977) conductive 40 mW/m2 geotherm. Pressures from table 3 were converted to depth using the following relation: 1 GPa = 33.3 km.

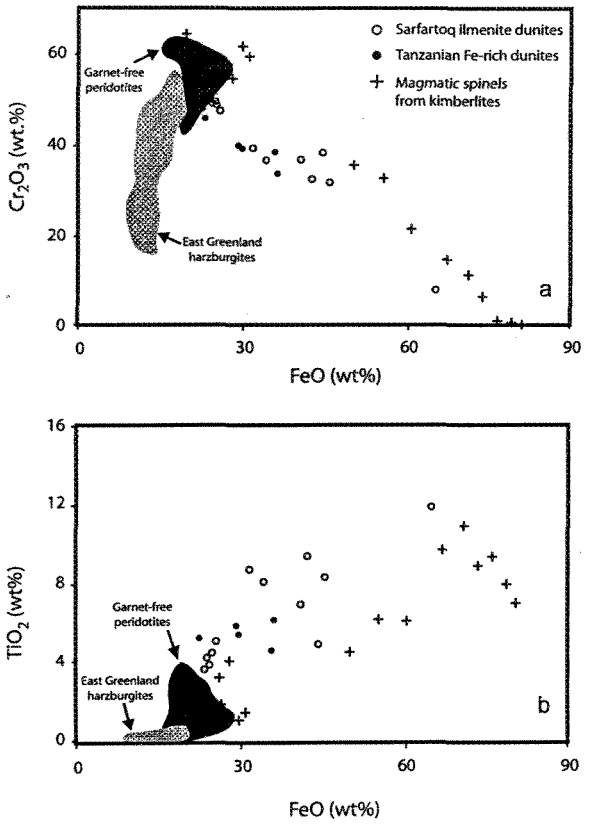

Figure 12: Diagrams showing variation of Cr_2O_3 (wt. %) (a) and TiO_2 (wt. %) (b) in realtion to FeO (wt. %) in spinels from Sarfartoq ilmenite dunites as well as Fe-rich dunites from Tanzania (Lee and Rudnick, 1999). Also plotted are the spinel trends of the Wiedemann fjord harzburgites (Bernstein et al., 1998) and Sarfartoq garnet-free peridotites (this study). Note the similarity of the Sarfartoq ilmenite dunites and Fe-rich dunites from Tanzania with magmatic spinels from kimberlites (Mitchell, 1995).

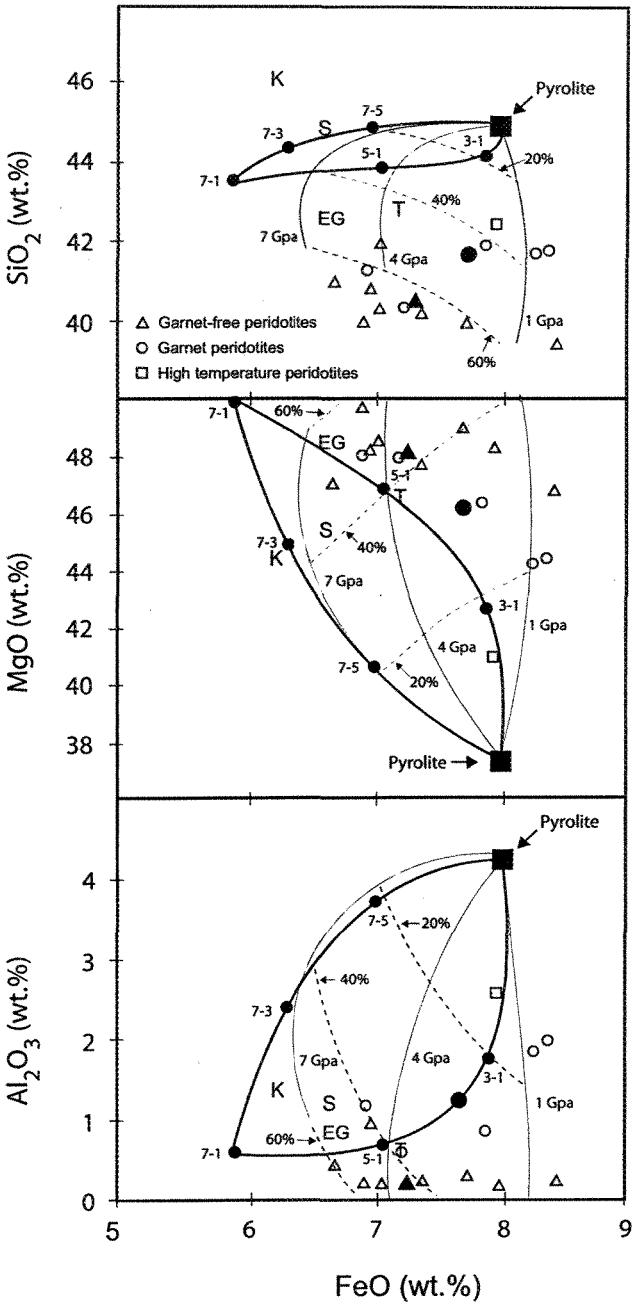

Figure 13: Oxide variation diagrams of average Sarfartoq peridotites compositions relative to melt extract trends of Walter (1998; 1999). Also shown for comparison are Kaapvaal (K; Boyd and Mertzman, 1987), Siberian (S; Boyd et al., 1997) and Tanzanian (T; Lee and Rudnick, 1999) averages. Thin solid lines are isobaric batch melt extraction

contours and dashed lines give percent batch melt extraction. Filled circles connected by thick solid lines are residues of polybaric near-fractional melt extraction and are labeled according to the pressure range of melt extraction. Larger solid symbols (triangle and circle) correspond to averages of the rock type. Only samples with loss on ignition (LOI) values less than 2% were considred. Adapted from Walter (1999).

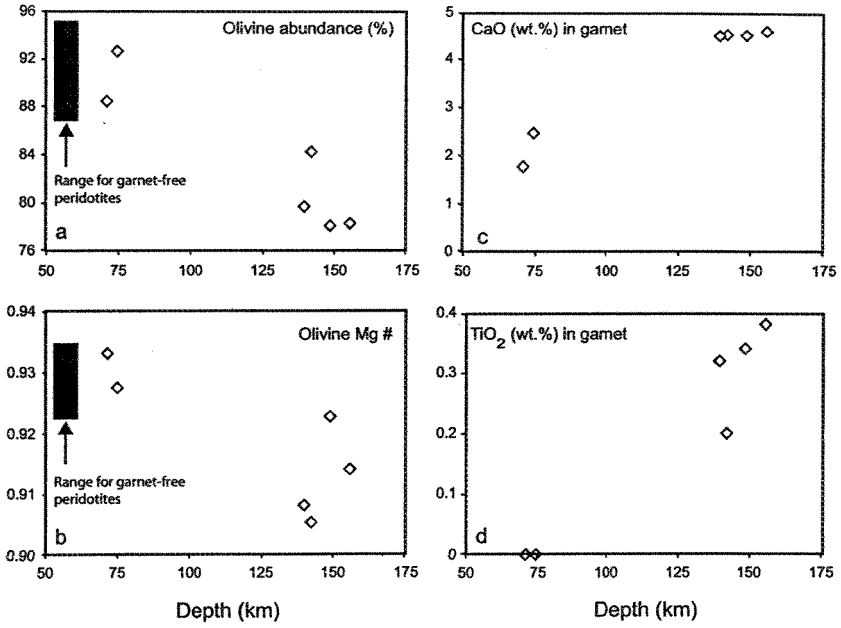

Figure 14: Variation diagrams for six garnet harzburgites from Sarfartoq showing the relation between last depth of equilibration and olivine abundance (%) (a), olivine Mg# (b), and CaO (wt. %) and TiO_2 (wt. %) in garnet (c) and (d). Also shown is the range of variation observed for olivine Mg# and olivine abundance (%) for garnet-free peridotites.

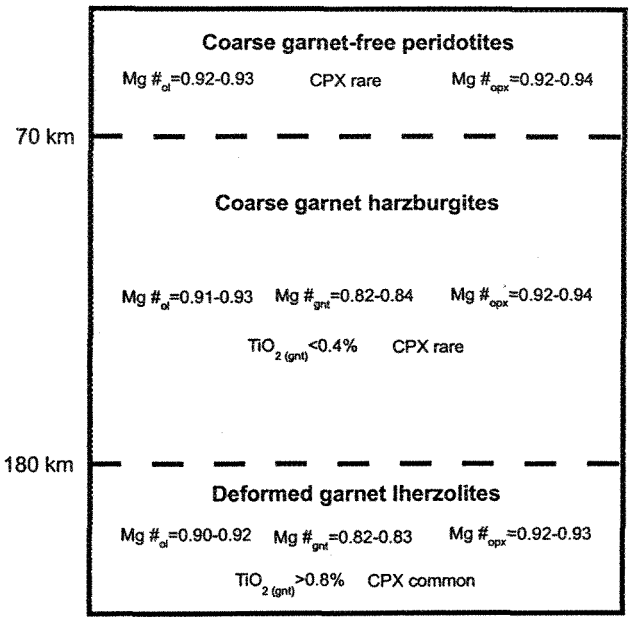

Figure 15: Schematic cross-section of Sarfartoq mantle based on xenolith data.

Chapter II

In Situ $^{87}Sr/^{86}Sr$ Investigation of Igneous Apatites and Carbonates Using Laser Ablation MC-ICP-MS

Martin Bizzarro[1], Antonio Simonetti[1], R.K. Stevenson[1] and Stephan Kurszlaukis[2]

1-GÉOTOP Center, Université du Québec à Montréal, Station Centre-ville, P. O. box 8888, Montréal, Québec, Canada, H3C 3P8.

2-De Beers GeoScience Center, P.O. 82232, Southdale, 2135, South Africa.

ABSTRACT

In situ Sr isotopic compositions of coexisting apatite and carbonate for carbonatites from the Sarfartoq alkaline complex, Greenland, have been determined by laser ablation MC-ICP-MS. This study is the first to examine the extent of Sr isotopic homogeneity amongst coexisting igneous minerals containing high Sr (>3000 ppm) and low Rb (1<< ppm) contents within a single petrographic thin section mount. This technique is capable of producing measured $^{87}Sr/^{86}Sr$ values with analytical precision (~0.004%, 2σ) approaching those obtained by TIMS but in a much shorter interval of time (100 seconds versus ≥1 hour, respectively). The combined total analyses (n=107) of apatite and carbonate yield $^{87}Sr/^{86}Sr$ compositions ranging from ~0.7025 to ~0.7031. This relatively large variation in Sr isotopic compositions (~0.0006) is significantly higher than the estimated external reproducibility (~0.0001, 2σ) of the method. The large range in $^{87}Sr/^{86}Sr$ values suggests that apatite and carbonate precipitated predominantly under non-equilibrium conditions. The isotopic variations observed within individual hand specimens may therefore reflect larger- (regional) scale open-system processes, possibly involving mixing of carbonatitic melts derived from distinct mantle sources, or from a common isotopically heterogeneous mantle.

2.0 INTRODUCTION

The Sarfartoq alkaline province is located on the southwestern coast of Greenland, and consists of a 600 Ma carbonatite intrusive complex on which is centered a contemporaneous kimberlite dike swarm. The latter is interpreted as series of cone sheets dipping towards the core area of the carbonatite (Larsen and Rex, 1992). At numerous localities, the kimberlite dikes are host to peridotite xenoliths. The alkaline complex is intruded into high-grade Precambrian gneisses and straddles the boundary between the southern front of the Proterozoic Nagssuqotidian orogen, and units of the Greenland Western Archean craton. The Nagssuqotidian orogen is an east-northeast trending 150-km wide belt consisting of Archean tonalitic and granodioritic orthogneisses interleaved with Proterozoic orthogneisses and supracrustal units (Kalsbeek et al, 1987; Kalsbeek and Nutman, 1996). The Sarfartoq complex is predominantly magnesio-carbonatite, with lenses of calcio-carbonatite restricted to the core area of the complex (Secher and Larsen, 1980).

Carbonatites, igneous rocks containing >50% carbonate by volume, are ideally suited for laser ablation studies because their constituent minerals (e.g. carbonate and apatite) are Sr-rich (>3000 ppm) and Rb-poor (<<1 ppm) phases. Moreover, carbonate and apatite are not necessarily contemporaneous liquidus phases in carbonatite magmas (Biggar, 1969); thus they can record potential isotopic changes in a dynamic system as each retains the composition of the host magma at different times during the crystallization history of the melt (providing that re-equilibration with the host melt does not occur). As results from melt experiments (e.g. Wallace and Green, 1988) and isotopic data (Nd, Pb, and Sr; e.g. Bell, 1998) have clearly established that carbonatitic melts are of a deep-seated mantle origin, carbonatites can provide valuable information about the composition of the

different mantle sources involved in their genesis (e.g. East African Rift- Bell and Simonetti, 1996; Bell and Tilton, 2001; Deccan alkaline complexes of India- Simonetti et al., 1998; Greenland-Bizzarro et al., in press). The scale at which the 'isotope fingerprinting' of these large-scale mantle processes occurs remains unclear, and whether-or-not these can be traced by small-scale isotopic examination of different minerals within single whole rock samples.

Over the last decade, introduction of multicollector inductively coupled plasma mass spectrometry (MC-ICP-MS) instruments has provided the ability to measure a larger variety of stable and radiogenic isotope systems. This is attributable to their high ion transmission and flexibility for sample introduction, simultaneous detection of ion signals using analogue detectors, and flat-top peaks. These features have combined to generate an instrument capable of producing isotope measurements with precision comparable to those obtained by thermal ionization mass spectrometry (TIMS). Moreover, the coupling of laser ablation systems to MC-ICP-MS instruments has added the potential of providing spatially resolved, high precision measurements for a variety of radiogenic isotope systems, including $^{87}Sr/^{86}Sr$ (Jackson et al., 2001 and references therein). Christensen et al. (1995) first reported the application of laser ablation MC-ICP-MS to Sr isotope studies, and succeeded in obtaining precise and accurate measurements of modern marine gastropods and plagioclase. These experiments, which employed long ablation times (13-17 minutes), documented isotopic disequilibrium between two plagioclase grains from a Long Valley basalt that was interpreted as indicative of magma mixing. Recently, Sr isotope stratigraphy studies of individual plagioclase phenocrysts using either microdrilling (Davidson and Tepley, 1997) or laser ablation-MC-ICP-MS (Davidson et al., 2001) techniques clearly indicate that equilibrium conditions were not attained with the host magma. This feature, indicative of open system behavior, attests to the complex crystallization histories of some

lavas prior to solidification. Moreover, it suggests that certain processes such as wall-rock contamination or magma mixing, can modify the isotopic composition of magmas and may be common attributes of magmatic systems. Investigationsof whole-rock samples make the important assumption that all constituent minerals are in isotopic equilibrium. In magma systems with complex (open system) petrogenetic histories, therefore, whole rock isotopic compositions would simply reflect the average, weighted value for the different minerals with distinct signatures. We have investigated the Sr isotopic composition of individual apatite and carbonate grains for carbonatites from the Sarfartoq complex of southwestern Greenland by LA-MC-ICP-MS. Here, we document (if any) the variation in the $^{87}Sr/^{86}Sr$ composition of coexisting apatite and carbonate, and attempt to constrain the mechanisms generating the observed variations. By comparison with the whole-rock Sr isotopic compositions of associated kimberlites and their host mantle peridotites, we evaluate the contribution of possible mantle sources involved in the genesis of the carbonatite at Sarfartoq.

2.0 ANALYTICAL METHODS

Whole-rock major element compositions of carbonatites were determined with a Philips PW 1400 X-ray fluorescence (XRF) spectrometer using 10-15 grams of powdered rock (Table 1). XRF analyses of major oxides were determined from fused beads prepared from ignited samples, and Sr XRF analyses were determined from pressed pellets. Uncertainties for major (>5%) and minor (<5%) oxides are better than 2% and 5% of quoted values, respectively. The major element compositions of calcites and carbonates were determined with a JEOL 8900 super microprobe (Tables 1, 2). Microprobe analyses were conducted with an acceleration voltage of 15 Kv and beam current at 5 °— 10-8 A, and the diameter set at 5 £gm. Uncertainties for major (>5%) and minor (<5%) oxides analyzed by microprobe are better than 2% and 5% of quoted values, respectively, and 10% and 20% of quoted value for SrO and Ce2O3, respectively.

Laser ablation experiments were conducted on approximately 50 microns thick thin sections prepared for electron microprobe work. In situ Sr isotope analyses were obtained at GEOTOP, Université du Québec à Montréal using a MC-ICP-MS (IsoProbe from Micromass) coupled to a 193 nm (ArF) excimer laser (Compex 102 from Lambda Physik) and optics system by Merchantek-New Wave Research. The ablation was conducted under helium atmosphere in a non-jet ablation cell at a flow rate of approximately 0.5 L/minute. He was used to flush-out the ablation cell instead of Ar since previous studies have clearly shown that the former increases instrument sensitivity due to a higher degree of sample transport efficiency, and reduced deposition at the ablation site (e.g. Eggins et al., 1998; Horn et al., 2000; Fig. 1). Ar gas was mixed into the 'sample-out' line from the ablation cell prior to arrival at the plasma via a 'y-connection' to an ARIDUS® microconcentric nebulizer. Laser pulse energies were in the order of 70 to 90 mJ (25 nanoseconds pulse duration) at a repetition rate of 1 to 2 Hz (depending on the spot size) corresponding to energy densities of approximately 4 to 5 J/cm2 at the sample surface. The spot sizes used for the ablation experiments varied from 80 to 330 microns (Fig. 1). Sr isotope data were obtained in static, multi-collection mode using 6 Faraday collectors. For each sample, data acquisition consisted of a 50 seconds measurement of the gas blank prior to the start of ablation, a similar method as employed by Davidson et al. (2001) for an IsoProbe MC-ICP-MS. This measurement is critical since it monitors the 86Kr, which interferes with the 86Sr signal. The isobaric interference of 87Rb was monitored by measuring the 85Rb ion signal (e.g. Table 3). Using Rb-doped synthetic glass standards, Davidson et al. (2001) investigated the relationship between the Rb/Sr ratio in feldspars versus their measured $^{87}Sr/^{86}Sr$ value obtained during laser ablation. The results indicate that for Rb-doped standards with Rb/Sr ratios of ~0.0015, the 87Sr/86Sr values obtained by laser ablation were roughly 0.0001 higher compared to those obtained by TIMS analysis for the same standards. The Rb/Sr values for the majority of the carbonate and apatite grains investigated

here (Table 3), however, are much lower than 0.0015 (average=0.00004, n=107) and therefore the ^{87}Rb interference on the measured $^{87}Sr/^{86}Sr$ is considered negligible. In the extreme case, it is approximately the same magnitude as the typical 2£m internal precision (~0.00005) associated with the $^{87}Sr/^{86}Sr$ value for individual laser ablation analyses. The effectiveness of the combined interference corrections (i.e. Kr, Rb) applied to the analyses can be directly evaluated by monitoring the invariant $^{84}Sr/^{88}Sr$ (0.00675) and $^{84}Sr/^{86}Sr$ (0.0565) values, and these are listed in Table 3. It is extremely important to carefully monitor these invariant ratios since the presence of either doubly-charged middle to heavy rare earth elements (masses 144 to 176 divided by Z=2+), molecular species from Ca (^{42}Ca2, ^{43}Ca2, ^{44}Ca2), or oxides of Fe (^{54}Fe or ^{56}Fe +2(^{16}O)) formed during the ablation process, would create isobaric interferences within the mass range used for Sr isotope data acquisition. Ion beam intensities for most samples varied from ~2 to 5x10-11 A of ^{88}Sr. Time-resolved analysis for the ablation runs was not needed because of the simultaneous acquisition of the ion signals (multi-collection), and the relative stability of the ion signals (average error~2%) resulting in high in run precision (Table 3). Subsequent to the start of laser ablation, two half mass unit baseline measurements were obtained for each Faraday collector (within the mass range 82.5 to 88.5), followed by ion signal measurements of 100 seconds interval (50 integrations of 2 seconds each). The measured Sr isotope ratios were normalized to $^{86}Sr/^{88}Sr$= 0.1194 and corrected for instrumental mass bias using the exponential law (Russell et al., 1978). Sr isotopic ratios obtained for repeated analyses of a 100 ppb solution of the standard NBS 987 (n=5) for the analytical sessions in which both solution mode and laser ablation analyses were carried out yield the following values (2£m uncertainties): $^{87}Sr/^{86}Sr$=0.71025 ±7, $^{84}Sr/^{86}Sr$=0.05659 ±29, $^{84}Sr/^{88}Sr$=0.006758 ±34. These are well within the accepted Sr isotopic composition for this standard, thus validating the Sr isotope data obtained in solution mode. Samples selected for whole-rock Sr isotopic analysis by thermal ionization mass spectrometry (TIMS) were dissolved in a mixture of

HF-HCl-HNO3 in Savilex® beakers for 48 hrs. Sr separation was achieved by standard cation exchange chromatography, and subsequently loaded onto a single filament (Re) with a HCl-HNO3-TaO solution for analysis using a VG-54 Sector multi-collector mass spectrometer. Analyses were obtained in static, multi-collection mode and during the period of this study, repeated analysis of the NBS-987 standard yielded an average $^{87}Sr/^{86}Sr$ value of 0.71024 °"4 (2£m standard deviation; n=10; normalized to $^{86}Sr/^{88}Sr$=0.1194). This $^{87}Sr/^{86}Sr$ value is identical to that obtained in solution mode MC-ICP-MS analysis.

2.3 RESULTS

3.1 Mineral chemistry

The calcio-carbonatites, which were selected for the laser ablation work (Table 1), consist of calcite and dolomite with subordinate amounts of apatite, phlogopite, magnetite and ilmenite, and accessory phases include richterite-arfvedsonite, pyrochlore, pyrite and zircon (Secher and Larsen, 1980). Mineral segregation textures are evidenced by clusters of apatite, or bands of large carbonate crystals associated with Fe-oxide minerals (Fig. 2a). Apatite crystals, ranging in size from 0.1 mm to 0.5 cm, demonstrate a wide range of petrographic habits from euhedral to irregular morphologies. Large apatite crystals often show textural disequilibrium features such as resorbtion and embayment (Fig. 3). A number of electron microprobe traverses were conducted along large apatite crystals exhibiting textural disequilibrium features so as to investigate the extent of chemical zoning. Results indicate that the major and trace (Sr, Ce) element composition of apatite is homogeneous, with no systematic variation between cores and rims (Table 2). Moreover, image analyses including backscattered-electron (Fig. 3a and 3c) and cathodoluminescence (not shown) on a number of apatite crystals selected for laser ablation work do not reveal any evidence of trace element zoning. Carbonate crystals exhibit a wide range of grain sizes, with the predominant texture being large crystals (2 to 10 mm) set in a fine-grained interstitial matrix (<1 mm; Fig. 2b).

3.2. In-situ Sr isotope analysis- external reproducibility

A sample of modern-day coral from the "ribbon-reef" deposit surrounding Mayotte Island in the Indian Ocean (latitude: 12°50'S, longitude: 45°20'E; Colonna, 1994) yields a Uth age of 4663 ± 80 years (B. Ghaleb, pers. comm.) was investigated for its Sr isotopic composition so as to determine the external reproducibility (2σ) of the methodology employed in this study. The laser ablation experiments were conducted over two consecutive days, and repeated measurements (n=30) using a 80 microns spot size yield an average $^{87}Sr/^{86}Sr$ value of 0.709097 ±0.000047 (2σ) with corresponding average 84Sr/86Sr and 84Sr/88Sr ratios of 0.00672 ± 0.00004 (2σ) and 0.0562 ± 0.0003 (2£m standard deviation), respectively (Fig. 4a). Of interest, the 2σ external reproducibility obtained for the sample of coral is almost identical to the average 2σ internal precisions of ±0.00005 and ±0.00007 for the carbonate and apatite, respectively (as calculated from uncertainties listed in Table 3). The accuracy of the laser ablation results was investigated by obtaining TIMS measurements on four separate fragments of the coral. These four fragments, weighing approximately 0.050 grams each, were dissolved and Sr separated using conventional cation exchange chromatography. The Sr isotopic results obtained by TIMS are listed in Table 4, and yield an average $^{87}Sr/^{86}Sr$ value of 0.709098 ±0.000019 (2σ). The latter is identical to the average Sr isotopic composition based on the laser ablation runs, and thus provides strong evidence for the accuracy of the results obtained in this study.

For comparison, a mollusk sample from a terrace deposit located at Esmeraldas (northwestern Ecuador) yields a U-Th date of ~55,000 years; however, the accurate stratigraphic age for the terrace deposit is ~125,000 years (B. Ghaleb, pers. comm.). This feature was attributed to post-depositional, open-system behaviour suffered by the mollusk. Figure 4b illustrates the measured $^{87}Sr/^{86}Sr$ values obtained for 35 analyses of the mollusk over the period of this study. The average $^{87}Sr/^{86}Sr$ value is 0.70901 ±0.0001 (2σ), and the

average $^{84}Sr/^{86}Sr$ and $^{84}Sr/^{88}Sr$ ratios obtained are 0.0567 ± 0.0004 (2σ) and 0.00677 ± 0.00008 (2σ), respectively. In contrast to the laser ablation results from the coral, the external reproducibility (2σ, ±0.0001) for the Sr isotopic measurements of the mollusk is twice as large, and roughly double the average internal precision for the individual ablation analyses (Fig. 4b). Thus, the large-scale isotopic homogeneity of the mollusk was investigated using two sample fragments (0.050 and 0.130 grams) taken randomly from the piece complementary (i.e. other half) to the one used for the laser ablation experiment. These were dissolved, then processed through conventional cation exchange chromatography, and analyzed in solution mode MC-ICP-MS. The Sr isotopic ratios for the two fragments (also shown in Fig. 4b) exhibit a certain degree of isotopic heterogeneity, and essentially bracket the results for the individual laser ablation analyses. Thus, the distribution of the laser ablation data for the mollusk is not entirely instrument-induced, but simply reflects the inherent isotopic heterogeneity of the sample. In summary, the laser ablation Sr isotopic values obtained for both the samples of coral and mollusk indicate the effectiveness of the technique in detecting isotopic heterogeneity within a single sample at the millimeter scale.

The values obtained for the $^{84}Sr/^{86}Sr$ and $^{84}Sr/^{88}Sr$ measurements for both the coral and mollusk samples are within error of the accepted reference values (0.0565 and 0.00675, respectively), thus validating the methodology and proving the effectiveness of the correction for the gas blank (i.e. ^{86}Kr). For sample SARF-03, however, the measured $^{87}Sr/^{86}Sr$ compositions are clearly correlated with the $^{84}Sr/^{86}Sr$ values (Fig. 5a) indicating that the variation in the former are an analytical artefact. This is clearly not the case for sample SARF-10 (Fig. 5b), and therefore suggests that this contrasting behavior is related to a significant difference in the major element composition of the SARF-03 carbonates. The major element compositions of samples SARF –03 and –10 are listed in Table 1, and

one significant difference is the higher Fe content in the former compared to the latter (4.13 vs. 2.06 wt%, respectively). It is possible that isobaric interferences on masses 86 and 88 related to Fe-oxides produced during the laser ablation result in erroneous corrections of the mass bias (using the $^{86}Sr/^{88}Sr$=0.1194), which in turn yield inaccurate $^{87}Sr/^{86}Sr$ values.

In order to more accurately assess this hypothesis, a series of laser ablation experiments were conducted with the assistance of back-scattered electron imaging and electron microprobe analysis in order to clearly distinguish between dolomite and calcite grains (Fig. 6a). The results of thirteen laser ablation analyses of dolomite grains in an area (2.5 mm^2) of sample SARF-10 are plotted in a diagram of $^{84}Sr/^{86}Sr$ versus $^{87}Sr/^{86}Sr$ (Figs. 6b, c). The results clearly show once again a significant correlation between these two ratios for the dolomites ($y = -4.9577x + 3.5403$, $r^2 = 0.78$; Fig. 6c), whereas a similar plot (not shown) for analyses of neighboring calcite grains (n=6) are completely scattered. Lastly, the Sr isotopic results for the dolomites (Fig. 6c) indicate that the analyses closest to the accepted $^{84}Sr/^{86}Sr$ value (i.e. 0.0565) are characterized by the least radiogenic $^{87}Sr/^{86}Sr$ composition (<0.7027).

3.3. In-situ Sr isotope analyses – magmatic carbonate and apatite

LA-MC-ICP-MS results for carbonates and apatites are listed in Table 3. Reconnaissance analyses were conducted principally on cores of apatite and carbonate crystals for five different thin sections from sample SARF-10. Forty-seven in situ analyses of apatites, using spot sizes ranging from 150 to 330 μm, yield a large range of $^{87}Sr/^{86}Sr$ values for all sections, i.e. from 0.70252 to 0.70317. Similarly, 60 analyses of carbonate from the five different thin sections yielded a range of values between 0.70253 and 0.70300 (Fig. 7). The observed spread in $^{87}Sr/^{86}Sr$ ratios overlaps the average TIMS whole rock value of 0.70279 ±4 (2σ; n=5) for this sample. A number of whole-rock powder samples were leached in order to assess the possible extent of isotopic heterogeneity due to the presence of low-temperature sub-solidus phases of distinct isotopic composition. Seven

HCl leachates (carbonate fraction) from samples representing different parts of the outcrop area (25 m^2) were analyzed by TIMS, and yielded Sr isotope compositions between 0.70276 to 0.70284 (average= 0.70280 ±4; n=7). The range defined by TIMS analyses does not bracket the peak observed in the both the carbonate or apatite distributions, but is slightly offset to less radiogenic compositions (Fig. 8). Although no correlation exists between ^{88}Sr ion signal intensity (i.e. Sr abundance) and isotopic composition, the offset in the histogram distribution suggests that carbonate and apatite grains containing the least radiogenic Sr isotope compositions have the highest strontium content. Contrarily, the average $^{87}Sr/^{86}Sr$ compositions calculated for both apatite and carbonate using the individual laser ablation runs (0.70284 and 0.70280, respectively; Table 3) are identical to one another (within error) and to the whole rock Sr isotope values obtained by TIMS analysis (0.70279).

There is some evidence to suggest that the Sr isotopic composition does correlate with the petrographic textures of the carbonate crystals. Five analyses of fine-grained interstitial carbonate (e.g. Fig. 2b) yielded radiogenic compositions (0.70289±8) compared to the range defined by the larger crystals (0.7026 to 0.7030). In addition, the least radiogenic isotopic compositions are typically recorded by carbonate in close association with magnetite crystals, and are also characterized by the presence of zoned phlogopite inclusions (Fig. 2a). The latter are generally absent in the large carbonate crystals which are ubiquitous throughout the sections. Core-rim analyses of the micas reveal that they are characterized by an increase in Fe, and decrease in both Al and, to lesser extent, Si contents (Table 5). These compositional trends are typical of crystallization in the presence of magnetite, which forms during the latter stages of the solidification history of carbonate magmas, driving the composition of the micas towards tetra-ferriphlogopite (McCormick and Le Bas, 1996). Thus, it is likely that the phlogopite-bearing carbonate crystals with relatively unradiogenic Sr isotopic compositions formed during the late stages of the

crystallization history of the melt.

Potential isotopic heterogeneity within individual apatite crystals was investigated by conducting traverses across several relatively large apatite grains. The $^{87}Sr/^{86}Sr$ compositions measured across these two traverses show negligible isotopic variations (Fig. 9), and are thus considered to be in isotopic equilibrium. The traverses illustrated in Figure 9 indicate that one apatite grain records slightly more radiogenic Sr isotopic compositions than the range outlined by TIMS, whereas the other grain is characterized by values that are within the TIMS analyses.

2.4 DISCUSSION

4.1 Isotopic disequilibria

LA-MC-ICP-MS data for the apatite and carbonate crystals strongly suggest that these minerals precipitated under non-equilibrium conditions. The large spread in Sr isotopic ratios recorded by these minerals indicates that the melt was undergoing extensive isotopic change during crystallization. In addition, the apatites and carbonates define a similar spread in Sr isotopic ratios (Figs. 7 and 8). This feature suggests that crystallization of apatite and carbonate occurred concurrently throughout the solidification history of the sample. Experimental studies have demonstrated that apatite and carbonate may represent simultaneous liquidus phases over a wide range of pressures and temperatures (e.g. Wyllie et al., 1962; Biggar, 1969; Hoggart, 1989). This is in accordance with the petrographic features of the studied samples since both apatite and carbonate crystals occur as cumulus and inter-cumulus phases. As such, both minerals can potentially monitor the isotopic evolution of the melt during crystallization. The range of $^{87}Sr/^{86}Sr$ values in apatites and carbonates is consistent with mixing of distinct generations of crystals cognate to a melt undergoing progressive change in isotopic composition. This may be achieved by melting

under open system conditions resulting in mixing of components (melts, fluids) with different $^{87}Sr/^{86}Sr$ isotopic ratios. The spread of data may thus be reconciled with either (1) a melt with a high initial $^{87}Sr/^{86}Sr$ undergoing progressive exchange with a less radiogenic component, or, alternatively, (2) an initial melt with a low Sr isotopic composition evolving towards high $^{87}Sr/^{86}Sr$ values. As discussed earlier, lower Sr isotopic compositions have been recorded by large carbonate crystals associated with oxide (magnetite) segregations. The core-rim variations observed in phlogopite crystals present as inclusions in the carbonate with lower isotopic compositions suggest that these precipitated during later stages of the crystallization history of the magma. Therefore, the isotopic composition recorded by the carbonate crystals in which phlogopite inclusions with tetra-ferriphlogopite rims occur may represent the isotopic composition of the melt during a later stage of the crystallization sequence, while other carbonate crystals may record secular isotopic changes experienced by the melt upon initial melting. In this respect, it is possible that the range of $^{87}Sr/^{86}Sr$ recorded by the large carbonate and apatite crystals may be explained by crystal fractionation from a melt of initially high $^{87}Sr/^{86}Sr$ composition undergoing isotopic exchange with a low $^{87}Sr/^{86}Sr$ component. The correlation observed between isotopic composition and texture within carbonate crystals supports episodic melt replenishment, and the isotopic composition of the fine-grained carbonate crystals may thus represent the isotopic nature of a scavenging melt.

4.2 Mantle sources

The isotopic signatures of mantle components most likely involved in the genesis of the carbonatite complex at Sarfartoq, i.e. plume material and subcontinental mantle (SCM), have been characterized through the study of peridotite xenoliths and host kimberlites

(Bizzarro and Stevenson, unpublished). Peridotite xenoliths yield an average Sr isotopic composition of 0.70225 ±27 (2σ; n=8), whereas the kimberlites, possible derivatives of the plume component, have an average whole rock $^{87}Sr/^{86}Sr$ ratio of 0.70297 ±6 (2σ; n=5). In addition, a number of carbonatite samples from the Sarfartoq alkaline complex yield an average whole-rock $^{87}Sr/^{86}Sr$ ratio of 0.70276 ±8 (2σ; n=4). The whole rock data clearly indicates that the carbonatites at Sarfartoq may not have been generated by melting of SCM, but necessitate the involvement of a more radiogenic component such as plume material (Fig. 8b). The range in $^{87}Sr/^{86}Sr$ ratios recorded by apatites and carbonates (0.7025-0.7031) overlaps the isotopic compositions of kimberlites, carbonatites and peridotite xenoliths at Sarfartoq. This indicates that the observed spread of Sr isotopic compositions may be generated by the mixing of at least two end members, represented by kimberlites and peridotites (i.e. plume and lithosphere), respectively. Thus, the Sr isotope compositions for the apatite and carbonate crystals can represent a record of temporal evolution of a plume-derived magma undergoing isotopic exchange with the overlying SCM reservoir. It is possible that the Sr isotopic variations defined by apatite and carbonate at the scale of individual hand specimens are a reflection of larger- (regional) scale open system processes involving mixing of distinct mantle sources, which include SCM and up-welling plume material. Alternatively, Bell and Tilton (2001) have recently proposed carbonatite generation via plumes originating from the deep mantle (bottom 1000 km) involving the HIMU and EM1 mantle components. The HIMU-EM1 mixing trends observed in African carbonatites do not reflect interaction of a plume (HIMU) component with enriched lithosphere (EM1), but stems from the isotopic heterogeneity of the plume

source itself (Bell and Tilton, 2001). The variation in $^{87}Sr/^{86}Sr$ compositions documented in this study may therefore also be explained by isotopic heterogeneity inherent to the plume source.

2.5 CONCLUSIONS

This study is the first to report $^{87}Sr/^{86}Sr$ compositions for coexisting igneous minerals (carbonate and apatite) from the same petrographic thin section. Based on the results presented here, the LA-MC-ICP-MS method provides a rapid and effective approach to determine the extent of isotopic heterogeneity within a single sample or individual grains, with analytical precision approaching that obtained by TIMS. This study reveals the importance of detailed, in situ isotopic work for deciphering the complex dynamics of magmatic systems. The laser ablation data obtained here reveals a somewhat complicated petrogenetic history for the Sarfartoq carbonatite complex, involving crystal fractionation under open system conditions with possible interaction of different mantle reservoirs. The range of $^{87}Sr/^{86}Sr$ values recorded by apatite and carbonate indicate that the melt was undergoing progressive isotopic exchange throughout its crystallization history. Compared to the whole rock Sr isotopic compositions for associated kimberlites, carbonatites and mantle-derived peridotites (obtained by TIMS), the laser ablation data obtained here may be attributed to the interaction of plume and SCM reservoirs which took place during generation of the carbonatite at Sarfartoq. Alternatively, the observed isotopic variations may reflect isotopic heterogeneity within a plume mantle source (Bell and Tilton, 2001).

Acknowledgements-Financial support for this project was provided through a NSERC grant to RKS. MB acknowledges the FCAR (*Fonds pour la Formation de Chercheurs et l'aide a la Recherche) Bourse de Recherche en Milieu Pratique* program for a Ph.D. scholarship.

De Beers Canada Exploration Inc. are thanked for support during fieldwork. Glenn Poirier and Glenna Keating (both at McGill University, Montréal, Canada) are thanked for help with the microprobe and XRF analyses, respectively. Reviews by Andrew Campbell and two anonymous reviewers are acknowledged.

REFERENCES

Bell K. (1998) Radiogenic isotope constraints on relationships between carbonatite and associated silicate rocks—A brief review. *Journal of Petrology* 39, 1987-1996.

Bell K. and Simonetti A. (1996) Carbonatite magmatism and plume activity: implications from the Nd, Pb and Sr isotope systematics of Oldoinyo Lengai. *Journal of Petrology* 37, 1321-1329.

Bell K. and Tilton G. R. (2001) Nd, Pb and Sr isotopic compositions of East African carbonatites: Evidence for mantle mixing and plume inhomogeneity: *Journal of Petrology*, 42, 1927-1945.

Biggar G. M. (1969) Phase relationships in the join $Ca(OH)_2$-$CaCO_3$-Ca_3PO_4-H2O at 1000 bars. *Mineralogical Magazine* 37, 75-82.

Bizzarro, M., Simonetti, A., Stevenson, R.K. and David, J. (in press) Hf isotope evidence for a hidden mantle reservoir. *Geology*.

Christensen J. N., Halliday A. N., Lee, D.-C. and Hall C. M. (1995) In situ Sr isotopic analysis by laser ablation. *Earth Planetary Science Letters* 136, 79-85.

Colonna, M. (1994) Chronologie des variations du niveau marin au cours du dernier cycle climatique (0-140 000 ans) dans la partie occidentale de l'océan Indien. Ph.D. thesis, Université de Provence, France.

Davidson J. P., Tepley III F. J. (1997) Recharge in volcanic systems; evidence from isotopic profiles of phenocrysts. *Science* 275, 826-829.

Davidson J., Tepley III F., Palacz Z. and Meffan-Main S. (2001) Magma recharge, contamination and residence times revealed by in situ laser ablation isotopic analysis of feldspar in volcanic rocks: *Earth and Planetary Science Letters*, 184, 427-442.

Eggins S. M., Kinsley L. P. J. and Shelley J. M. G. (1998) Deposition and element fractionation processes during atmospheric pressure sampling for analysis by ICP-MS. *Applied Surface Science* 127-129, 278-286.

Hoggart D. D. (1989) Pyrochlore, apatite and amphibole: distinctive minerals in carbonatites. In *Carbonatites, Genesis and Evolution* (Ed. K. Bell). pp. 105-148.

Horn I., Rudnick R. L. and McDonough W. F. (2000) Precise elemental and isotope ratio determination by simultaneous solution nebulization and laser ablation-ICP-MS: application to U-Pb geochronology. *Chemical Geology* 164, 281-301.

Jackson S. E., Pearson N. J. and Griffin W. L. (2001) In situ isotope ratio determination using laser-ablation (LA)- magnetic sector-ICP-MS. In *Laser-Ablation-ICP-MS in the Earth Sciences* (Ed. P.J. Sylvester). Mineral. Assoc. Canada Short course series volume 29, pp. 105-119.

Kalsbeek F., Pidgeon R. T. and Taylor P. N. (1987) Nagssugtoqidian mobile belt of West Greenland: a cryptic 1850 Ma suture between two Archaean continents-chemical and isotopic evidence. *Earth and Planetary Science Letters* 85, 385-395.

Kalsbeek F. and Nutman A. P. (1996) Anatomy of the Early Proterozoic Nagssugtoqidian Orogen, West Greenland, explored by reconnaissance SHRIMP U-Pb dating. *Geology* 24, 515-518.

Larsen L. M. and Rex D. C. (1992) A review of the 2500 Ma span of alkaline-ultramafic, potassic and carbonatitic magmatism in West Greenland. *Lithos* 28, 367-402.

McCormick G. R. and Le Bas M. J. (1996) Phlogopite crystallization in carbonatitic magmas from Uganda. *Canadian Mineralogist* 34, 469-478.

Russell W. A., Papanastassiou D. A., and Tombrello T. A. (1978) Ca isotope fractionation on the Earth and other solar system materials. *Geochimica Cosmochimica Acta* 42, 1075-1090.

Secher K. and Larsen L. M. (1980) Geology and mineralogy of the Sarfartoq carbonatite complex, southern West Greenland. *Lithos* 13, 199-212.

Simonetti A., Goldstein S. L., Schmidberger S. S. and Viladkar S. G. (1998) Geochemical and Nd, Pb, and Sr isotope data from Deccan alkaline complexes- inferences for mantle sources and plume-lithosphere interaction. *Journal of Petrology* 39, 1847-1864.

Wallace M. E. and Green D. H. (1988) An experimental determination of primary carbonatite magma composition: *Nature* 335, 343-346.

Wyllie P. J., Cox K. G. and Biggar, G. M., (1962) The habits of apatite in synthetic systems and igneous rocks. *Journal of Petrology* 3, 238-243.

Table 1: Major element compositions of whole-rock carbonatites and average compositions of associated carbonates.

	SARF-10			SARF-03	
	Whole-rock	***Calcite (n=6)***	***Dolomite (n=5)***	***Whole-rock***	***Dolomite (n=31)***
SiO_2	0.60			0.03	
TiO_2	0.01			0.01	
Al_2O_3	0.17			0.02	
FeO	2.06	0.35	3.47	4.13	4.92
MnO	0.25	0.21	0.31	0.59	0.59
MgO	8.20	0.48	18.60	16.85	17.64
CaO	39.03	54.84	29.23	28.73	28.09
Na_2O	0.05			0.06	
K_2O	0.06			0.00	
P_2O_5	4.71			0.11	
SrO	0.39	0.58	0.30	0.90	0.96
LOI/CO_2	44.24	43.54	48.09	48.24	47.80
Total	99.8	100.0	100.0	99.7	100.0

Analyses reported in weight %. Whole-rock major element compositions of carbonatites were determined with a Philips PW 1400 X-ray fluorescence (XRF) spectrometer using 10-15 grams of powdered rock, while the major element compositions of calcites and carbonates were determined with a JEOL 8900 super microprobe (both at McGill University, Montréal, Canada). XRF analyses of major oxides were determined from fused beads prepared from ignited samples, and Sr XRF analyses were determined from pressed pellets. Uncertainties for major (>5%) and minor (<5%) oxides are better than 2% and 5% of quoted values, respectively. Microprobe analyses were conducted with an acceleration voltage of 15 Kv and beam current at 5×10^{-8} A, and the diameter set at 5 μm. Uncertainties for major (>5%) and minor (<5%) oxides analyzed by microprobe are better than 2% and 5% of quoted values, respectively, and 10% of quoted value for SrO.

Table 2: Major element variation amongst single apatite crystals.

Spot #	F	Na_2O	P_2O_5	CaO	Ce_2O_3	SrO	SO_3	FeO	Total
Apatite 1									
1	2.24	0.17	41.82	54.34	0.31	0.48	0.02	0.07	99.45
2	2.37	0.24	41.62	54.18	0.18	0.51	0.05	0.07	99.21
3	2.21	0.24	41.36	54.12	0.13	0.49	0.03	0.09	98.67
4	2.19	0.22	41.62	54.36	0.17	0.46	0.05	0.08	99.15
5	2.15	0.25	41.42	54.10	0.13	0.51	0.03	0.06	98.65
6	2.46	0.18	41.80	54.38	0.14	0.54	0.02	0.04	99.56
7	2.13	0.23	41.31	54.29	0.15	0.48	0.04	0.08	98.72
8	2.15	0.24	41.45	54.07	0.20	0.50	0.05	0.10	98.75
9	2.16	0.22	41.66	53.92	0.13	0.53	0.04	0.09	98.74
10	2.14	0.18	41.12	54.39	0.17	0.59	0.04	0.06	98.68
11	2.04	0.24	41.66	53.50	0.20	0.51	0.04	0.08	98.26
12	2.33	0.23	41.66	54.18	0.15	0.50	0.07	0.09	99.20
Apatite 2									
1	2.33	0.24	41.42	54.05	0.15	0.46	0.06	0.11	98.80
2	2.45	0.17	41.36	54.38	0.16	0.49	0.04	0.06	98.16
3	2.58	0.13	41.69	54.15	0.18	0.46	0.00	0.03	98.34
4	3.15	0.14	41.30	53.99	0.21	0.52	0.02	0.03	98.26
5	2.63	0.14	41.65	54.44	0.19	0.54	0.01	0.07	98.74
6	2.54	0.13	41.64	54.16	0.21	0.49	0.02	0.03	98.38
7	2.47	0.15	41.69	54.19	0.22	0.49	0.00	0.06	98.28
Apatite 3									
1	2.22	0.24	41.23	54.19	0.16	0.44	0.05	0.11	98.65
2	2.17	0.24	41.75	54.03	0.17	0.47	0.05	0.09	98.96
3	2.33	0.17	41.65	54.36	0.24	0.54	0.02	0.05	99.36
4	2.17	0.20	41.37	54.18	0.27	0.54	0.03	0.10	98.84

Analyses reported in weight %. Apatite 1 is 6.5 mm long and 2.5 mm wide, apatite 2 is 3 mm long and 1.2 wide, and apatite 3 is 2.1 mm long and 1 mm wide. Analyses were distributed homogeneously along the length of the crystals. All apatites are characterized by textural disequilibrium features (e.g. Fig. 3). Microprobe analyses were conducted with the same operating conditions as outlined in Table 1. Analytical uncertainties for Ce_2O_3 and SrO are 20% and 10% of quoted values, respectively, and as outlined in Table 1 for remaining elements.

Table 3: Sr isotopic ratios measured by LA-MC-ICP-MS for SARF-10 apatites and carbonates.

Analysis #	Pit size (mm)	$^{87}Sr/^{86}Sr$	$^{84}Sr/^{88}Sr$	$^{84}Sr/^{86}Sr$	^{88}Sr (V)	^{85}Rb (10^{-3}V)
Apatites						
1	330	0.70291 (05)	0.00677 (1)	0.05669 (11)	3.21	0.00
2	330	0.70289 (04)	0.00675 (1)	0.05650 (06)	4.85	0.00
3	330	0.70289 (04)	0.00677 (1)	0.05670 (06)	5.1	0.01
4	330	0.70290 (03)	0.00674 (1)	0.05644 (05)	4.92	0.01
5	330	0.70287 (03)	0.00676 (1)	0.05663 (05)	4.9	0.00
6	330	0.70288 (02)	0.00678 (1)	0.05676 (06)	4.98	0.00
7	330	0.70288 (03)	0.00677 (1)	0.05674 (05)	5.02	0.21
8	330	0.70288 (04)	0.00676 (1)	0.05663 (06)	4.91	0.00
9	330	0.70281 (03)	0.00677 (7)	0.05673 (06)	5.07	0.02
10	150	0.70273 (04)	0.00679 (1)	0.05683 (06)	4.9	0.01
11	150	0.70285 (04)	0.00673 (1)	0.05640 (08)	4.9	0.12
12	150	0.70277 (04)	0.00680 (1)	0.05694 (06)	4.9	0.01
13	150	0.70287 (08)	0.00674 (1)	0.05645 (12)	4.56	0.10
14	150	0.70278 (05)	0.00678 (1)	0.05680 (09)	4.86	0.06
15	150	0.70283 (05)	0.00678 (1)	0.05675 (09)	4.49	0.08
16	150	0.70289 (04)	0.00676 (1)	0.05659 (07)	4.2	0.49
17	150	0.70289 (05)	0.00671 (1)	0.05623 (10)	4	0.07
18	330	0.70284 (08)	0.00670 (3)	0.05609 (26)	1.12	0.00
19	330	0.70297 (10)	0.00676 (4)	0.05669 (35)	0.74	0.00
20	330	0.70281 (11)	0.00680 (3)	0.05694 (24)	1.26	0.00
21	330	0.70281 (10)	0.00670 (3)	0.05611 (25)	1.25	0.00
22	330	0.70304 (09)	0.00670 (3)	0.05609 (25)	1.31	0.00
23	330	0.70304 (16)	0.00674 (4)	0.05644 (33)	0.74	0.96
24	330	0.70292 (08)	0.00671 (2)	0.05619 (18)	1.6	0.06
25	330	0.70284 (04)	0.00671 (1)	0.05622 (11)	3.62	0.02
26	330	0.70278 (07)	0.00672 (1)	0.05630 (10)	3.12	0.00
27	330	0.70291 (05)	0.00670 (1)	0.05607 (11)	2.77	0.13
28	150	0.70252 (18)	0.00674 (5)	0.05643 (44)	0.72	0.01
29	330	0.70317 (10)	0.00678 (2)	0.05680 (20)	1.85	0.84
30	330	0.70289 (08)	0.00679 (2)	0.05689 (17)	1.92	0.08
31	330	0.70284 (08)	0.00680 (2)	0.05694 (18)	1.79	0.00
32	330	0.70280 (15)	0.00676 (2)	0.05663 (17)	1.58	0.00
33	330	0.70280 (13)	0.00680 (2)	0.05693 (20)	1.52	0.01
34	330	0.70264 (08)	0.00679 (2)	0.05690 (18)	1.65	0.05
35	330	0.70269 (08)	0.00677 (2)	0.05666 (16)	1.69	0.04

36	330	0.70268 (13)	0.00677 (2)	0.05672 (16)	1.63	0.00
37	330	0.70267 (14)	0.00679 (2)	0.05684 (16)	1.66	0.02
38	330	0.70304 (13)	0.00670 (2)	0.05614 (17)	1.67	0.00
39	330	0.70279 (09)	0.00675 (2)	0.05655 (18)	1.54	0.00
40	330	0.70262 (10)	0.00675 (3)	0.05655 (21)	1.56	0.03
41	150	0.70284 (04)	0.00673 (1)	0.05636 (06)	4.78	0.09
42	150	0.70297 (05)	0.00666 (1)	0.05579 (07)	4.58	0.08
43	150	0.70279 (05)	0.00672 (1)	0.05629 (080	4.76	0.10
44	150	0.70282 (03)	0.00674 (1)	0.05643 (05)	4.59	0.05
45	150	0.70287 (03)	0.00671 (1)	0.05623 (07)	4.66	0.08
46	330	0.70297 (05)	0.00673 (1)	0.05640 (06)	5.72	0.07
47	330	0.70294 (04)	0.00677 (1)	0.05672 (07)	5.52	0.03
	Averages	***0.70285 (24)***	***0.00675 (7)***	***0.05654 (28)***	***3.25***	***0.08***
Coarse-grained carbonates						
1	330	0.70297 (06)	0.00669 (2)	0.05600 (14)	2.26	0.00
2	330	0.70269 (05)	0.00674 (1)	0.05644 (04)	3.42	0.08
3	330	0.70277 (11)	0.00676 (3)	0.05658 (24)	1.17	0.01
4	330	0.70266 (03)	0.00677 (1)	0.05671 (05)	5.78	0.01
5	330	0.70298 (10)	0.00671 (4)	0.05618 (29)	1.05	0.15
6	330	0.70291 (06)	0.00671 (7)	0.05616 (62)	0.48	0.00
7	100	0.70283 (04)	0.00676 (1)	0.05660 (05)	6.99	0.14
8	330	0.70291 (11)	0.00679 (1)	0.05687 (06)	6.64	0.00
9	150	0.70277 (05)	0.00675 (1)	0.05653 (06)	6.92	0.26
10	330	0.70281 (04)	0.00679 (1)	0.05688 (06)	3.64	0.07
11	150	0.70289 (04)	0.00673 (1)	0.05638 (06)	4.87	0.01
12	330	0.70254 (03)	0.00676 (1)	0.05659 (06)	4.16	0.02
13	150	0.70292 (02)	0.00671 (1)	0.05622 (06)	4.71	0.03
14	330	0.70283 (07)	0.00675 (2)	0.05649 (17)	1.51	0.01
15	330	0.70287 (04)	0.00677 (1)	0.05671 (07)	3.84	0.06
16	330	0.70300 (08)	0.00675 (2)	0.05655 (16)	1.55	0.06
17	330	0.70261 (03)	0.00678 (1)	0.05676 (07)	4.11	0.13
18	330	0.70263 (03)	0.00675 (1)	0.05691 (07)	3.87	0.04
19	330	0.70260 (04)	0.00680 (1)	0.05694 (08)	3.85	0.02
20	150	0.70281 (04)	0.00676 (1)	0.05664 (08)	4.23	0.02
21	330	0.70284 (04)	0.00675 (1)	0.05655 (08)	3.73	0.06
22	150	0.70289 (05)	0.00673 (1)	0.05634 (08)	3.09	0.09
23	150	0.70286 (03)	0.00675 (1)	0.05649 (08)	4.70	0.04
24	330	0.70283 (05)	0.00678 (1)	0.05676 (08)	3.44	0.07
25	150	0.70282 (04)	0.00675 (1)	0.05655 (08)	4.70	0.00
26	330	0.70269 (04)	0.00680 (1)	0.05697 (08)	3.28	0.12
27	330	0.70282 (04)	0.00670 (1)	0.05611 (08)	3.40	0.05

28	330	0.70277 (05)	0.00678 (1)	0.05680 (08)	3.34	0.08
29	150	0.70286 (03)	0.00677 (1)	0.05667 (08)	4.72	0.10
30	330	0.70253 (05)	0.00676 (1)	0.05663 (08)	3.84	0.05
31	150	0.70282 (03)	0.00679 (1)	0.05683 (08)	4.50	0.21
32	330	0.70275 (06)	0.00679 (1)	0.05689 (08)	3.44	0.10
33	330	0.70273 (06)	0.00679 (1)	0.05683 (08)	3.61	0.06
34	330	0.70254 (04)	0.00678 (1)	0.05678 (09)	4.22	0.23
35	330	0.70283 (04)	0.00676 (1)	0.05658 (09)	3.38	0.11
36	150	0.70276 (04)	0.00671 (1)	0.05623 (09)	2.70	0.10
37	330	0.70279 (04)	0.00679 (1)	0.05684 (09)	4.50	0.00
38	150	0.70286 (04)	0.00676 (1)	0.05661 (09)	4.66	0.07
39	330	0.70284 (04)	0.00680 (1)	0.05691 (10)	3.60	0.08
40	330	0.70285 (04)	0.00675 (1)	0.05655 (10)	4.64	0.04
41	330	0.70284 (08)	0.00680 (1)	0.05691 (10)	3.44	0.00
42	150	0.70265 (06)	0.00679 (1)	0.05685 (10)	2.51	0.00
43	330	0.70259 (04)	0.00674 (1)	0.05642 (10)	3.70	0.08
44	150	0.70281 (04)	0.00676 (3)	0.05658 (11)	8.77	0.30
45	150	0.70278 (05)	0.00678 (1)	0.05678 (11)	2.58	0.01
46	150	0.70280 (04)	0.00675 (1)	0.05656 (11)	2.52	0.00
47	330	0.70278 (02)	0.00676 (1)	0.05662 (11)	7.37	0.10
48	150	0.70282 (05)	0.00670 (1)	0.05613 (11)	2.50	0.87
49	330	0.70291 (05)	0.00673 (1)	0.05637 (11)	7.13	0.19
50	330	0.70289 (04)	0.00676 (1)	0.05662 (11)	7.39	0.23
51	150	0.70282 (04)	0.00675 (1)	0.05653 (12)	4.83	0.30
52	150	0.70276 (06)	0.00671 (2)	0.05622 (13)	2.31	0.08
53	150	0.70294 (05)	0.00672 (2)	0.05622 (13)	2.45	0.00
54	330	0.70285 (09)	0.00673 (8)	0.05634 (67)	0.45	0.03
55	100	0.70282 (05)	0.00679 (2)	0.05684 (14)	3.19	0.03
Fine-grained carbonates						
56	330	0.70289 (05)	0.00671 (1)	0.05623 (05)	**5.47**	0.02
57	330	0.70282 (04)	0.00677 (1)	0.05670 (05)	**5.83**	0.01
58	330	0.70290 (04)	0.00674 (1)	0.05645 (05)	**5.18**	0.04
59	330	0.70295 (04)	0.00676 (1)	0.05665 (07)	**5.41**	0.01
60	330	0.70288 (05)	0.00676 (1)	0.05660 (07)	**5.10**	0.01
	Averages	***0.70280 (22)***	***0.00676 (6)***	***0.05658 (49)***	***4.01***	***0.08***

Number in parentheses corresponds to analytical uncertainties in the last decimal place, and are quoted at the 2σ level.

Table 4. Sr isotopic ratios of coral standard determined by TIMS.

Sample number	$^{87}Sr/^{86}Sr$	2σ	$^{84}Sr/^{88}Sr$	$^{84}Sr/^{86}Sr$
1	0,709107	0,000020	0,006745	0,056489
2	0,709106	0,000017	0,006744	0,056471
3	0,709093	0,000014	0,006746	0,056495
4	0,709084	0,000016	0,006744	0,056478
Average	*0,709098*	*0,000020*	*0,006744*	*0,056483*

Table 5. Major element variation amongst single phlogopite crystals.

	Na_2O	F	K_2O	FeO	SiO_2	MgO	TiO2	CaO	MnO	Al_2O_3	Total
Phlogopite 1											
Core	0.41	0.48	10.41	9.06	41.13	24.63	0.32	0.06	0.05	9.81	96.35
Rim	0.15	0.82	10.17	14.66	40.33	22.34	0.18	0.35	0.08	7.28	96.34
Phlogopite 2											
Core	0.27	0.46	10.45	10.04	41.29	24.38	0.18	0.02	0.05	9.21	96.35
Rim	0.13	0.45	10.55	13.99	40.30	21.86	0.07	0.15	0.06	8.43	95.98
Rim	0.09	0.76	10.66	14.39	40.10	21.92	0.14	0.17	0.04	8.19	96.46
Rim	0.22	0.52	10.57	11.24	40.63	24.07	0.18	0.15	0.06	8.51	96.16
Phlogopite 3											
Core	0.30	0.48	10.02	10.64	40.97	24.31	0.24	0.21	0.04	8.73	95.92
Core	0.29	0.61	10.08	10.53	40.90	23.91	0.21	0.22	0.04	8.99	95.78
Rim	0.18	1.14	10.24	11.29	40.28	23.82	0.21	0.44	0.05	8.72	96.36
Rim	0.20	0.84	10.10	12.43	40.52	23.36	0.16	0.34	0.06	8.22	96.22

Analyses reported in weight %. Grains selected for analyses were small (<1 mm) inclusions found in carbonates associated with magnetite (e.g. Fig. 1a). Microprobe analyses were conducted under the same operating conditions as outlined in Table 1. Analytical uncertainties are outlined Table 1.

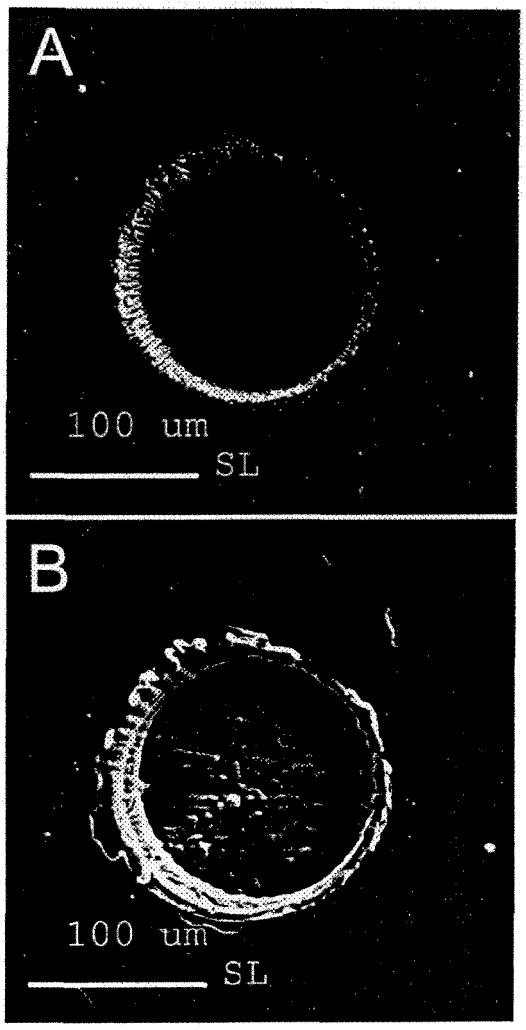

Figure 1. Scanning electron microscope images of laser-ablation pits. (a) 150μm pit in carbonate. (b) 150 μm pit in apatite. Laser ablation experiments were conducted in He atmosphere (0.450 L/min.), repetition rate of 1 to 2 Hz, and laser pulse energy of approximately 90 mJ (at 22 Kv) corresponding to energy densities of ~5 J/cm^2. Note the absence of accumulated ablated particles surrounding the pits.

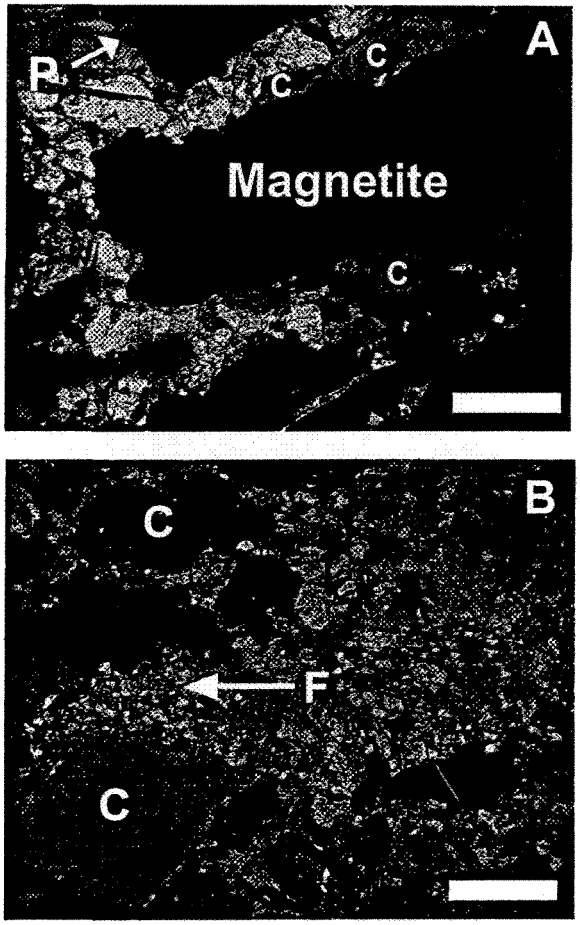

Figure 2. Microphotographs taken under polarized light of textural features observed in sample SARF-10. Scale bars represent 2 mm. (a) Coarse carbonate (C) crystals associated with magnetite. Phlogopite inclusions (P) are generally restricted to the carbonate crystals associated with the magnetite. (b) Coarse carbonate (C) crystals set in a finer carbonate (F) matrix.

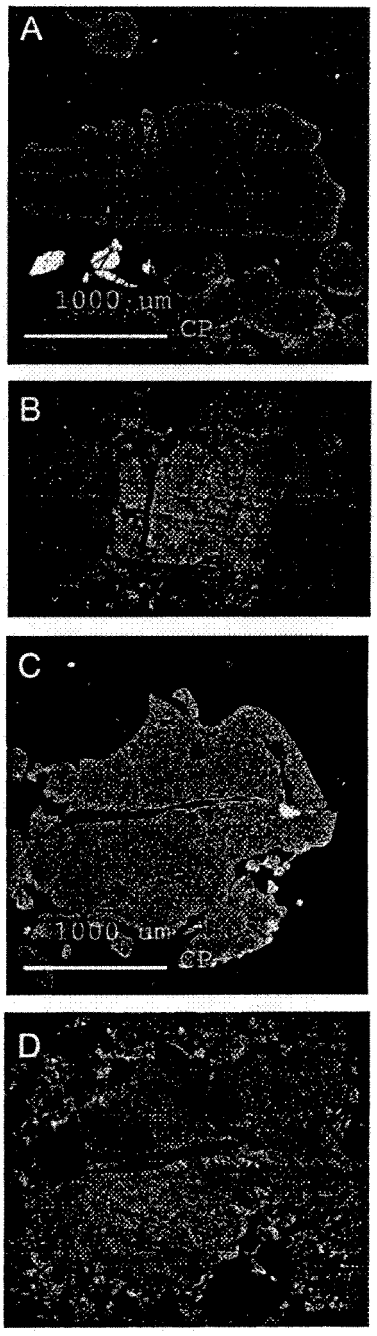

Figure 3. Backscattered electron images (a-c) and microphotographs taken under polarized light (b-d) of anhedral apatite crystals form sample SARF-10. Note embayment, resorbtion features, and lack of internal chemical zoning in both apatite grains.

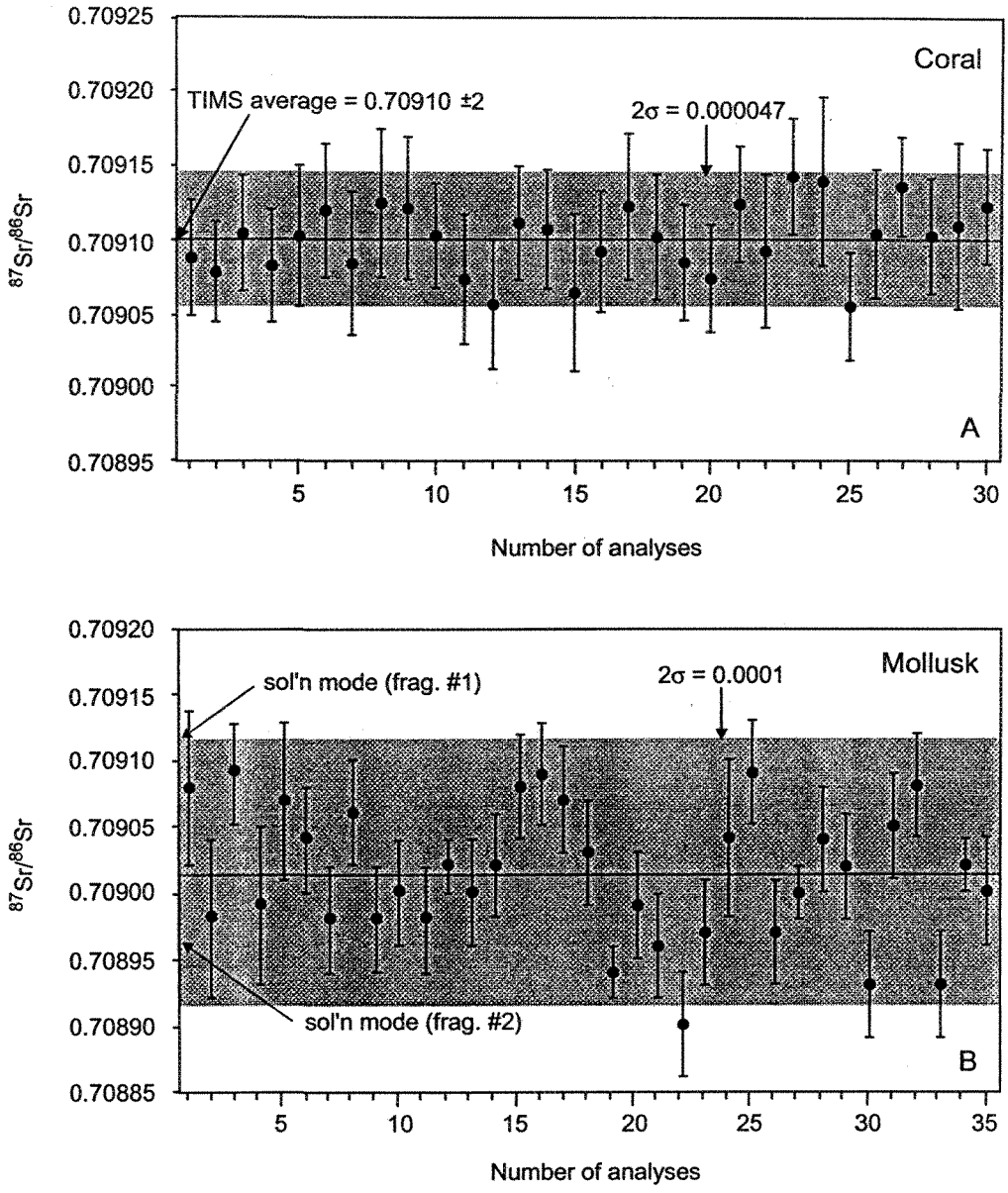

Figure 4. Individual $^{87}Sr/^{86}Sr$ isotope analyses for the 'in-house' coral (a) and mollusk (b) standards using laser ablation-MC-ICP-MS. The Sr isotopic compositions determined using solution mode MC-ICP-MS analysis for two separate mollusk fragments are also shown for comparison (b). Gray bands in both diagrams represent 2σ level external reproducibility.

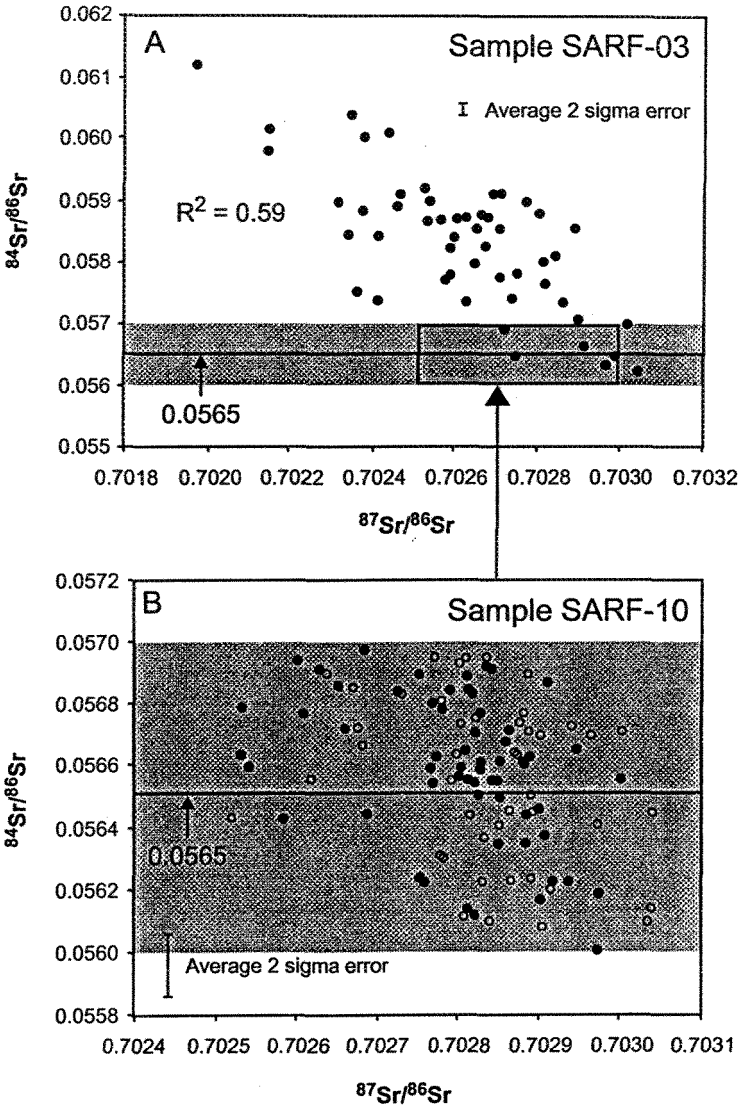

Figure 5. Correlation diagrams of $^{84}Sr/^{86}Sr$ vs. $^{87}Sr/^{86}Sr$. Solid circles = carbonate analyses; open circles = apatite analyses. The accepted $^{84}Sr/^{86}Sr$ value is 0.0565. (a) Sample SARF-03 displays a negative correlation between $^{87}Sr/^{86}Sr$ and $^{84}Sr/^{86}Sr$ values. Box outlines range for data obtained from sample SARF-10. (b) Sample SARF-10. Note lack of correlation for both apatites and carbonates crystals, and clustering of data around the accepted $^{84}Sr/^{86}Sr$ value of 0.0565.

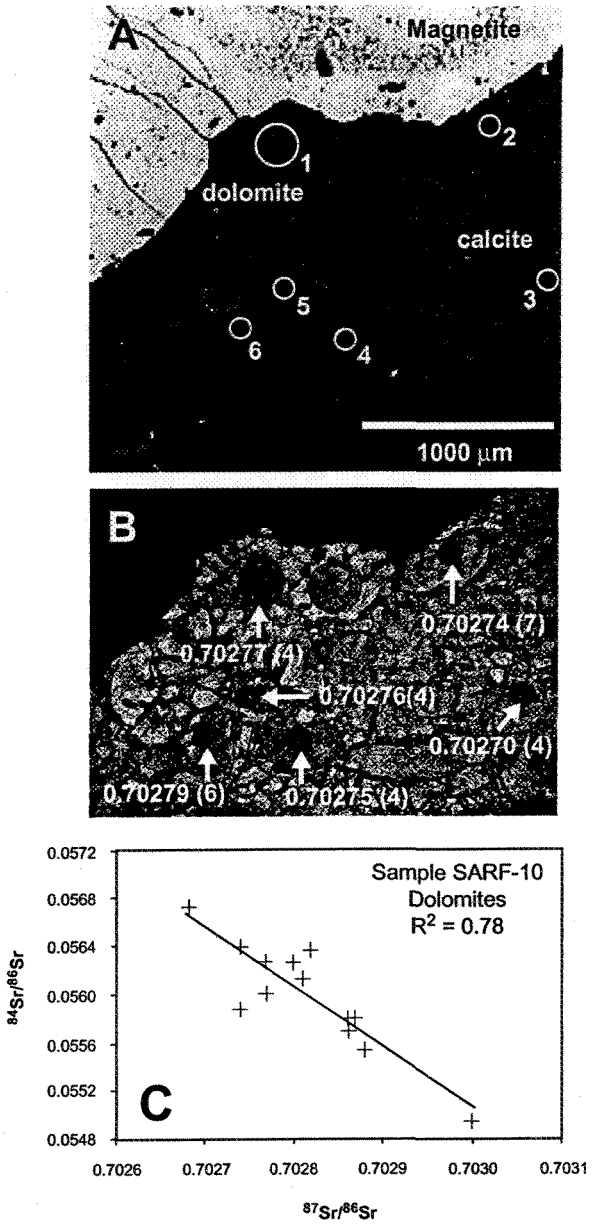

Figure 6. Backscattered electron image (a) and microphotographs taken under transmitted light (b) showing spatial relationships between dolomite, calcite, and magnetite crystals, and location of laser ablation pits with corresponding Sr isotopic composition. (c) Correlation diagram of $^{84}Sr/^{86}Sr$ vs. $^{87}Sr/^{86}Sr$ for dolomite grains shown in Fig. 6a. Pit sizes are 330 μm for #1 and 80 μm for # 2 to 6.

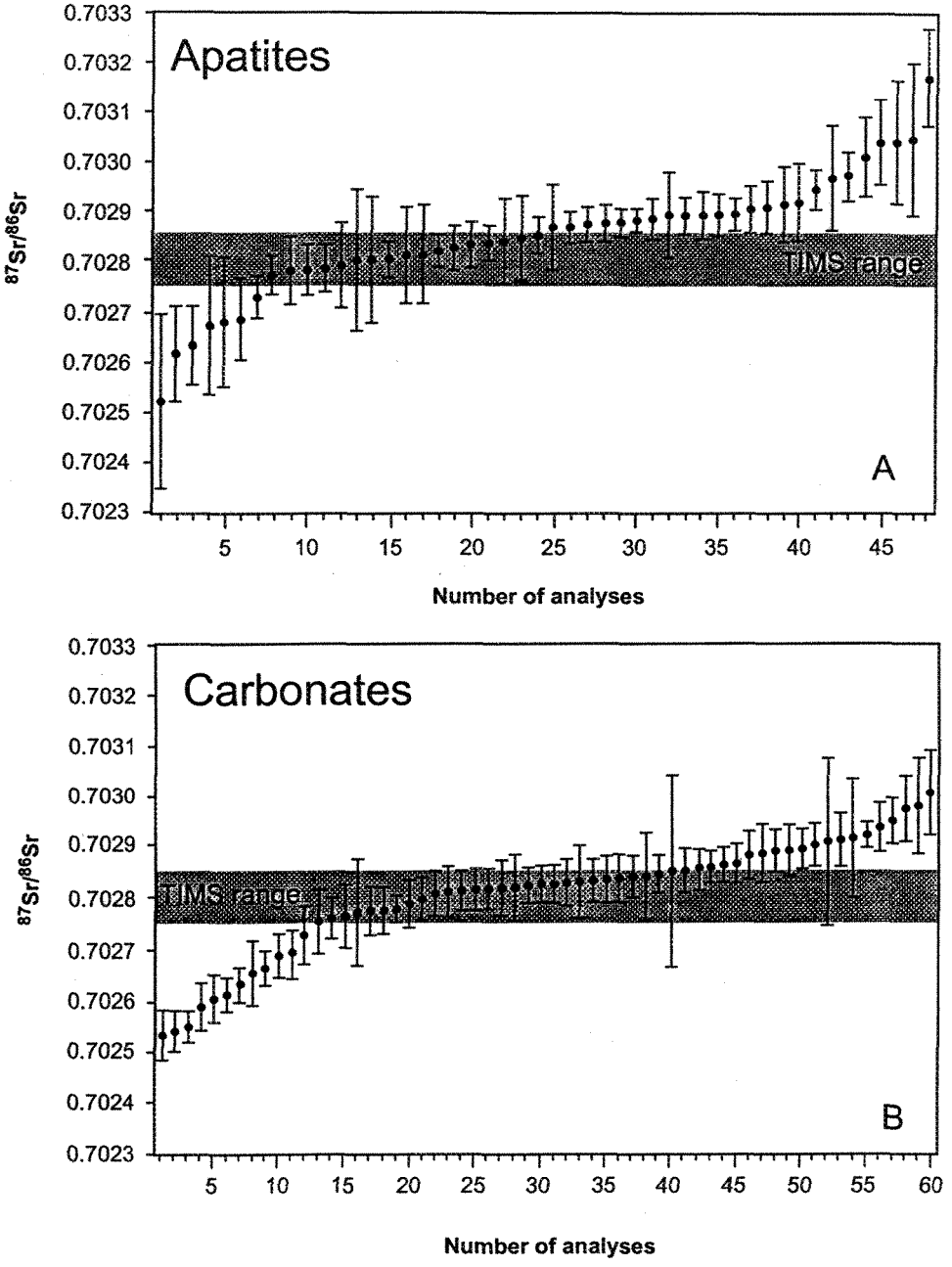

Figure 7. Diagram showing range of $^{87}Sr/^{86}Sr$ values obtained for apatites (a) and carbonates (b) from sample SARF-10. Gray area depicts range of $^{87}Sr/^{86}Sr$ values obtained for whole-rock TIMS analyses from sample SARF-10. Error bars represent uncertainties at 2σ level. Data are from Table 3.

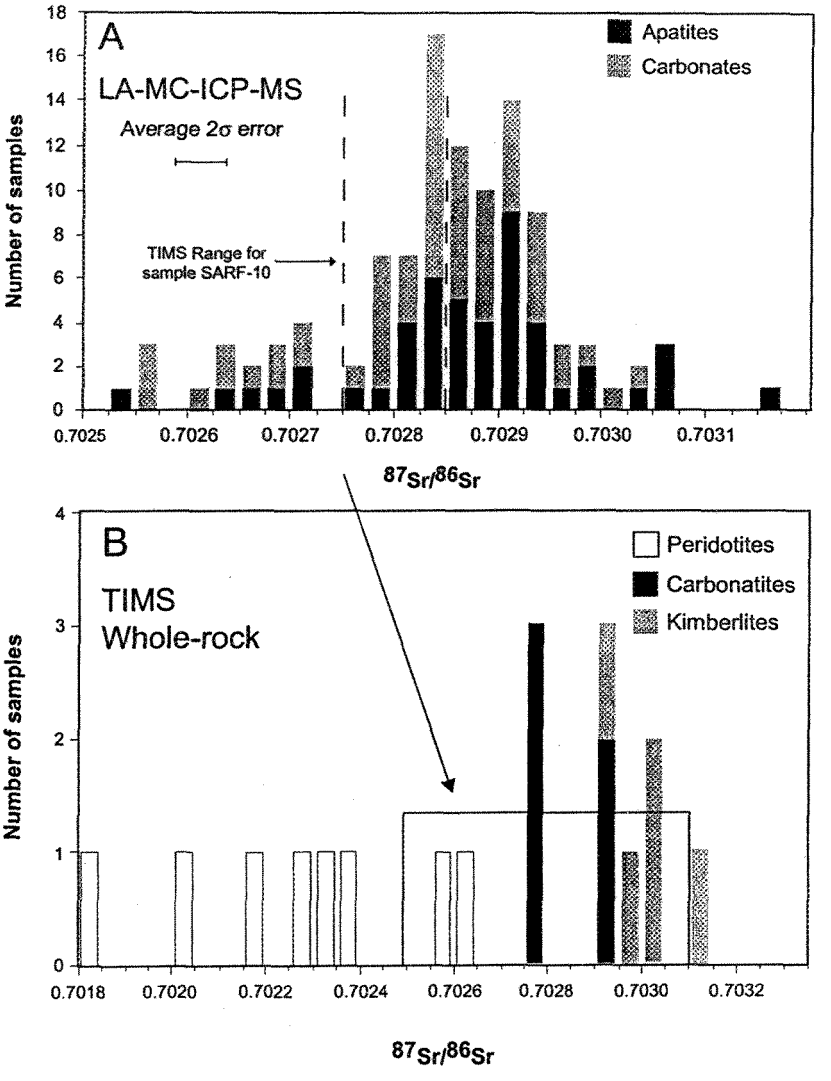

Figure 8. Histograms showing variations of Sr isotopic compositions for different rock-types and minerals of the Sarfartoq alkaline province of Greenland. (a) Range of $^{87}Sr/^{86}Sr$ values obtained by LA-MC-ICP-MS for apatites and carbonates from sample SARF-10. Data from Table 3. (b) Range of $^{87}Sr/^{86}Sr$ values obtained by TIMS for whole-rock analyses of kimberlites, carbonatites and kimberlite-hosted peridotites from Sarfartoq complex. Box represents range of values obtained by LA-MC-ICP-MS. TIMS data from Bizzarro and Stevenson (unpublished).

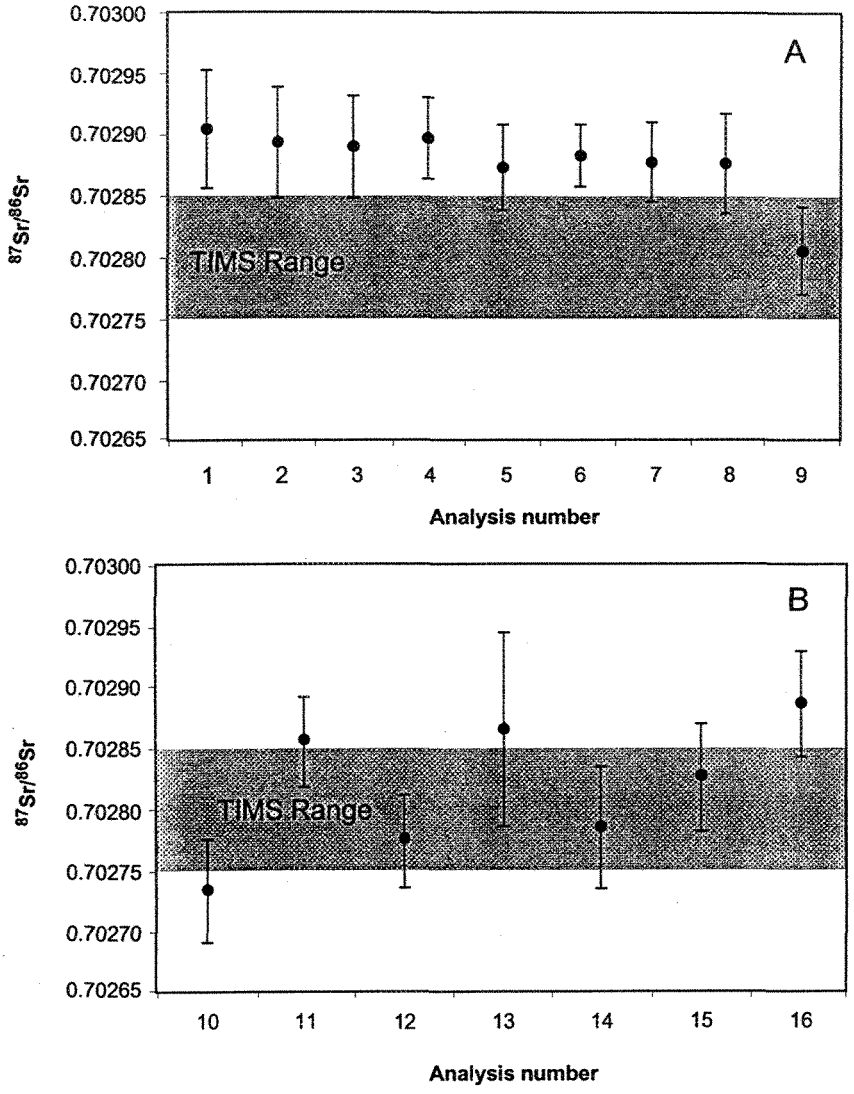

Figure 9. Diagrams showing intra-mineral variations of the $^{87}Sr/^{86}Sr$ composition in two different apatite crystals from sample SARF-10. Gray area depicts range of $^{87}Sr/^{86}Sr$ values obtained for whole-rock TIMS analyses from sample SARF-10. Error bars represent uncertainties at 2σ level. Analysis number corresponds to those listed in Table 3. (a) Measurements taken across a section perpendicular to the long axis of a euhedral grain. Section is 3.5 mm wide. (b) Measurements taken along the length of a 5.5 mm by 1.5 mm wide anhedral crystal.

Chapter III

Hf Isotope Evidence for a Hidden Mantle Reservoir

Martin Bizzarro, Antonio Simonetti, Ross K. Stevenson & Jean David

Centre GÉOTOP, Université du Québec à Montréal, succursale Centre-ville, CP 8888,

Montréal, Québec, Canada, H3C 3P8.

ABSTRACT

High-precision hafnium isotopic analyses and U-Pb ages of carbonatites and kimberlites from Greenland and eastern North America, including Earth's oldest known carbonatite (3 Ga), indicate derivation from an enriched mantle source. This previously unidentified mantle reservoir of unradiogenic Hf isotopic composition, preserved in the deep mantle for at least 3 billion years, may account for the mass imbalance in Earth's Hf-Nd budget. The Hf isotopic data presented here support a common mantle source region and genetic link between carbonatite and some oceanic island basalt (OIB) volcanoes.

3.1 INTRODUCTION

Recent Hf isotopic studies of Early Archean juvenile lithologies (Vervoort and Blichert-Toft, 1999; Amelin *et al.*, 2000) advocate for mantle depletion early in Earth's history (>3.7 Ga). This depletion may have resulted via the extraction of sialic (Bowring and Housh, 1995), or large-ion-lithophile-element (LILE)-enriched mafic crust (Chase and Patchett, 1988; Vervoort and Blichert-Toft, 1999). The paucity of unradiogenic Hf isotopic signatures in juvenile Early Archean rocks, indicative of derivation from an enriched mantle source, suggests that this crust was rapidly recycled back into the mantle and isolated from convective stirring. Isolation of recycled material may be achieved at deep mantle levels, such as the 660-km seismic discontinuity or the core-mantle boundary (CMB). Recycling at the 660-km discontinuity implies a layered convective regime for the Earth's mantle, which is not supported by geophysical evidence (Van der Hilst *et al.*, 1997), thus leaving the CMB region as the most likely possibility of the two. As discussed elsewhere (Albarède *et al.*, 2000), the exact chemical and physical nature of the bottom 1000 km of the mantle is unknown. The presence of strong seismic heterogeneity in this region of the mantle is consistent with the existence of compositionally distinct domains, possibly isolated from convective stirring (Tackley, 2000). Sampling of these deep mantle domains may occur via the production of vertically oscillating domes with narrow tubular plumes arising from their upper surfaces, as modeled by thermochemical convection experiments (Davaille, 1999). For Earth's mantle, this process occurs at low density contrasts (<1%), and provides a mechanism by which deep (recycled?) material may be involved in surface volcanic processes. Recycled material in the source region of recent oceanic volcanism, in particular for HIMU-basalts (generated from mantle source with high

μ-$^{238}U/^{206}Pb$ ratios), has been argued based on Pb (White and Hofmann, 1982) and Hf isotopes (Salters and White, 1998; Blichert-Toft *et al.*, 1999). One commonly held view is that HIMU-type basalts are derived from a boundary region where subducted oceanic lithosphere has accumulated (e.g. Hofmann, 1997, Bell and Tilton, 2001). It has been proposed that the HIMU mantle component may be stored at the CMB (Hart, 1988), and recent tomographic results indicate major upwelling from this region in at least two places (Van der Hilst et al., 1997). These are the southeast Pacific Ocean and the East African Rift zone, the latter containing an overwhelming number of kimberlite and carbonatite complexes (Woolley, 1989). Furthermore, Nd, Pb, and Sr isotope data from carbonatites world-wide (in particular those <200 Ma old) indicate similarities to OIBs as previously proposed by other workers (e.g. Nelson et al., 1988), and suggest mantle mixing involving the HIMU component (Tilton and Bell, 1994). To-date, the Hf isotopic systematics of carbonatites and kimberlites, and their kinship to HIMU basalts, has yet to be thoroughly investigated. To this effect, we report on the Hf, Nd and U-Pb isotope systematics of carbonatites and kimberlites from Eastern North America and Greenland in order to constrain their mantle source regions. The carbonatites at Qaqarssuk, Sarfartoq, and Tupertalik of southwestern Greenland (Larsen and Rex, 1992), and kimberlites from the Guigues pipe of Eastern Canada (Heaman and Kjarsgaard, 2000) and Sarfartoq (Larsen and Rex, 1992) were intruded over a period of >2.6 Ga (see Table 1). This provides an unparalleled opportunity to investigate the chemical evolution of their source regions.

3.2 RESULTS

Table 1 lists the results for U-Pb age determinations using isotope dilution thermal ionization mass spectrometry (ID-TIMS) and Hf isotopic composition by multi-collection,

inductively coupled plasma-source mass spectrometry (MC-ICP-MS; IsoProbe from Micromass) for baddeleyite (ZrO_2) and zircon ($ZrSiO_4$) from carbonatite and whole rock kimberlite (hypabyssal facies) from Greenland and Canada. U, Pb, and Hf isotopic compositions were determined on the same baddeleyite/zircon grain or mineral fraction for both solution and laser ablation modes. Additional data tables are available in the GSA Data repository.

The U-Pb data obtained for 7 baddeleyite fractions yield the precise Concordia age of 3007 ± 2 Ma (Fig. 1), which renders Tupertalik as Earth's oldest known carbonatite. This age is approximately 300 million years older than any other carbonatite occurrence documented to-date (Woolley, 1989). Only grains exhibiting concordant U-Pb ages (i.e. closed system behaviour) were selected for Hf isotope analyses. Of importance, the occurrence of baddeleyite is restricted to mafic and alkaline magmas (Heaman and LeCheminant, 1993), and not likely inherited from the surrounding felsic crustal lithologies. The $^{176}Lu/^{177}Hf$ values for ten zircons and ten baddeleyites from the Tupertalik carbonatite and for seven zircons from Sarfartoq, determined by laser ablation MC-ICP-MS, range from 0 to 0.00002 and 0.0001 to 0.0004, respectively; this results in a maximum (downward) age correction on the $^{176}Hf/^{177}Hf$ value of <20 ppm for Sarfartoq and <5 ppm for Tupertalik. These corrections are considered negligible since they are well within the internal precision of individual analyses (Table 1) and the (2σ) external reproducibility (100 ppm). As such, present-day Hf isotopic compositions of baddeleyites and zircons were considered initial values for all carbonatite complexes.

Hf isotopic results are presented in an ε_{Hf} (ε_{Hf} is a deviation of the $^{176}Hf/^{177}Hf$ ratio from the chondritic reference value, multiplied by 10^4) vs. age diagram (Fig. 2). The three kimberlite samples analyzed are characterized by Hf isotopic compositions intermediate between depleted mantle (DM) and unradiogenic values (ε_{Hf} <0), similar to kimberlites from South Africa (Nowell *et al.*, 1999). Zircon and baddeleyite from carbonatites have isotopic compositions extending towards unradiogenic values except for the Sarfartoq zircons, showing signatures intermediate to BSE (bulk silicate earth) and DM. Unradiogenic Hf isotopic signatures (ε_{Hf} ~ -10) have also been reported for concordant baddeleyites from the 2059 Ma Palaborwa carbonatite, South Africa (Fig. 2; Scherer *et al.*, 2001). The ε_{Hf} compositions of baddeleyite and zircon from the Tupertalik carbonatite exhibit a good correlation with the $^{206}Pb/^{238}U$ ratio (Fig. 1), such that the most concordant grains (high $^{206}Pb/^{238}U$) show negative ε_{Hf} values. In addition, the U content is not correlated to either the Hf isotopic composition or the $^{206}Pb/^{238}U$ value of the grains analyzed. This indicates that the negative ε_{Hf} component is not the result of a post-crystallization metamorphic disturbance, but most probably represents the true isotopic signature of the melt. A combined U-Pb and Hf laser ablation (LA) MC-ICP-MS study was undertaken on zircons from the Tupertlik and Sarfartoq carbonatites. Zircons for which a concordant U-Pb age was determined by LA-MC-ICP-MS yielded a range of Hf isotopic compositions comparable to that established in solution mode (Fig. 2).

3.3 DISCUSSION

The estimated compositions for the mantle sources of both <600 Ma kimberlites and carbonatites and the 3 Ga Tupertalik carbonatite are distinct from the mantle sources

sampled by modern oceanic basalts, as the data fall below the array formed by MORBs and OIBs. Such a decoupling, also noted for HIMU basalts from St. Helena (Salters and White, 1998), indicates derivation from a reservoir with sub-chondritic Lu/Hf and super-chondritic Sm/Nd ratios. This decoupling can be achieved during partial melting in a mid-oceanic ridge setting, since modern MORBs are characterized by sub-chondritic Lu/Hf and super-chondritic Sm/Nd ratios. Long-term storage of such a mafic component would generate a mantle reservoir with time-integrated un-radiogenic and radiogenic Hf and Nd isotopic compositions, respectively. Thus, the Sm/Nd and Lu/Hf fractionation trends observed in Fig. 3 indicate that the source region for the 3 Ga Tupertalik carbonatite and younger carbonatites, kimberlites and modern HIMU basalts, may contain a recycled mafic crustal component. The variation in Hf isotopic compositions recorded by zircon and baddeleyite crystals (Figs. 2 and 3) also suggest open-system behaviour involving distinct mantle reservoirs during carbonatite formation, such as plume and subcontinental lithosphere (e.g. Bell and Simonetti, 1996; Simonetti *et al.*, 1998). Another striking feature of Fig. 3 is that the Early to mid-Archean terrestrial mantle was isotopically much more heterogeneous (in particular for Lu/Hf) than the present-day mantle sampled by MORBs and OIBs. As discussed in Albarède *et al.* (2000), the isotopic heterogeneity observed in the early terrestrial mantle exhibits similarities to the poorly mixed mantles of planetary bodies such as Mars and the Moon, and may represent a transient regime inherited from initial planetary differentiation. Our study thus confirms that such isotopic heterogeneity was still present as late as around 3 Ga, but more elusive in <2.7 Ga mantle-derived rocks.

The Hf-Nd isotope systematics of modern basalts and chondrites requires an additional reservoir complementary to depleted mantle and continental crust in order to

account for the accepted Hf-Nd composition of BSE (Blichert-Toft and Albarède, 1997). This missing component may consist of recycled basalts representing old oceanic crust and plateaus (Chase and Patchett, 1988; Blichert-Toft and Albarède, 1997). Assuming that this reservoir equates to the carbonatite-kimberlite source region, and formed approximately 4 Ga ago (Fig. 2), a $^{176}Lu/^{177}Hf$ ~0.027 is required to generate the least radiogenic Hf composition observed at 3 Ga (i.e. 19% fractionation from the BSE value of 0.0332; Blichert-Toft and Albarède, 1997). Formation of the carbonatite and kimberlite source reservoir around 4 Ga is consistent with other estimates of timing of mantle differentiation (Vervoort and Blichert-Toft, 1999). Using this constraint and accepted abundances of Lu, Hf, Sm, and Nd for Earth's major geochemical reservoirs (McDonough and Sun, 1995; Rudnick and Fountain, 1995) mass balance calculations indicate that the unradiogenic Hf component may account for 10-15% of the total mass of silicate Earth. For depleted mantle, Hf (0.15 ppm), Lu (0.01 ppm), Nd (1 ppm), and Sm (0.2 ppm) contents were derived using batch melting equations (Albarède, 1995), partition coefficients from Hart and Dunn (1993), and assuming 10-15% garnet-absent melting in order to yield average compositions of MORBs (McDonough and Sun, 1995). These abundances are consistent with Lu/Hf and Sm/Nd ratios accepted for depleted mantle based on Hf and Nd isotope compositions (Vervoort and Blichert-Toft, 1999). This approach results in Hf, Lu, Nd, and Sm concentrations of approximately 1, 0.2, 1.5, and 0.4 ppm, respectively in the missing mantle reservoir, which represents ~10-15% of BSE as compared to ~85-90% for depleted mantle and 0.6% for continental crust. Obviously, these concentrations are approximations since they are highly sensitive to model parameters such as partition coefficients and degree of partial melting. This calculation assumes a present-day $\varepsilon Hf \sim -17$ for the enriched

component, and the absence of any primitive-mantle–like reservoir since the Hf-Nd isotope geochemistry of terrestrial basalts is inconsistent with derivation from such a component (Blichert-Toft and Albarède, 1997). The proposed model results in a present-day $^{176}Hf/^{177}Hf$ value of 0.28279 for BSE, which differs by ~75 ppm to the accepted value of 0.282772 (Blichert-Toft and Albarède, 1997). These two values, determined independently, are identical considering the uncertainties associated with both the isotopic compositions for the BSE model (Blichert-Toft and Albarède, 1997) and our calculated value (50 and 100 ppm, respectively).

Our data indicate the existence in the source region of kimberlite and carbonatite magmas, since at least 3 Ga, of a negative ε_{Hf} component that is decoupled from the Nd isotope systematics and divergent from either depleted- or primitive-mantle compositions. The carbonatite and kimberlite mantle source is distinct from that which generated the Archean komatiites since these have sampled a depleted mantle source at approximately 3 Ga (Fig. 2). In addition, Sr and Pb isotopic data from North American carbonatites (ranging from 0.1 to 2.7 Ga) indicate derivation from a source region distinct from either primitive or MORB-like depleted mantle (Bell *et al.*, 1982; Tilton and Bell, 1994). Alternatively, the negative ε_{Hf} component may also reside in the subcontinental mantle (Griffin *et al.*, 2000). New Hf isotopic data for constituent minerals from kimberlite-hosted garnet peridotite xenoliths from the Canadian Arctic (Schmidberger *et al.*, 2002) refutes this interpretation since these analyses systematically yield positive ε_{Hf} signatures. Our preferred interpretation is that carbonatite/kimberlite melts are derived from an unradiogenic Hf mantle source that is at least 3 Ga old. Isolation of this mantle source may have occurred in

the deep mantle (CMB region?), and may consist of recycled, fertile lithosphere related to an Early Archean mantle depletion event (e.g. Chase and Patchett, 1988). A similar model is presented for the generation of South African group I and II kimberlites, which involves plumes originating from a deep mantle source characterized by a negative ε_{Hf} signature (Nowell *et al.*, 1999). Bell and Tilton (2001) have also recently proposed carbonatite generation via plumes originating from the deep mantle (the bottom 1000 km of the mantle) involving the HIMU and EM1 (enriched-mantle 1) mantle components, which corroborates the model being presented here.

ACKNOWLEDGEMENTS

Supported by a Natural Sciences and Engineering Research Council of Canada grant (to Stevenson), and a Graduate Research Grant from the Geological Society of America (to Bizzarro). Bizzaro acknowledges *Fonds de recherche sur la nature et les technologies* for a Ph.D. scholarship. Francis Albarède and Clément Gariépy informally reviewed an earlier version of this manuscript. Constructive reviews from J. Blichert-Toft, J. Patchett and K. Bell improved the quality of this manuscript.

REFERENCES

Albarède, F., 1995, Introduction to Geochemical Modeling, Cambridge University Press, Cambridge, pp. 543.

Albarède, F., Blichert-Toft, J., Vervoort, J.D., Gleason, J. G., Rosing, M., 2000, Hf-Nd evidence for a transient dynamic regime in early terrestrial mantle: Nature, v. 404, p. 488-490.

Amelin, Y., Lee, D.-C., Halliday, A.N., 2000, Early-middle Archaean crustal evolution deduced from Lu-Hf and U-Pb isotopic studies of single grain zircons: Geochimica et Cosmochimica Acta, v. 64, p. 4205-4225.

Bell, K., Blenkinsop, J., Cole, T. J. S., Menagh, D. P., 1982, Evidence from Sr isotopes for long-lived heterogeneities in the upper mantle: Nature, v. 298, p. 251-253.

Bell, K., Simonetti, A., 1996, Carbonatite magmatism and plume activity: implications from the Nd, Pb and Sr isotope systematics of Oldoinyo Lengai: Journal of Petrology, v. 37, p. 1321-1339.

Bell, K., Tilton, G.R., 2001, Nd, Pb and Sr isotopic compositions of East African carbonatites: Evidence for mantle mixing and plume inhomogeneity: Journal of Petrology, v. 42, p. 1927-1945.

Blichert-Toft, J., Albarède, F., 1997, The Lu-Hf isotope geochemistry of chondrites and the evolution of the mantle-crust system: Earth and Planetary Science Letters, v. 148, p. 243-258.

Blichert-Toft, J., Chauvel, C., Albarède, F., 1997, Separation of Hf and Lu for high-precision isotope analysis of rock samples by magnetic sector-multiple collector ICP-MS: Contributions to Mineralogy and Petrology, v. 127, p. 248-260.

Blichert-Toft, J., Arndt, N.T., 1999, Hf isotope compositions of komatiites: Earth and Planetary Science Letters, v. 171, p. 439-451.

Blichert-Toft, J., Frey, F.A., Albarède, F., 1999, Hf isotope evidence for pelagic sediments in the source of Hawaiian basalts: Science, v. 285, p. 879-882.

Bowring, S.A., Housh, T., 1995, The Earth's early evolution: Science, v. 269, 1535-1540.

Chase, C.G., Patchett, P.J., 1988, Stored mafic/ultramafic crust and early Archean mantle depletion: Earth and Planetary Science Letters, v. 91, p. 66-72.

Chauvel, C., Blichert-Toft, J., 2001, A hafnium isotope and trace element perspective on melting of the depleted mantle: Earth and Planetary Science Letters, v. 190, p. 137-151.

Davaille, A., 1999, Simultaneous generation of hotspots and superswells by convection in a heterogeneous planetary mantle: Nature, v. 402, p. 756-760.

Griffin, W.L., Pearson, N.J., Belousova, E., Jackson, S.E., van Achterbergh, E., O'Reilly, S.Y., Shee, S.R., 2000, The Hf isotope composition of cratonic mantle: LAM-MC-ICPMS analysis of zircon megacrysts in kimberlites: Geochimica et Cosmochimica Acta, v. 64, p. 133-147.

Hart, S.R., 1988, Heterogeneous mantle domains: signature, genesis and mixing chronologies: Earth and Planetary Science Letters, v. 90, p. 273-296.

Hart, S.R., Dunn, T., 1993, Experimental clinopyroxene-melt partitioning of 24 trace elements: Contribution to Mineralogy and Petrology, v. 113, p. 1-8.

Heaman, L.M., LeCheminant, A.N., 1993, Paragenesis and U-Pb systematics of baddeleyite (ZrO_2): Chemical Geology, v. 110, p. 95-126.

Heaman, L.M., Kjarsgaard, B., 2000, Timing of eastern North American kimberlite magmatism: continental extension of the Great Meteor hotspot track?: Earth and Planetary Science Letters, v. 178, p. 253-268.

Henry, P., Stevenson, R.K., Gariépy, C., 1998, Late Archean mantle composition and crustal growth: Geochimica et Cosmochimica Acta, v. 62, p. 143-157.

Hofmann, A., 1997, Mantle geochemistry: The message from oceanic volcanism: Nature, v. 385, 219-229.

Jacobsen, S.B., Wasserburg, G.J., 1980, Sm-Nd isotopic evolution of chondrites, Earth and Planetary Science Letters, v. 50, p. 139-155.

Larsen, L.M., Rex, D.C., 1992, A review of the 2500 Ma span of alkaline-ultramafic, potassic and carconatitic magmatism in west Greenland: Lithos, v. 28, 367-402.

Machado, N., Simonetti, A., 2001, U-Pb dating and Hf isotopic composition of zircon by laser-ablation MC-ICP-MS, *In* P. Sylvester, Ed., Laser-Ablation-ICPMS in the Earth Sciences: Principles and Applications, St.John's, Newfoundland, Mineralogical Association of Canada, pp. 121-146.

McDonough, W.F., Sun, S.-S., 1995, The composition of the Earth: Chemical Geology, v. 120, p. 223-253.

Nelson, D.R., Chivas, A.R., Chappell, B.W., McCulloch, M. T., 1988, Geochemical and isotopic systematics in carbonatites and implication for the evolution of ocean-island sources: Geochimica et Cosmochimica Acta, v. 52, p. 1-17.

Nowell, G.M., Pearson, D.G., Kempton, P.D., Noble, S.R., Smith, C.B., 1999, The origins of kimberlites: A Hf isotope perspective: *In* J.J.,Gurney, J.L., Gurney, M.D. Pascoe and S.H. Richardson., eds., Proceedings of the VIIth International Kimberlite Conference, v. 2, Cape town, Red Roof Design, p. 616-624.

Nyquist, L.E., Shih, C.-Y., 1992, The isotopic record of lunar volcanism: Geochimica et Cosmochimica Acta, v. 62, p. 525-544.

Rudnick, R.L., Fountain, D.M., 1995, Nature and composition of the continental crust: a lower crustal perspective: Reviews of Geophysics, v. 33, p. 267-309.

Salters, V.J.M., White, W.M., 1998, Hf isotope constraints on mantle evolution: Chemical Geology, v. 145, p. 447-460.

Scherer, E., Münker, C., Mezger, K., 2001, Calibrating the Lu-Hf clock: Science, v. 293, p. 683-686.

Schmidberger S.S., Simonetti A., Francis, D., Gariépy, C., 2002, Probing Archean lithosphere using the Lu-Hf isotope systematics of peridotite xenoliths from Somerset Island kimberlites, Canada: Earth and Planetary Science Letters, v. 197, p. 245-259.

Simonetti A., Goldstein S.L., Schmidberger S.S., Viladkar S.G., 1998, Geochemical and Nd, Pb, and Sr isotope data from Deccan alkaline complexes-inferences for mantle sources and plume-lithosphere interaction: Journal of Petrology v. 39, p. 1847-1864.

Tackley, P.J., 2000, Mantle convection and plate tectonics: Towards an integrated physical and chemical theory: Science, v. 288, p. 2002-2007.

Tilton, G.R., Bell, K., 1994, Sr-Nd-Pb isotope relationships in late Archean carbonatites and alkaline complexes: Applications to the geochemical evolution of the mantle: Geochimica et Cosmochimica Acta, v. 58, p. 3145-3154.

Van der Hilst, R.D., Widiyantoro, S., Engdahl, E.R., 1997, Evidence for deep mantle circulation from global tomography: Nature, v. 386, p. 578-583.

Vervoort, J., Blichert-Toft, J., 1999, Evolution of the depleted mantle: Hf isotope evidence from juvenile rocks through time: Geochimica et Cosmochimica Acta, v. 63, p. 533-556.

White, W.M, Hofmann, A.W., 1982, Sr and Nd isotope geochemistry of oceanic basalts and mantle evolution: Nature v. 296, p. 821-825.

Woolley, A.R., 1989, Spatial and Temporal Distribution of Carbonatites: *in* Carbonatites: Genesis and Evolution, K. Bell, Ed., Unwin Hyman, London, pp. 15-37.

TABLE 1. Hf, Nd and U-Pb DATA

	No	* $^{176}Hf/^{177}Hf_{(0)}$	$\varepsilon_{Hf(t)}$	$^{206}Pb/^{238}U$	$^{207}Pb/^{235}U$	U-Pb age †	$\varepsilon_{Nd(t)}$
Solution mode							
Carbonatites							
Qaqarssuk	2z	0.282519 (48)	−5.11	0.0246	0.17	157	4.45
Qaqarssuk	3z	0.282637 (19)	−0.94	0.026	0.1432	165	
Qaqarssuk	4z	0.282656 (19)	−0.26	0.0263	0.1498	167	
Qaqarssuk	5z	0.282745 (06)	2.88	0.0261	0.1691	166	
Qaqarssuk	6z	0.282770 (08)	3.77	0.0263	0.1812	167	
Sarfartoq	1z	0.282493 (07)	3.35	0.0702	0.5808	604	
Sarfartoq	2z	0.282438 (07)	1.4	0.077	0.6422	621	4.21
Sarfartoq	3z	0.282520 (31)	4.31	0.0888	0.7302	590	
Sarfartoq	4z	0.282581 (27)	6.47	0.0834	0.6897	603	
Sarfartoq	6z	0.282621 (19)	7.88	0.0903	0.7441	595	
Sarfartoq	7z	0.282490 (08)	3.24	0.0937	0.7719	594	
Sarfartoq	8z	0.282476 (08)	2.75	0.0921	0.7548	584	
Tupertalik	3b	0.280788 (52)	−2.45	0.5883	18.103	3004	2.88
Tupertalik	5b	0.280742 (08)	−4.09	0.5955	18.378	3009	
Tupertalik	7b	0.280802 (10)	−1.96	0.583	17.948	3005	
Tupertalik	8b	0.280870 (11)	0.47	0.5941	18.312	3007	
Tupertalik	1z	0.280805 (12)	−1.85	0.5888	18.069	2999	
Tupertalik	2z	0.280780 (08)	−2.74	0.5847	17.778	2985	
Tupertalik	4z	0.280760 (08)	−3.45	0.5921	18.22	3004	
Tupertalik	5z	0.280846 (15)	−0.39	0.5834	17.633	2975	
Tupertalik	6z	0.280882 (12)	0.89	0.5778	17.766	3003	
Kimberlites							
Guigues	G-3	0.282636 (22)	−1.92	N.D.#	N.D.	N.D.	5.23
Sarfartoq	S-1	0.282467 (14)	2.43	N.D.	N.D.	N.D.	2.98
Sarfartoq	S-2	0.282462 (10)	2.25	N.D.	N.D.	N.D.	3.01
Laser ablation							
Carbonatites							
Sarfartoq	101z	0.282430 (23)	1.12	0.0926	0.7814	609	4.21
Sarfartoq	102z	0.282527 (25)	4.55	0.0898	0.7448	610	
Sarfartoq	105z	0.282533 (25)	4.77	0.0951	0.8075	690	
Sarfartoq	106z	0.282409 (23)	0.38	0.0935	0.7626	598	
Sarfartoq	106z	0.282422 (22)	0.84	N.D.	N.D.	N.D.	
Sarfartoq	122z	0.282543 (32)	5.12	0.0955	0.8019	612	
Sarfartoq	133z	0.282492 (29)	3.31	0.0994	0.8495	706	
Tupertalik	101z	0.280856 (30)	−0.03	0.5991	18.2079	2992	2.88
Tupertalik	102z	0.280824 (22)	−1.17	N.D.	N.D.	N.D.	
Tupertalik	103z	0.280846 (29)	−0.39	0.6007	18.7191	2990	
Tupertalik	105z	0.280812 (24)	−1.6	0.6257	19.829	2983	
Tupertalik	106z	0.280769 (30)	−3.13	N.D.	N.D.	N.D.	
Tupertalik	107z	0.280870 (27)	0.47	0.5988	17.9693	2977	
Tupertalik	109z	0.280829 (22)	−0.99	0.6656	20.4002	2952	
Tupertalik	109z	0.280827 (29)	−1.07	N.D.	N.D.	N.D.	
Tupertalik	110z	0.280800 (29)	−2.03	0.6037	18.6924	2999	
Tupertalik	111z	0.280812 (30)	−1.6	0.6019	18.2484	2992	

Note: εHf(t) and εNd(t) values were calculated using planetary reference values of Blichert-Toft and Albarède (1997) and Jacobsen and Wasserburg (1980), respectively, and the Lu decay constant (λ) of 1.865×10^{-11} years^{-1} (Scherer *et al.*, 2001). εHf(t) values were

calculated using ages of 175 Ma and 600 Ma for the Guigues and Safartoq kimberlites, respectively. Chemical separation for Lu and Hf is after Blichert-Toft *et al.* (1997) and Amelin *et al.* (2000). Procedural blanks of <50 pg for Hf are considered negligible. Measured ratios were corrected for mass fractionation to $^{179}Hf/^{177}Hf = 0.7325$; spiked samples were corrected by iteratively solving a non-linear equation combining the exponential fractionation law and the spike-natural mixing equation (Blichert-Toft *et al.*, 1997). $^{176}Lu/^{177}Hf$ ratios of the G-3, S- 1 and S-2 kimberlites are 0.008, 0.002 and 0.001, respectively, (error of ≤2%). Repeated analysis (n=20) of the JMC Hf standard yielded $^{176}Hf/^{177}Hf=0.28216\pm3$, $^{178}Hf/^{177}Hf=1.46726\pm15$, and $^{180}Hf/177^{Hf}=1.88667\pm26$ (2σ, standard deviation). Average $^{178}Hf/^{177}Hf$ and $^{180}Hf/^{177}Hf$ ratios for both solution and laser ablation runs are 1.46724±14, 1.88667±27 (2σ, n=20), and 1.46731±13, 1.88669±32 (2σ, n=17), respectively. U-Pb and Hf laser ablation protocols outlined in Machado and Simonetti (2001). Chemical procedures and isotopic analyses for Nd are after Henry *et al.* (1998).

*b=baddeleyite, z=zircon.

†Reported U-Pb ages (Ma) calculated using the $^{207}Pb/^{206}Pb$ value (Tupertalik and Sarfartoq carbonatites), and the $^{206}Pb/^{238}U$ result for Qaqarssuk.

#Not determined.

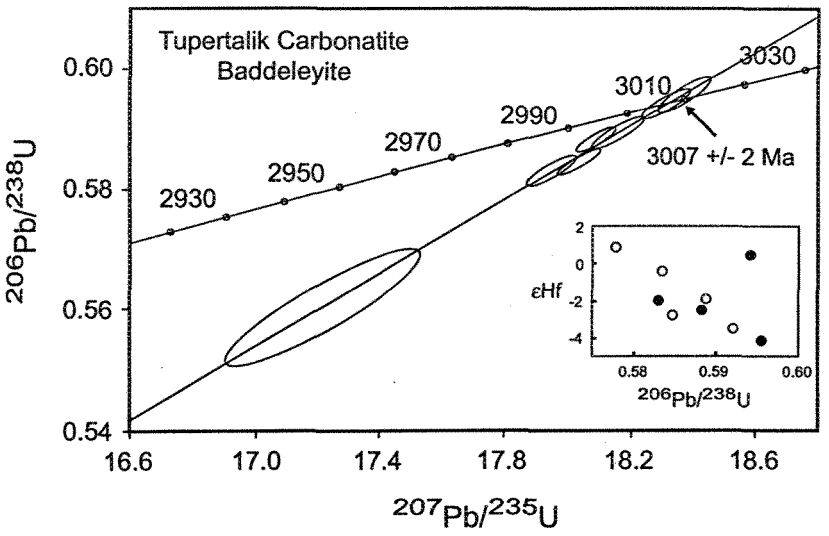

Figure 1. U-Pb Concordia diagram for single baddeleyite grains from the Tupertalik carbonatite. Error ellipses are 1σ and age uncertainty is quoted at the 2σ level. U-Pb analyses followed isotope dilution methods outlined in Heaman and Kjarsgaard (2000) and Amelin *et al.* (2000). The relaltionship between ε_{Hf} and $^{206}Pb/^{238}U$ for zircon (open symbols) and baddeleyite (solid symbols) of the Tupertalik carbonatite is shown in the inset.

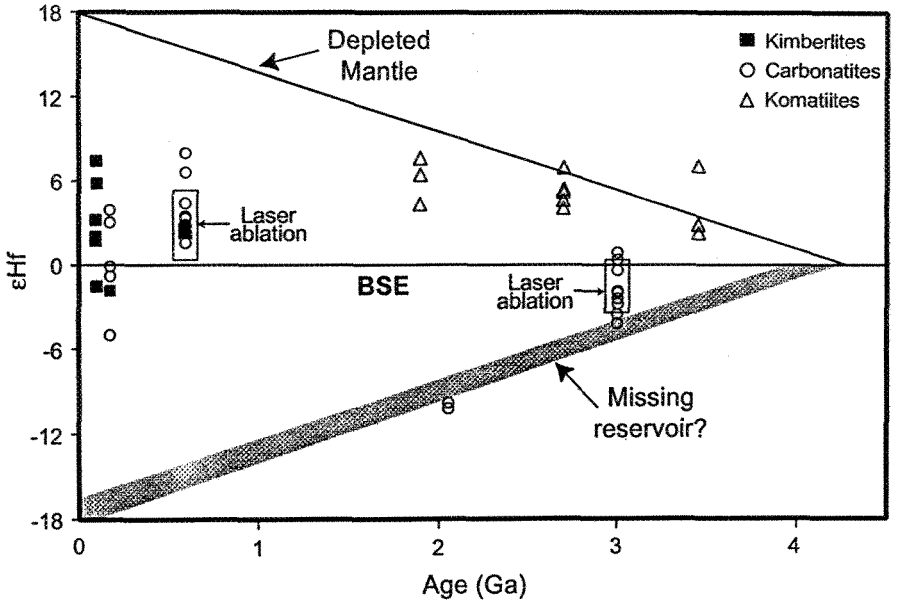

Figure 2. Hf isotope evolution diagram. Boxes outline range of Hf isotopic compositions determined by laser ablation-MC-ICP-MS. Komatiite data is from Blichert-Toft and Arndt (1999), whereas Hf isotope values at 2.059 Ga and <90 Ma are from Scherer *et al.* (2001) and Nowell et al. (1999), respectively. External reproducibility (2σ), based on repeated analysis of the JMC 475 standard in solution mode (Table 1 caption), is approximately ± 1 ε_{Hf} unit. The BSE reference line is from Blichert-Toft and Albarède (1997), while the depleted mantle evolution line is modified from Vervoort and Blichert-Toft (1999). The gray band depicts the evolution of the enriched reservoir using a $^{176}Lu/^{177}Hf$ ~0.027, and extraction age of 4 Ga.

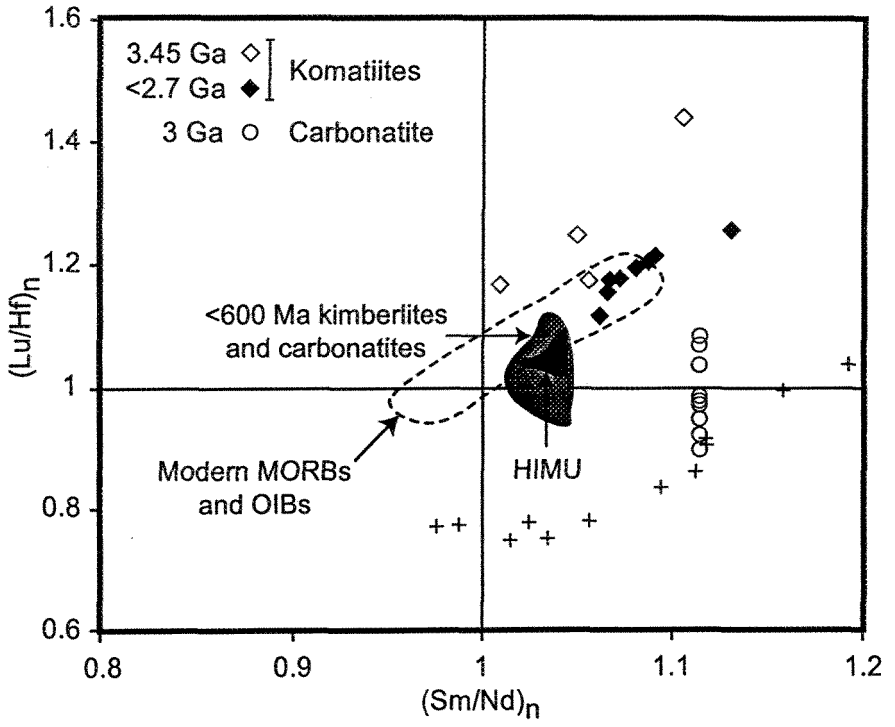

Figure 3. Time-integrated Lu/Hf vs Sm/Nd ratios estimated for the source region of komatiites, carbonatites, kimberlites and modern MORBs, normalized to chondritic values (modified from Nyquist and Shih, 1992). Planetary reference values used in calculations are the same as mentioned in Table 1. Source for komatiite and kimberlite data is same as in Figure 2, while the HIMU field is from Salters and White (1998). Nd isotope compositions for zircon and baddeleyite were assumed to be equal to the initial Nd isotope compositions of their host whole-rock carbonatite because the latter contains extremely high abundances of Nd (average ~250 ppm), which buffer the Nd isotope composition inherited from their mantle source against possible crustal contamination. ε_{Nd} compositions for the carbonatite and kimberlite samples represent minimum values since their $^{147}Sm/^{144}Nd$ values are slightly lower compared to that of their mantle source region (i.e. recycled mafic component). The lower Sm/Nd values are attributed to the

preferential addition of Nd (and LREE), which most probably reflects the presence of a volatile-rich (metasomatic agent) within the recycled reservoir, and a low degree of partial melting. The modern MORBs and OIBs array is from Albarède *et al.* (2000). Plus symbols (+) show parent/daughter values for modern MORB samples (Chauvel and Blichert-Toft, 2001); these samples indicate a decoupling to lower Lu/Hf ratios and may imply that similar lithospheric material has been recycled into the mantle and is present in the source region of kimberlite and carbonatite magmas.

GENERAL CONCLUSIONS

In the course of this thesis, we have used major element and isotope geochemistry of different geological material to study the dynamics of Earth's mantle through time. It included the use of cutting edge technology (plasma source mass spectrometry) as well as the implementation of new analytical procedures (Lu-Hf chemical separation scheme, *in situ* isotopic analyses by laser ablation). The five most significant contributions to the scientific community can be summarized as follows:

1) The lithospheric mantle underneath the Sarfartoq area of Greenland is compositionally layered. The compositional stratification is expressed by the presence of an upper refractory harzburgitic assemblage (70 to 180 km) underlain by a layer (180-225 km) of fertile lherzolites. The sharp nature of the stratification may indicate a two-step process for the formation of this lithosphere, i.e. multistage growth of the lithospheric root.

2) The coupling of a laser system to a multi-collector plasma source mass spectrometer (LA-MC-ICP-MS) provides a rapid and effective approach to determine the extent of isotopic heterogeneity within a single sample or individual grains, with analytical precision approaching that obtained by conventional thermal ionization mass spectrometry.

3) In situ measurements of Sr isotopes by LA-MC-ICP-MS in coexisting apatites and carbonates from a carbonatite complex of Southwestern Greenland reveal a large range in 87Sr/86Sr values, suggesting that these minerals precipitated predominantly under non-equilibrium conditions. The isotopic variations observed within individual hand specimens may therefore reflect larger- (regional) scale open-system processes,

possibly involving mixing of carbonatitic melts derived from distinct mantle sources, or from a common isotopically heterogeneous mantle.

4) Kimberlites and carbonatites are derived from a previously unidentified mantle reservoir of unradiogenic Hf and radiogenic Nd isotopic compositions, possibly isolated in the deep mantle for at least 3 Ga. Mass balance calculations suggest that the kimberlite/carbonatite source reservoir may amount to ~10-15% of the total mass of the BSE and, as such, close the mass imbalance in the terrestrial Hf-Nd budget.

5) The early to mid-Archean terrestrial mantle was isotopically much more heterogeneous (in particular for Lu/Hf) than the present-day mantle sampled by MORBs and OIBs. The isotopic heterogeneity observed in the early terrestrial mantle exhibits similarities to the poorly mixed mantles of planetary bodies such as Mars and the Moon and, as such, may represent a transient regime inherited from initial planetary differentiation. Our study thus confirms that such isotopic heterogeneity was still present as late as around 3 Ga, but more elusive in <2.7 Ga mantle-derived rocks.

APPENDIX

Chapters two and three of the thesis present newly developed analytical procedures. Although all analytical details relating to the second chapter were extensively described, this was not the case for the third chapter, because this manuscript was written using the 'short communication style', required for publication in *Geology*. To this effect, this appendix provides additional analytical details related to the third chapter and is essentially focused on the solution mode analyses because the analytical details related to the laser ablation experiments follow the procedures described by Machado and Simonetti (2001).

Analytical procedures-Solution mode Lu-Hf isotopic analyses

Whole-rock powders and zircon/badelleyite fractions were spiked (whole-rock powders only) with separate ^{180}Hf and ^{176}Lu isotopic tracers, and dissolved in HF-HNO3-HClO4 mixtures in steel-jacketed Teflon bombs at 160° for seven days. Hf was isolated by fluoride precipitation and then purified via a two-stage elution scheme (Blichert-Toft et al., 1997). Lu was separated from the fluoride salt following a first stage cation column (Blicher-Toft et al., 1997) followed by purification on a HDHEP column. Total procedural blanks were <50 pg and <10 pg for Hf and Lu, respectively, roughly 1000 times lower than the amount of Hf in the samples, and hence negligible.

Hf and Lu isotopes were measured at the GEOTOP Centre (Montreal, Quebec) on a Micromass Isoprobe. Samples were aspirated in the plasma source in a 2% HNO3 solution via an Aridus microconcentric nebulaliser, at a constant uptake rate of ~50 ul/min. Sweep gas settings were adjusted to maximize ion beam intensity and reduce oxide productions, and were kept constant during each analytical session. Typical oxide production rates were

consistently <0.1% of the ion signals analyzed. The Hf isotopic data was acquired in static, multi-collection mode, using eight Faraday detectors. The mass configuration array is set-up to monitor masses ^{173}Yb to ^{182}Ta (Table 2), allowing for the measurements of the Hf isotopes as well as potential isobaric interferences from Lu, Yb, and W. This was achieved by monitoring masses ^{175}Lu (for ^{176}Lu), ^{173}Yb (for ^{176}Yb), and ^{182}W (for ^{180}W), following the procedure described by Blichert-Toft et al. (1997). Isobaric interferences were corrected during data acquisition using the stable ratios recommended by Blichert-Toft et al. (1997). Other potential isobaric interferences include middle rare earth oxides such as GdO and DyO, interfering at mass 176 and mass 177. Since these may not be corrected for during the data acquisition process, samples are systematically verified prior to analysis by monitoring the ^{157}Gd and ^{161}Dy interference-free isotopes. However, intensities of ^{157}Gd and ^{161}Dy in the Hf separates were at or below detection level for all samples studied. Lu isotopes were measured using the same instrument and the same collector set-up used for Hf isotopes was used to monitor masses ^{168}Yb to ^{177}Hf. Potential isobaric interferences on Lu are Hf and Yb, both interfering at mass 176, and are corrected by monitoring the interference-free ^{173}Yb and ^{177}Hf isotopes, using the values recommended by Blichert-Toft et al. (1997). The Lu separates were also systematically verified for the presence of MREE prior to each analysis. Ion beam intensities for the Gd and Dy peaks were consistently one order of magnitude less than the ion signal for the Lu or Yb peaks. Given the typical oxide production of 0.1% observed in this study for MREE such as Gd and Dy, the bias introduced on either the ^{176}Lu/^{175}Lu or the ^{176}Yb/^{177}Yb is <20ppm, and considered negligible.

The Hf fractions were analyzed in one block of 50 scans with a 10 second integration

time for each cycle. Prior to each isotope measurement, a 50 second 'on peak' zero baseline measurement was performed to monitor the gas and acid blanks. This was followed by baseline measurements at half-mass units (20 seconds). Repeated analyses (n=20) of the JMC Hf standard yielded $^{176}Hf/^{177}Hf$=0.28216+3, $^{178}Hf/^{177}Hf$=1.46726+15 and $^{180}Hf/^{177}Hf$=1.88667+26 (2s, standard deviation). The Lu isotopes were analyzed in blocks of 50 scans with a five second integration time for each cycle. The measured Hf isotopes were normalized for the mass bias to $^{179}Hf/^{177}Hf$=0.7325, while the measured Yb and Lu isotopic ratios were corrected after determination of the Lu and Yb mass biases from a pure Ames solution prior to analysis. Mass bias corrections were made using the exponential mass fractionation law (Russel, 1978). Spike-sample un-mixing was achieved by iteratively solving a non-linear equation combining the exponential fractionation law and a spike-natural isotope mixing equation (Blichert-Toft *et al.* 1997).